

BOSTON UNIVERSITY
COLLEGE OF ENGINEERING

Dissertation

**SHORTWAVE INFRARED SPATIAL FREQUENCY DOMAIN
IMAGING TO QUANTIFY BLOOD LIPIDS**

by

ANAHITA PILVAR

B.S., Sharif University of Technology, 2017
M.S., Boston University, 2021

Submitted in partial fulfillment of the
requirements for the degree of
Doctor of Philosophy

2023

© 2023 by
ANAHITA PILVAR
All rights reserved, except for Chapter 3 (All except 3.2.1), which is © 2022 by SPIE and Chapter 4, which is © 2023 by SPIE

Approved by

First Reader

Darren Roblyer, Ph.D.
Associate Professor of Biomedical Engineering
Associate Professor of Electrical and Computer Engineering

Second Reader

Irving J. Bigio, Ph.D.
Professor of Biomedical Engineering
Professor of Electrical and Computer Engineering
Professor of Physics
Professor of Medicine

Third Reader

Ji-Xin Cheng, Ph.D.
Moustakas Chair Professor in Photonics and Optoelectronics
Professor of Biomedical Engineering
Professor of Electrical and Computer Engineering
Professor of Materials Science and Engineering
Professor of Chemistry
Professor of Physics

Fourth Reader

Mark Pierce, Ph.D.
Associate Professor of Biomedical Engineering
Rutgers, The State University of New Jersey

Fifth Reader

Jorge Plutzky, MD
Associate Professor of Medicine
Harvard Medical School

DEDICATION

To Maman and Baba

ACKNOWLEDGMENTS

Firstly, I would like to thank Darren for his exceptional mentorship throughout the past six years. I have been very fortunate to have the opportunity to learn from Darren, not only about science, but he has also provided me with essential skills in areas like problem-solving and effectively communicating my research. I am truly grateful for his support and guidance, which have played an important role in shaping my academic journey.

I would like to thank Irving Bigio for his invaluable comments and feedback throughout these years. I have been privileged to be Irving's student, and I have greatly benefited from our weekly group meetings, where I had the opportunity to tap into his exceptional wisdom and expertise.

I am grateful to Mark Pierce who has consistently been a source of support throughout our collaboration, providing invaluable and detailed feedback on our joint work.

I would like to thank Ji-Xin Cheng and Jorge Plutzky, for their helpful insight and encouragement. I am very grateful to have them as members in my committee.

I would like to thank members of BOTLab who were wonderful and fun to work with and made my PhD journey enjoyable!

Great thanks to my friends in Boston who have become like a second family to me during my time here and my friends from back home (in Iran and all over the world) who have brightened my days with their unwavering friendship.

And finally, my biggest thank to my family who has been my ultimate source of love and support in my entire life. I owe my accomplishments to their constant encouragement and belief in me. To my family, I couldn't have done this without you and I love you so much.

SHORTWAVE INFRARED SPATIAL FREQUENCY DOMAIN

IMAGING TO QUANTIFY BLOOD LIPIDS

ANAHITA PILVAR

Boston University, College of Engineering, 2023

Major Professor: Darren Roblyer, Ph.D., Associate Professor of Biomedical Engineering, Associate Professor of Electrical and Computer Engineering

ABSTRACT

Blood lipids are one of the main biomarkers for cardiovascular diseases (CVD). Current method for blood lipid assessment requires invasive blood draws, usually after an overnight fast, followed by lab-based testing, makes the technique not suitable for regular monitoring. The limitations of invasive blood testing techniques, alongside the growing evidence supporting the benefits of regular lipid monitoring, particularly after a meal, for better CVD prediction, indicate that there is an unmet need for non-invasive blood lipid assessment.

Our lab recently demonstrated the possibility of non-invasive blood lipids monitoring using a diffuse optical technique called shortwave infrared spatial frequency domain imaging (SWIR SFDI). Using SWIR SFDI, we have shown that an increase of blood lipids after a high fat meal that was measured with gold standard blood draw, correlates strongly with an SFDI derived parameter called SWIR-MPI index. While the results were promising, advancements in SFDI instrumentation, modeling, and experiments are needed prior to clinical testing and translation.

The work presented in this dissertation was focused on identifying the source of optical contrast induced by blood lipids, and advancing SFDI instrumentation and processing methodology for the goal of developing a clinic-ready optical system for non-invasive blood

lipid assessment. To improve SFDI instrumentation, the SFDI parameters were fine-tuned, and a new compact and portable system was developed and assessed for its performance using optical phantoms. A new two-layer model that accounts for the effect of skin was developed to improve SFDI processing methodology when measuring human subjects. The integration of the new instrument and model make SFDI technique more suitable to use for human studies. Next, the effect of lipids on optical properties of blood were investigated through literature reviews, theoretical simulations and ex-vivo experiments on bovine blood. Finally, we conducted a healthy volunteer study to monitor blood lipid alteration after low fat and high fat meal with SFDI.

Together, the works in this project advances our comprehension of the optical effects of blood lipids and their association with meal consumption in both healthy individuals and those with dyslipidemia. The innovative technology and the preliminary feasibility study push the boundaries of non-invasive blood lipid assessment, offering promising prospects for translating this technology to clinical settings, thereby enhancing CVD risk assessment.

CONTENTS

Dedication	iv
Acknowledgements	v
Abstract	vi
List of Tables	xi
List of Figures	xii
List of Symbols and Abbreviations	xix
1 Introduction	1
1.1 Motivation	1
1.2 Aims	3
1.3 Chapter summaries	3
2 Background and Significance	5
2.1 Cardiovascular diseases	5
2.2 Blood lipid: a risk factor for cardiovascular disease	5
2.2.1 Non-fasting triglyceride concentration as CVD risk factor	6
2.2.2 Limitations of current blood lipid techniques	7
2.3 Spatial frequency domain imaging (SFDI)	7
2.3.1 SFDI in shortwave infrared (SWIR)	10
2.4 Limitations of previous SWIR SFDI measurements for blood lipid monitoring	12

3	LED-based NIR-SWIR SFDI for non-invasive measurement of tissue and blood optical properties	14
3.1	Introduction	15
3.2	SWIR SFDI imaging background	17
3.2.1	Comparing SWIR SFDI to NIR SFDI and DOSI	18
3.3	SWIR SFDI design criteria	25
3.3.1	Wavelength and spatial frequency selection	25
3.4	The SWIR SFDI system	30
3.5	Calibration and In-frame phantom correction	32
3.6	System characterization	33
3.7	Two-layer model	35
3.8	In-vivo blood and tissue measurements	38
3.9	Discussion	41
3.10	Conclusion	43
4	Feasibility of postprandial optical scattering of lipoproteins in blood as an optical marker of cardiovascular disease risk: modeling and experimental validation	44
4.1	Introduction	45
4.2	The basic properties of plasma lipoproteins and their synthesis	47
4.3	Experimental measurements of lipoproteins-like particles in blood	49
4.4	Estimation of blood μ_s' alterations with Mie theory	52
4.5	Chylomicron and VLDL scattering parameters from literature	57
4.6	Estimation of blood μ_s' changes after a meal	61
4.7	Discussion	64
4.8	Conclusion	67

5	Non-invasive assessment of blood lipid using spatial frequency domain imaging (SFDI): healthy volunteer study	68
5.1	Introduction	69
5.2	Materials and Methods	70
5.2.1	Subjects eligibility and enrollment	70
5.2.2	Spatial frequency domain imaging (SFDI) system	71
5.2.3	Postprandial experiment procedure	72
5.2.4	Measurement procedure	73
5.2.5	Data analysis	75
5.3	Results	77
5.3.1	Lipid panel	77
5.3.2	SFDI results	78
5.3.3	Arterial occlusion results	82
5.4	Discussion	85
5.5	Conclusion	88
6	Conclusions and future directions	89
6.1	Summaries	89
6.2	Future directions	91
6.3	Conclusion	93
	Bibliography	94
	Curriculum Vitae	105

LIST OF TABLES

3.1	Comparisons between SFDI, DOSI, and SWIR-MPI.	19
3.2	Comparison of water and lipid extraction errors for different wavelength pairs and noise models.	25
4.1	Reported literature properties for TRLs and triglyceride in the fasting state as well as model parameters	59
4.2	Reported literature properties for TRLs and triglyceride in the postprandial state	60
4.3	$\Delta\mu_s'$ from the baseline for different level of TG correspond to different subject population. The Mie simulated μ_s' was added to measured bovine blood μ_s' at each wavelength	64
5.1	Pearson Correlation between measured triglyceride and SFDI parameters after normalizing to the baseline. Correlations with p-value < 0.05 are shown.	82

LIST OF FIGURES

2.1	A) Schematic diagram of a SFDI system. The illumination source is a set of VIS-NIR LEDs. The illumination source combined with a DMD is labeled as projector in this diagram. Two crossed polarized linear polarizers are placed in the illumination and detection path to avoid specular reflection. B) SFDI data acquisition and processing flowchart. Top row represents the captured raw images at DC and AC at 851 nm. The raw AC images are the three phases captured at a spatial frequency of 0.1 mm^{-1} . Raw images are demodulated, corrected for height and angle variability, and calibrated. The middle row represents the calibrated diffuse reflectance (R_d) maps at DC and AC. The R_d maps are converted into optical property maps (μ_a and μ_s') using a LUT inverse model [1].	9
2.2	SWIR SFDI system diagram	12
3.1	The absorption and reduced scattering of a representative human tissue from 500 nm to 1300 nm. Left y-axis: The absorption coefficients of oxy-hemoglobin ($7.74 \mu\text{M}$), deoxyhemoglobin ($0.12 \mu\text{M}$), water (21.42%) and lipid (27.74%) represent previously published measurements taken from human subjects on the dorsal forearm with skin type I-II [2]. Left y-axis shown in log-scale. μ_a was calculated by multiplying the extinction coefficient by the concentration for each chromophore. Right y-axis: reduced scattering coefficient of human skin in linear scale.	18

3.2	A) White light image of ex vivo porcine tissue measured by DOSI and SWIR-MPI. B) Water, lipid, and optical property maps (930 nm) measured by DOSI with a 10 mm sampling grid and 28 mm source-detector separation. C) Water, lipid, and optical property maps (930 nm) measured by DOSI with a 5 cm × 10mm sampling grid and 10 mm source-detector separation. D) Water, lipid, and optical property maps (1210 nm) measured by SWIR-MPI.	21
3.3	Condition number plot for extinction coefficient matrices containing values for water and lipid at wavelengths between 700 to 1300 nm.	23
3.4	Average absolute errors in water and lipid extraction based on simulations with a) a model based on experimental SWIR-MPI system noise, b) a model assuming 5% zero-mean Gaussian noise.	24
3.5	SWIR-MPI (meso-patterned imaging) noise model at seven wavelengths and eight spatial frequencies	26
3.6	Cramer-Rao results for A) μ_a and B) μ_s' at spatial frequency of DC and 0.15 mm^{-1}	28
3.7	Photon 90th percentile depth penetration for skin optical properties at three spatial frequencies (DC, 0.1 mm^{-1} and 0.15 mm^{-1}) [3]. The shaded area shows the reported range for human skin thickness [4, 5, 6].	29

3.8	<p>A) Schematic diagram of the SWIR SFDI system. Light from the two LEDs is collimated and combined at a dichroic mirror. The DMD generates the spatially modulated light that projects onto the sample with an achromatic lens. Two linear polarizers are placed in the illumination and detection path to reject specular reflection. B) The fabricated SWIR SFDI system. C) Representative images from the system captured at 880 nm. Top row represents the raw images with DC and AC illumination patterns superimposed on the white light image of the hand taken with a camera phone. The middle row represents the calibrated diffuse reflectance at two spatial frequencies. Bottom row shows the optical property maps (μ_a and μ_s').</p>	31
3.9	<p>Results of an intralipid titration experiment to characterize the measurement sensitivity of SWIR SFDI to lipid concentration increments of 0.05% at 880 nm and 1100 nm. A) The measured absorption coefficient stayed largely unchanged when lipid concentrations were increased from 1.55% to 2.45%. B) The measured reduced scattering coefficient increased with increasing intralipid concentrations. C) Histograms of μ_s' pixel values from three consecutive measurements in the lipid titration experiment. The differences between the distribution of measurements of 1.95%, 2.0% and 2.05% lipid concentration were statistically significant (**** indicates $p < 0.0001$, determined with Student's t-test). D) μ_s' maps of four intralipid suspensions from 2.0% to 2.3% concentrations. All four concentrations were placed in the same field of view and measured simultaneously.</p>	35

3.10	A) A schematic of the two-layer MC simulation geometry. The inset shows a 1 mm thick skin-simulating phantom made with intralipid and agar. B) Comparison of bottom layer μ_s' measured using one-layer and two-layer LUTs. The absolute extraction errors for μ_s' are shown.	37
3.11	Healthy volunteer results (subject #1) from the dorsum of the hand. A) Optical property maps at 880 nm and 1100 nm using one-layer LUT and B) two-layer LUTs. C) Line profiles over the dotted red line for μ_a and d) μ_s' . Blue shows the line profiles at 880 nm and red shows the line profiles at 1100 nm. The solid lines correspond to the one-layer LUT results and dashed lines correspond to the two-layer LUT results. The use of the two-layer LUT enhances the contrast of the superficial blood vessel especially in μ_s' . The red arrow in D) shows an example of a vessel-like structure that is identified in μ_s' map but not in μ_a map at the same wavelength.	40
4.1	Blood triglyceride pathways: Chylomicron and VLDL are the main source of blood triglycerides (TG). Chylomicrons enter the blood through the small intestine after dietary fat intake and hence they are the exogenous source of blood TG. VLDLs enter the blood through the liver and they are the endogenous source of blood TG.	48
4.2	System diagram of the three-LED SFDI system.	50
4.3	Intralipid in bovine blood titration experiment results A) Measured absorption coefficient at three wavelengths showing no appreciable change as intralipid concentration increases from 0.1% to 1%. B) Reduced scattering coefficient increases with intralipid concentration for all measured wavelengths. C) $\Delta\mu_s'$ shows larger increase for shorter NIR wavelengths	51

4.4	<p>Microsphere bead in blood titration experiment at 730, 880 and 1100 nm. The results show the effect of added particle size on blood μ_s' as the bead concentration and size increases. The largest μ_s' increases occur from 100 nm to 500 nm. Bead concentration is indicated as volume percentage of bead in blood.</p>	52
4.5	<p>A) μ_s' results from titration experiments are shown in solid lines and Mie simulation results from the same lipid concentrations added to the baseline pure blood μ_s' are shown in dashed lines at 730, 880 and 1100 nm. The experiment results do not match the simulations due to the dependent scattering events caused by RBCs. B) Mie predicted μ_s' match the experiment results after correction by Twersky factor to account for dependent scattering events.</p>	55
4.6	<p>A) Mie simulation results shows the effect of particle size on μ_s' at three simulated wavelengths. The markers shows the particle sizes that were used in the bead experiment B) Comparison between the measured μ_s' and the simulated μ_s' at different bead size, concentration and wavelengths. Different colors correspond to different wavelengths and different marker shape correspond to different bead sizes. Each data point corresponds to a different concentration from 0.1% to 0.6% (V/V) of bead in bovine blood. The black dashed line is the identity line.</p>	56
4.7	<p>VLDL and chylomicron size distribution for 100 mg/dL of blood triglyceride</p>	59

4.8	Mie simulation results for whole blood in fasting and postprandial state. A) Simulation parameters B) Blood scattering coefficient (μ_s) B) anisotropy factor and C) blood $\mu_s l$ as the triglyceride content in blood increases. The increase in triglyceride results in higher concentration of chylomicrons, larger chylomicron particles and higher refractive index. D) Percent change in blood $\mu_s l$ from the baseline (first simulation results)	63
5.1	a. Schematic diagram of three-LED SFDI system b. SFDI data acquisition and processing flowchart. Top row shows the raw images captured at spatial frequency of DC and 0.1 mm^{-1} from dorsal surface of a subject's hand at 880 nm. The captured images are demodulated and calibrated and the diffuse reflectance data is converted into absorption and reduced scattering coefficient using the two-layer look up tables (LUTs) introduced in Chapter 3 . The bottom row shows the μ_a and $\mu_s l$ maps. The images were cropped to only show the hand ROI.	72
5.2	a. Study timeline b. Measurement procedure	74
5.3	Percent change in a) triglyceride concentration b) glucose concentration and c) cholesterol concentration compared to the fasting state (time point = 0) during the 5 hours postprandial measurements after high fat and low fat meal. Asterisks show the level of significant different between the two subject groups. $p < 0.00001$ is shown with **** and $p < 0.05$ is shown with *	78
5.4	Oxyhemoglobin maps at baseline and three hours after the meal for representative subjects in high fat and low fat category.	79

5.5	a. The process of generating the vessel mask using μ_a map at 880 nm and apply the mask to segment vascular and microvascular regions. b. Temporal changes and trends in three SFDI-derived parameters with the strongest correlation with serum triglyceride over the six measurements for high fat and low fat groups. $p < 0.05$ is shown with * and p -value < 0.01 is shown with **. c) The correlation plots for the same three metrics with triglyceride concentration combining all subjects from both group. All metrics were normalized to their respective baseline values.	81
5.6	a. an example of μ_a changes during the cuff occlusion experiment and the identified parameters after the release. b. Microvascular μ_a is shown during the 8-minute cuff occlusion experiment at baseline and three hours after the meal for two representative subjects. The top panel displays the results from a subject who consumed a high fat meal, and the bottom panel shows the results from a subject who consumed a low fat meal. c. Calculated parameters during the reactive hyperemic phase for low fat and high fat meal subjects. The solid lines represent the mean values, while the shaded regions depict the standard error between all subjects.	84

LIST OF SYMBOLS AND ABBREVIATIONS

ANOVA	Analysis of variance
AUC .	Area under the curve
CM ..	Chylomicron
CRB .	Cramer Rao Bound
CVD .	Cardiovascular disease
DMD .	Digital micromirror device
DOS .	Diffuse optical spectroscopy
$f_x \dots$	Spatial frequency
FOV .	Field of view
HDL .	High density lipoprotein
ICC .	Intraclass correlation coefficient
IDL .	Intermediate density lipoprotein
LDL .	Low density lipoprotein
LUT .	Look-up table
MAE .	Mean absolute error
MC ..	Monte Carlo
MPI .	Meso-patterened imaging
MTF .	Modulation transfer function
NIR .	Near Infrared
$R_d \dots$	Diffuse reflectance
RBC .	Red blood cells
RI ..	Refractive index

ROI .	Region of interest
SCOS .	Speckle contrast optical spectroscopy
SFDI .	Spatial frequency domain imagin
SWIR .	Shortwave Infrared
TG ..	Triglyceride
TRL .	Triglyceride rich lipoprotein
VIS ..	Visible
VLDL	Very low density lipoprotein
WHO .	World Health Organization

CHAPTER 1

Introduction

1.1 MOTIVATION

Cardiovascular diseases (CVD), including coronary heart disease, heart failure and stroke are the leading cause of death in the world, accounting for more than 30% of global death [7]. Hyperlipidemia, or abnormal elevation of blood lipids including cholesterol and triglycerides, is an important biomarker for CVD and is strongly tied to future risk of myocardial infarction and stroke [8]. Currently, blood lipids measurement requires invasive blood draws, trained technicians, and lab infrastructure, limiting access to regular screening for those at risk of CVD and leading to undertesting and undertreatment [9]. More regular blood lipid monitoring is an unmet need that may improve CVD diagnosis and treatment. Fast noninvasive blood lipid measurements would allow at-risk patients and patients with dyslipidemias (e.g. type II diabetes) to be screened and monitored more regularly to ensure blood lipids levels are under control.

Spatial Frequency Domain Imaging (SFDI) is a non-invasive diffuse optical imaging technique that can quantify the optical properties (i.e. absorption and reduced scattering) of biological tissues in a non-contact and wide-field manner [10]. SFDI uses structured illumination at several wavelengths and spatial frequencies to determine the optical modulation transfer function (MTF) of tissue, which can be converted to optical properties through an inverse model of light transport in a diffusive media. SFDI has been widely used in visible (VIS: 400-700 nm) and near-infrared (NIR: 700-900 nm) wavelength region where oxy- and deoxyhemoglobin are the dominant absorbers [11].

Previously our group has extended the SFDI technique to the shortwave infrared (SWIR) wavelength band (900-1300 nm) [12]. SWIR exhibits strong and distinct absorp-

tion characteristics of water and lipid while hemoglobin absorption is minimal [13]. Additionally, the increased penetration depth of specific SWIR wavelengths in tissue makes the SWIR advantageous over NIR for deep tissue imaging [12]. The utilization of SWIR SFDI have enabled our lab to non-invasively monitor changes in water content in mouse edema model and generate an ex-vivo map of tumor lipid content [12]. Moreover, a previous Ph.D. student in our lab conducted a study on healthy volunteers with SWIR SFDI to monitor blood lipid changes after a meal [12].

While promising, there are several key challenges and limitations related to the blood lipid study that need to be addressed. For example, the previous SWIR SFDI system utilizes a tunable femtosecond laser with table-top optics that is not suitable for clinical use due to large system size and slow wavelength tuning speed (27 sec per wavelength). Identification of measurement parameters such as wavelength and spatial frequency and development of models that account for skin tone to improve blood lipid quantification are other aspects of the work that needs to be addressed. Additionally, the source of optical changes induced by blood lipids has not been previously explored.

The primary objectives of this thesis project are to investigate and characterize the effect of blood lipid on the optical properties of peripheral tissue and blood, as well as to examine the hemodynamic responses related to lipid following meal consumption. To achieve these objectives, several key challenges associated with non-invasive blood lipid measurements using SFDI were addressed. This involved the development of a portable SFDI system tailored for clinical use, incorporating optimal wavelengths and spatial frequencies along with a more advanced inverse modeling. Furthermore, for the first time the optical characteristics of blood lipid were thoroughly investigated and characterized, specifically their impact on in-vivo optical property measurements after a meal. Lastly, a comprehensive postprandial blood lipid study was conducted on a group of healthy volun-

teers, providing novel insights into the effect of lipid on NIR measurements. The findings of this study contribute to our understanding of the dynamic changes in optical properties induced by lipid.

By addressing these objectives, this thesis project contributes to the advancement of non-invasive measurement techniques for blood lipid assessment and provides valuable insights into the relationship between lipid metabolism, optical properties, and hemodynamic responses. These findings have potential implications for managing dietary interventions and improving the early detection and management of cardiovascular diseases.

1.2 AIMS

In this project, our objective is to address the challenges associated with blood lipid monitoring using SFDI by developing SFDI instrumentation and processing methodology, as well as conducting an initial feasibility study for in-vivo blood lipid assessment. To achieve this, we have set the following aims:

Aim 1: Develop a clinic-ready portable SFDI system and a 2-layer inverse model for accurate quantification of blood lipid

Aim 2: Characterize the optical signature of lipoproteins and their effect on optical properties of blood

Aim 3: Conduct a healthy volunteer study for longitudinal blood lipid monitoring

1.3 CHAPTER SUMMARIES

All the work presented in this dissertation focuses on non-invasive blood lipid measurement using near-infrared (NIR) and shortwave infrared (SWIR) light with spatial fre-

quency domain (SFDI) imaging instrumentation. **Chapter 1** provides the motivation behind this work by identifying blood lipids as an important risk factor for cardiovascular diseases. **Chapter 2** provides background on current state of blood lipid monitoring, and spatial frequency domain imaging (SFDI) as a potential alternative for blood lipid measurements. **Chapter 3** investigates the SFDI parameters and light propagation model for optimizing SFDI for blood lipid application. Additionally this chapter introduces the newly fabricated LED-based NIR-SWIR SFDI system as an alternative to laser based SWIR SFDI system for blood lipid study. **Chapter 4** explores the effect of blood lipid on optical scattering of blood using theoretical simulations and ex-vivo experiments on bovine blood. **Chapter 5** presents the results from a postprandial healthy volunteer study and compares the effect of low fat and high fat meal on optical properties measured with SFDI for 5 hours after the meal. Finally **Chapter 6** discusses the final conclusions and future directions.

CHAPTER 2

Background and Significance

2.1 CARDIOVASCULAR DISEASES

Cardiovascular diseases (CVD), including coronary heart disease, heart failure, stroke and other forms of CVD are the number one cause of death in the world. CVD is estimated to cause more than 30% of global death. The World Health Organization (WHO) estimates 17.9 million deaths from CVD every year [7]. The economic costs of CVD is estimated to be more that \$400 billion each year in the US [14]. More than 75% of the CVD death occur in low- and middle income countries due to late diagnosis and non-effective health care services, yet CVD is the major contributor to US mortality as well [7, 15].

The risk of CVD increases with age, with majority of deaths related to CVD happen in people aged 65 and above. However, CVD such as atherosclerosis are known to be slow and progressive disease starting as early as childhood. There are various behavioral risk factors linked to CVD including tobacco use, an unhealthy diet and physical inactivity. These factors can lead to raised blood pressure, raised blood glucose and lipid levels, as well as diabetes and obesity.

2.2 BLOOD LIPID: A RISK FACTOR FOR CARDIOVASCULAR DISEASE

Hyperlipidemia, defined as abnormal elevation of blood lipids, is one of the major predictor of CVD and can be an indication of increased risk of heart attack, myocardial infraction and stroke [8, 16, 17]. Measurements of different lipid species, including cholesterol, triglycerides, low-density lipoproteins (LDL), and high-density lipoproteins (HDL), each have strong predictive power as biomarkers for CVD. For example, previous studies

have shown that elevated triglyceride rich lipoproteins (>580 mg/dL) can be an independent predictor of CVD and would result in 5.1-fold increase in myocardial infarction, and 2.2-fold increase in all CVD mortalities compared to the low triglyceride level [18].

Regular blood lipid screening is essential for CVD early diagnosis, surveillance, and treatment feedback. Some studies recommend blood lipid screening every 5 years for adults to improve CVD risk assessment [19, 20]. Considering that 31% of American adults suffer from hypertriglyceridemia with triglyceride level above 150 mg/dL, regular blood lipid monitoring is crucial for those at risk of CVD [19].

2.2.1 Non-fasting triglyceride concentration as CVD risk factor

The current standard procedure for assessing blood lipid levels involves fasting for 8-12 hours prior to the measurements [21]. However, blood triglyceride level changes substantially in the postprandial state. Since most individuals spend the majority of waking hours in a postprandial state, fasting triglyceride level do not accurately represent the dynamic nature of lipid metabolism. Furthermore, while fasting triglyceride levels are a risk factor for CVD when adjusted for HDL-Cholesterol [21], postprandial plasma triglyceride levels independently predict CVD risk [17]. Recent evidence suggest that postprandial measurement of blood lipids may further improve CVD risk prediction and help to identify pre-diabetic conditions [22, 23]. Hypertriglyceridemia is more severe in patients suffering from obesity, insulin resistance and diabetes, conditions which are also directly associated with CVD risk factors [19, 24]. For these reasons postprandial blood lipid measurements has recently gained more interest as it may provide more information about the cardiovascular health.

2.2.2 Limitations of current blood lipid techniques

Currently, measuring blood lipids requires invasive blood draws, typically after an overnight fast. In addition to being invasive, the method and the subsequent lab-based analysis require trained technicians and lab equipment, which limits access to blood lipid testing and prevents those at risk of CVD from regular blood lipid monitoring. Poor access to regular blood lipid testing results in CVD undertreatment and ongoing health problem for decades. Longitudinal monitoring of blood lipid under non-fasting condition after a high fat meal has shown further improvement in CVD prediction and diagnosis accuracy. However, such longitudinal blood testing requires multiple blood draws over several hours, making it impractical and time and resource-intensive for clinical settings. Additionally, the latency between the blood test and availability of the results adds to the limitation of blood lipid screening for many at-risk patients. Developing a fast and noninvasive method for measuring blood lipids that provides immediate feedback would enable CVD patients to frequently monitor their lipid levels and improve CVD diagnosis and treatment.

2.3 SPATIAL FREQUENCY DOMAIN IMAGING (SFDI)

Details regarding SFDI measurements and data processing has been described elsewhere [10, 25]. Briefly, SFDI is a label free non-contact diffuse optical imaging modality that provides information on optical properties (absorption and scattering) of a biological sample from a large field of view on a pixel by pixel basis. In SFDI, spatially modulated light projected at multiple spatial frequencies (f_x) and wavelengths (λ) is used to illuminate the sample. Typically, sinusoidal spatial patterns are projected on the sample with three phase offsets ($0^\circ, 120^\circ, 240^\circ$). The reflected light from the tissue, which contains the tissue response to the projected pattern, is captured by a camera. The captured images at each phase offset (I_1, I_2, I_3) is used to calculate the amplitude envelope of the measurement for

each pixel (I) using the following demodulation algorithm (equation 2.1):

$$I = \frac{\sqrt{2}}{3} \sqrt{(I_1 - I_2)^2 + (I_2 - I_3)^2 + (I_1 - I_3)^2}. \quad (2.1)$$

The amplitude envelope is calibrated using a calibration phantom with known and stable optical properties to account for any instrument response using equation 2.2:

$$R_d = \frac{M_{AC}(f_x)}{M_{AC,ref}(f_x)} R_{d,ref}(f_x) \quad (2.2)$$

In this equation, $M_{AC}(f_x)$ refers to the amplitude envelop of the sample measurement, $M_{AC,ref}(f_x)$ refers to the reference measurement taken from the calibration phantom at the same wavelength and spatial frequency, and $R_{d,ref}(f_x)$ is the predicted diffuse reflectance (R_d) of the calibration phantom using Monte Carlo (MC) or analytical forward model of light propagation in diffusive media based on the known optical properties of the calibration phantom.

This process generates images of the diffuse reflectance of the sample at each wavelength and spatial frequency. The diffuse reflectance values typically at two spatial frequencies are used as the inputs to an inverse model of light transport in diffusive media, which decouples the relative contribution of absorption and reduced scattering at each wavelength. In other words, the calibrated diffuse reflectance measurements at two illuminating spatial frequencies are converted to the corresponding absorption coefficient (μ_a) and reduced scattering coefficient (μ_s') values at each wavelength for every pixel in the field of view. **Figure 2.1** shows a simple diagram (**Figure 2.1.A**) and flowchart of SFDI data acquisition and processing workflow (**Figure 2.1.B**).

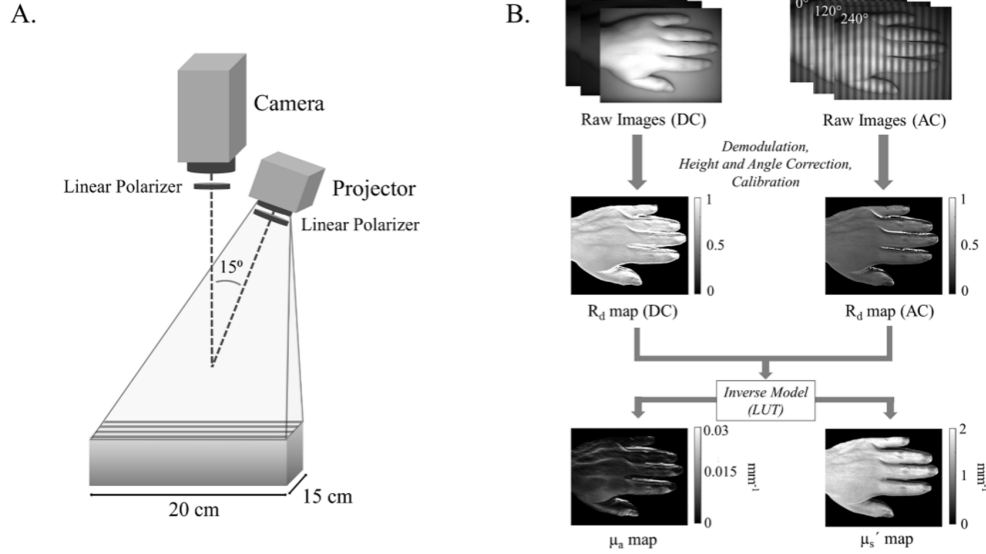


Figure 2.1: A) Schematic diagram of a SFDI system. The illumination source is a set of VIS-NIR LEDs. The illumination source combined with a DMD is labeled as projector in this diagram. Two crossed polarized linear polarizers are placed in the illumination and detection path to avoid specular reflection. B) SFDI data acquisition and processing flowchart. Top row represents the captured raw images at DC and AC at 851 nm. The raw AC images are the three phases captured at a spatial frequency of 0.1 mm^{-1} . Raw images are demodulated, corrected for height and angle variability, and calibrated. The middle row represents the calibrated diffuse reflectance (R_d) maps at DC and AC. The R_d maps are converted into optical property maps (μ_a and μ_s') using a LUT inverse model [1].

The tissue optical absorption at different wavelengths provides an absorption spectra that enables the extraction of molar concentration of the dominant light absorbing chromophores using their extinction coefficient (ϵ) by performing a least square fit with Beer's law:

$$\mu_a = \sum_i \epsilon_i C_i \quad (2.3)$$

The μ_s' can be fit to a power law using a least square fitting approach:

$$\mu_s' = a \frac{\lambda^{-b}}{\lambda_0} \quad (2.4)$$

In this equation, a is the scattering amplitude, b is the scattering slope, and λ_0 is the reference wavelength.

2.3.1 SFDI in shortwave infrared (SWIR)

To date, almost all published works on SFDI utilize visible (VIS: 400-700nm) and near-infrared (NIR: 700-900nm) wavelength bands [11, 26]. Oxy and deoxyhemoglobin are the dominant absorbers at VIS and NIR and most SFDI systems use VIS-NIR wavelength regions to extract the concentration of these two chromophores. Water and lipids have strong and distinct absorption characteristics in the SWIR wavelength band (SWIR: 900-1300nm) where absorption of hemoglobin is minimal. The spectral features of endogenous chromophores in SWIR along with the increased penetration depth at some SWIR wavelengths in tissue (4 mm) make this wavelength region advantageous over VIS and NIR for water and lipid measurements. Previous studies with diffuse optical spectroscopy (DOS) have shown the benefit of including SWIR wavelengths for more accurate estimation of water and lipid related parameters (both absorption and scattering properties) with four times higher confidence as opposed to measurements at only below 1000 nm [13]. Wilson et al. used NIR SFDI combined with unstructured illumination in the SWIR region, where they benefited from increased penetration depth and sensitivity to water and lipid absorption, to quantify the changes in the optical properties of rat skin pre- and post-burn [27].

The previous PhD student in our group for the first time has extended SFDI to the

SWIR and fabricated a table-top custom SWIR SFDI system [12]. The instrumentation of the SWIR SFDI system is shown in **Figure 2.2**. The system uses an ultrafast pulsed laser (InSight DS+, Spectra-Physics, Santa Clara, CA, USA) with tunable wavelengths range from 680 nm to 1300 nm as the illumination source. With this light source we can cover both NIR and SWIR. The laser provides high power at the entire wavelength region which helps to guarantee high SNR for the captured SFDI data. To prevent generating speckle patterns, the laser light passes through a diffuser to make the coherent light of the laser diffusive. A digital micro-mirror device (DMD) generates the spatial patterns of light with different spatial frequencies. These patterns are sequentially projected on the sample using an imaging lens and two mirrors. The remitted light is then captured with Germanium doped CMOS camera (TriWave, Infrared Laboratories, Inc., Peabody, MA, USA) with a wide spectral sensitivity (300-1600nm). A pair of crossed linear polarizers are placed in the illumination and the detection path to minimize the effect of specular reflection. With this system, a large field of view of 7 * 11 cm was achieved. Using this system, a prior Ph.D. student investigated water concentrations in a mouse edema model as well as blood lipid changes in normal volunteers [12].

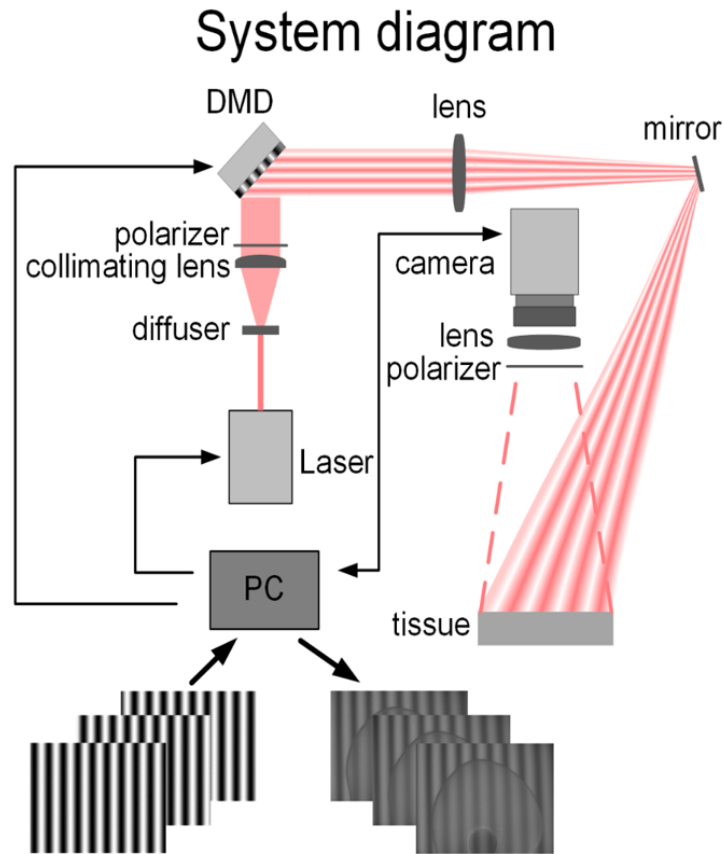


Figure 2.2: SWIR SFDI system diagram

2.4 LIMITATIONS OF PREVIOUS SWIR SFDI MEASUREMENTS FOR BLOOD LIPID MONITORING

The ability of SFDI system to estimate optical properties in a fast, label-free and non-contact manner provide a powerful tool for non-invasive blood lipid assessment. If the technique can be made simpler and lower cost, SFDI would have additional advantages for clinical lipid measurement over competing techniques such as Diffuse Optical Spectroscopic Imaging (DOSI) and photoacoustic techniques. Despite the early promising results

in measuring lipid induced changes using SWIR SFDI system, there were multiple limitations and drawbacks to the previous technology, methodology and experiments that need to be addressed.

Regarding the technology, the slow acquisition speed and immobility of the laser source were the main obstacles in using the table-top SWIR SFDI system in human measurements. The lack of exploration in identification of measurement parameters such as wavelength and spatial frequency choice is another drawback that needed to be addressed. Additionally, the development of models that account for the effect of human skin in NIR and SWIR wavelengths bands remained unexplored. Furthermore, the optical characteristics of blood lipids and their direct and indirect impact on the optical properties of tissue and blood were overlooked in previous studies. Moreover, the previous healthy volunteer study conducted with SWIR SFDI exhibited logistical issues in terms of study design and study cohort, making it challenging to draw meaningful conclusions. In this project, I specifically addressed these challenges associated with the previous SWIR SFDI technology. Furthermore, I thoroughly characterized the optical signature of blood lipids and investigated the lipid-induced changes in tissue and blood optical properties. Lastly, a comprehensive post-prandial healthy volunteer study was conducted, providing valuable insights into the effects of lipid consumption on optical measurements.

CHAPTER 3

LED-based NIR-SWIR SFDI for non-invasive measurement of tissue and blood optical properties

We previously demonstrated shortwave infrared spatial frequency domain imaging (SWIR SFDI) for wide-field tissue optical property measurements. Key design and performance characteristics such as portability, wavelength selection, measurement resolution, and the effect of skin have not yet been addressed for SWIR SFDI. In this chapter we aim to fabricate and characterize a SWIR SFDI system for clinical use. To achieve this aim, the optimal choice of wavelengths was identified based on optical property uncertainty estimates and imaging depth. A compact LED-based dual wavelength SWIR SFDI system was fabricated. A two-layer inverse model was developed to account for the layered structure of skin. Performance was validated using tissue-simulating phantoms and in-vivo measurements from three healthy subjects. The SWIR SFDI system developed has a μ_s' resolution of at least 0.03 mm^{-1} at 880 nm and 0.02 mm^{-1} at 1100 nm. The two-layer inverse model reduced the error in deeper layer μ_s' extractions by at least 24% in the phantom study. The two-layer model also increased the contrast between superficial vessels and the surrounding tissue for in-vivo measurements. The clinic-ready SWIR SFDI device is sensitive to small optical property alterations in diffuse media, provides enhanced accuracy in quantifying optical properties in the deeper layers in phantoms, and provided enhanced contrast of subcutaneous blood vessels.

The work in Chapter Three (except for 3.2.1) was published in the Journal of Biomedical Optics (JBO) in 2022 [28] with the following contributing authors:

Anahita Pilvar¹, Jorge Plutzky², Mark C. Pierce³, Darren Roblyer^{1,4}

¹*Department of Electrical and Computer Engineering, Boston University, 8 St Mary's St, Boston, MA 02215, USA.*

²*Brigham and Womens Hospital, Harvard Medical School, Department of Medicine, Boston, Massachusetts, United States*

³*Department of Biomedical Engineering, Rutgers, The State University of New Jersey, 599 Taylor Road, Piscataway, NJ 08854, USA.*

⁴*Department of Biomedical Engineering, Boston University, 44 Cummington Mall, Boston, MA 02215, USA.*

3.1 INTRODUCTION

The shortwave infrared (SWIR) optical window (approximately 900–2000 nm) has recently attracted interest for deep tissue imaging due to the lower scattering of light compared to the visible (VIS: 400–700) and near-infrared (NIR: 700–900 nm) wavelength bands [29]. SWIR imaging has accelerated in recent years due to the increased availability of SWIR-sensitive detectors [30]. The SWIR optical window has previously been explored for deep fluorescence imaging using NIR/SWIR fluorescence dyes for applications such as targeted cancer imaging and tumor surgery guidance [31, 32, 33]. Reflectance imaging in the SWIR optical window has been explored for determination of peripheral edema, skin burn and bruise imaging, but the planar reflectance data cannot reliably predict the optical properties of the tissue [27, 34, 35]. Techniques such as diffuse optical spectroscopy (DOS) and spatial frequency domain imaging (SFDI) are widely used to measure tissue optical properties in the NIR region, namely the absorption coefficient (μ_a) and the reduced scattering coefficient (μ_s'). SFDI measurements in the SWIR may be advantageous over other SWIR imaging techniques owing to its ability for quantitative assessment of tissue and blood optical properties. Compared to SFDI measurements in the NIR, SWIR SFDI is potentially capable of imaging deeper in tissue [36, 3, 37]. Additionally, SWIR SFDI is

sensitive to water and lipids, which makes the technique valuable for applications such as monitoring of volume status, tracking edema, and lipid measurements.

In our prior work, we developed a laser-based hyperspectral SWIR SFDI system with the ability to extract water and lipid concentrations in the tissue and blood of mice and humans [12]. We demonstrated that SWIR SFDI could be used to monitor tissue edema during inflammation, lipid content in tumors, and brown fat content in mice. A key experiment in that work was the measurement of non-invasive blood lipids before and after a high-fat meal using measured optical properties through intact skin. While preliminary, this demonstration suggests that one important application of SWIR SFDI may be the non-invasive assessment of tissue and blood nutrients and metabolites. Potential examples include blood lipids (e.g., triglycerides, cholesterol) and glucose, metabolic parameters that are often measured as critical parameters in clinical management. Current approaches to such measurements through phlebotomy or other invasive techniques pose significant issues: higher costs including technicians and chemical laboratories, risk for both patients and technicians, generation of waste and its safe disposal. Moreover, the ability to track changes in these parameters regularly, conveniently and over time with high accuracy is an important unmet clinical need for patients with life-threatening diseases such as diabetes and cardiovascular disease (CVD) [8, 19]. The potential for improved imaging depth with SWIR SFDI makes the measurement of subcutaneous tissue and blood a good fit for this technology but remains largely unexplored.

Our previously reported hyperspectral SWIR SFDI system [12] suffered from low acquisition speed and immobility given the use of a tunable Ti-Sapphire laser for sample illumination at wavelengths from 680 nm to 1300 nm. Additionally, the layered structure of skin during measurements of subcutaneous tissue and blood remained unaccounted for, likely leading to errors due to partial volume effects. These limitations, which represent

important obstacles toward extending SWIR SFDI to clinical applications, are addressed in data presented here.

In this study, we first describe the design of a new, portable, dual-wavelength SWIR SFDI instrument for measuring the optical properties of subcutaneous tissue and blood. We identify the optimal imaging wavelengths based on an analysis of optical property uncertainties and imaging depth. Next, we show results obtained by using a new two-layer inverse model of the skin. We then report in-vivo measurements from three healthy subjects and show enhanced contrast of superficial blood vessels with the two-layer model.

3.2 SWIR SFDI IMAGING BACKGROUND

SWIR SFDI has multiple potential advantages compared to VIS or NIR SFDI. First, the scattering of light generally decreases exponentially with wavelength in tissue at NIR and SWIR wavelengths, allowing for deeper light penetration at some SWIR wavelengths. This is especially true at wavelengths such as 1100 nm where the absorption from water, lipids, and collagen are at a local minimum [36, 3]. Second, the lower hemoglobin absorption and stronger absorption of water and lipids make measurements in the SWIR region more sensitive to water and lipid content. **Figure 3.1** shows the absorption and reduced scattering coefficient of human skin tissue in VIS-NIR-SWIR optical windows, highlighting both the reduced scattering and prominence of water and lipid absorption at wavelengths past 900 nm [2].

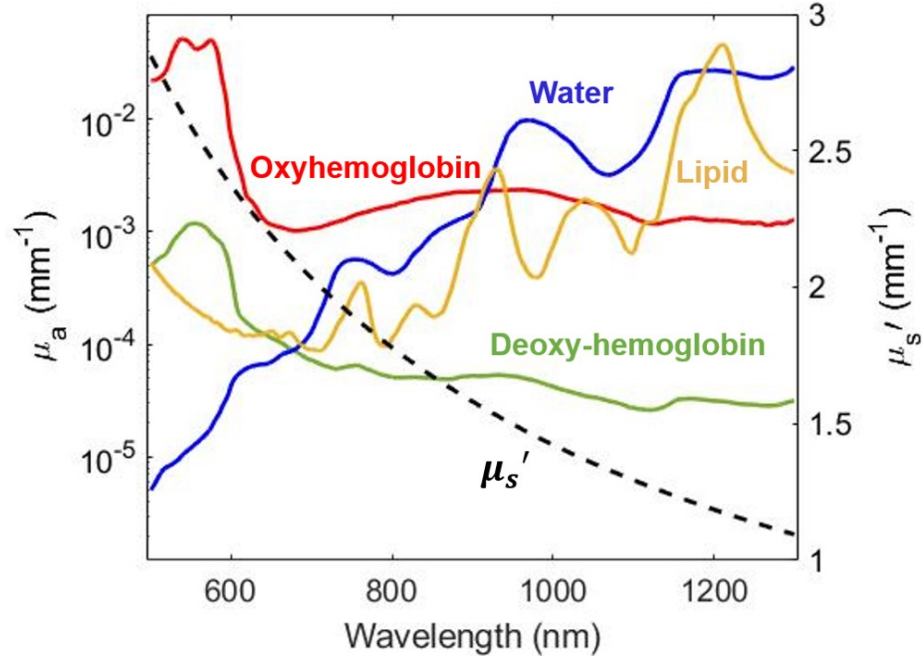


Figure 3.1: The absorption and reduced scattering of a representative human tissue from 500 nm to 1300 nm. Left y-axis: The absorption coefficients of oxyhemoglobin (7.74 μM), deoxyhemoglobin (0.12 μM), water (21.42%) and lipid (27.74%) represent previously published measurements taken from human subjects on the dorsal forearm with skin type I-II [2]. Left y-axis shown in log-scale. μ_a was calculated by multiplying the extinction coefficient by the concentration for each chromophore. Right y-axis: reduced scattering coefficient of human skin in linear scale.

3.2.1 Comparing SWIR SFDI to NIR SFDI and DOSI

There are several major advantages to using SFDI at SWIR wavelengths compared to SFDI at NIR and VIS wavelengths, as well as other diffuse optical imaging modalities such as DOSI. We can compare these techniques using various methods, such as directly comparing DOSI and SWIR SFDI in terms of spatial resolution and acquisition time on a tissue sample, as well as performing computational modeling to evaluate chromophore extraction error in SWIR SFDI versus SFDI in NIR and DOSI.

Table 4.3 demonstrates a comparison between NIR SFDI, DOSI and SWIR SFDI that we

previous published on, also known as SWIR-MPI [12], over several quantitative parameters (wavelength, spatial resolution, measurement type, chromophores available). SFDI works use 640 nm - 851 nm wavelengths in the NIR range (known as the first in-vivo imaging window) [10, 38]. DOSI uses 650 nm - 1000 nm wavelength region which is mostly in the NIR, and it also uses the first in vivo imaging window [39, 38]. In contrast, SWIR MPI utilizes 680 nm - 1300 nm wavelengths that cover large range of both NIR and SWIR, and can access the well-known second in vivo imaging window [12, 38]. In terms of chromophores, both DOSI and SWIR MPI can extract oxy-hemoglobin, deoxy-hemoglobin, water and lipids, whereas SFDI is only able to extract oxy- and deoxy-hemoglobins.

A major advantage of SWIR-MPI and SFDI over related diffuse optical technologies

Table 3.1: Comparisons between SFDI, DOSI, and SWIR-MPI.

Modality	Wavelength	Spectral range	Imaging window	Spatial resolution	Measurement	Chromophores
SFDI	640-851 nm	NIR	First in-vivo imaging window	<1 mm	Wide-field, non-contact	oxy- and deoxy-hemoglobin
DOSI	650-1000 nm	NIR	First in-vivo imaging window	5 mm-1 cm	point-by-point contact	oxy- and deoxy-hemoglobin, water and lipid
SWIR-MPI	680-1300 nm	NIR + SWIR	Second in-vivo imaging window	<1 mm	Wide-field, non-contact	oxy- and deoxy-hemoglobin, water and lipid

such as DOS and NIRS is its higher spatial resolution. While some versions of DOS can probe the same chromophore species as those of SWIR-MPI and SFDI (oxy-hemoglobin, deoxy-hemoglobin, water, and lipids), common implementations involve point-by-point measurements using a handheld probe [40], which is time consuming and typically has spatial resolution on the order of 1 cm [39]. In contrast, SWIR-MPI and SFDI operate in a non-contact manner with spatial resolution often finer than 1 mm [10].

As an experimental demonstration of the different spatial resolutions that can be attained by

SWIR-MPI and DOS (FDPM + CW), ex vivo porcine tissue with relatively rich fat deposits was measured by these two modalities and compared side-by-side. **Figure 3.2.A** shows a white light image of the tissue, where the white regions are fat deposits. The rectangular dashed boxes indicate measurement regions. **Figure 3.2.B-C** correspond to DOS measurements conducted with 10 cm \times 10 mm and 5 cm \times 10 mm grid spacing, respectively. Both water and lipid concentration maps, as well as optical property maps (μ_a and μ_s' , at 930 nm) are shown for comparison with SWIR-MPI in **Figure 3.2.D**. The dark blue areas in the DOS maps are due to removal of non-physiological values arising in data processing (such as an increase in scattering coefficient with wavelength). DOS is able to provide information on the samples lipid and water content, but the spatial resolution is relatively low. In contrast, SWIR-MPI (**Figure 3.2.D**) shows substantially finer resolution, and the spatial distribution of lipid-rich regions and muscle-fat margins are clearly visible. Note that typical DOS measurements are conducted with 1 cm spatial increments[39, 41, 42]. Here a 5 mm increment was also included to demonstrate that even with higher than typical sampling density, DOS still has a lower spatial resolution compared to SWIR-MPI. The extracted water and lipid values from DOS and SWIR-MPI are moderately different from each other due to the partial volume effect in a spatially heterogeneous sample and different probing depths. This side-by-side comparison shows that SWIR-MPI is able to provide much finer spatial information compared to DOSI, although in more superficial tissue.

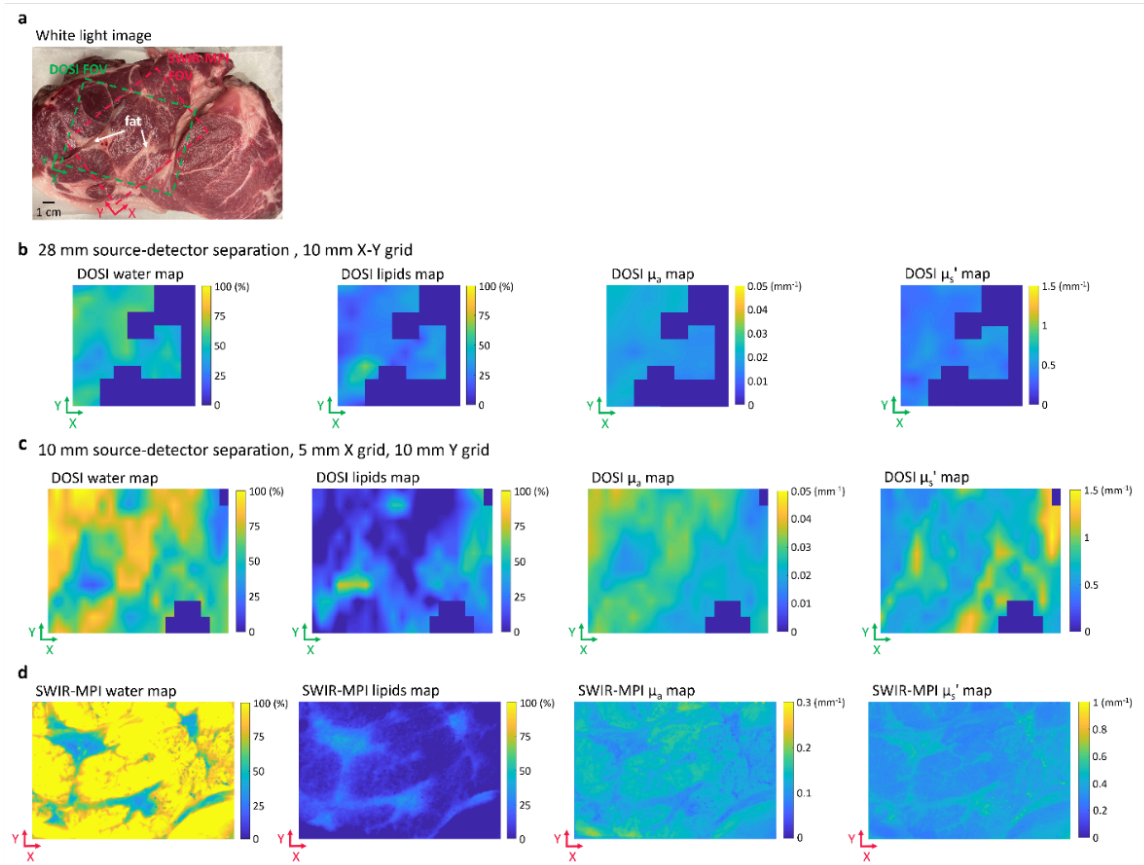


Figure 3.2: A) White light image of ex vivo porcine tissue measured by DOSI and SWIR-MPI. B) Water, lipid, and optical property maps (930 nm) measured by DOSI with a 10 mm sampling grid and 28 mm source-detector separation. C) Water, lipid, and optical property maps (930 nm) measured by DOSI with a 5 cm \times 10 mm sampling grid and 10 mm source-detector separation. D) Water, lipid, and optical property maps (1210 nm) measured by SWIR-MPI.

Next, we conduct numerical simulations on water and lipid extraction with the wavelengths utilized by the different modalities to help demonstrate the advantage SWIR SFDI has over NIR SFDI and DOSI in extracting accurate water and lipid concentrations in tissue. We utilized two different methodologies: condition number analysis and statistical simulations.

Condition number analysis for water and lipid extraction: Condition number analysis

is a method previously used for determining the measurement wavelengths that minimize crosstalk between absorbing chromophores [43]. The μ_a value at each wavelength is coupled with the chromophore concentrations through Beers law, shown in matrix form in **(Equation 3.1)**, where μ_a , λ , ϵ , and c refer to optical absorption, wavelength, chromophore extinction coefficient, and chromophore concentration, respectively.

$$\begin{bmatrix} \mu_a(\lambda_1) \\ \cdot \\ \cdot \\ \mu_a(\lambda_j) \end{bmatrix} = \begin{bmatrix} \epsilon_1(\lambda_1) & \dots & \epsilon_i(\lambda_1) \\ \cdot & \cdot & \cdot \\ \cdot & \cdot & \cdot \\ \epsilon_1(\lambda_j) & \dots & \epsilon_i(\lambda_j) \end{bmatrix} * \begin{bmatrix} c_1 \\ \cdot \\ \cdot \\ c_j \end{bmatrix} \quad (3.1)$$

The condition number of the extinction coefficient matrix (i.e. first term on the right-hand side of the equation) is defined as the ratio of the maximum and minimum singular values (SVD) of the matrix and can be used to quantify the sensitivity of the solution values to changes or errors in the input . A high condition number indicates an ill-conditioned problem where small changes in input values would result in large changes in the outputs. Thus, the optimal choice of wavelengths is the combination for which the condition number is minimized.

A map of condition numbers was generated by iterating wavelength pairs in the range of 700 nm to 1300 nm **(Figure 3.3)**. The extinction coefficient matrix was adapted from previous literature for water and lipids [44, 45]. The minimum condition number (2.52) occurs at the wavelength pair of 1212 nm and 1300 nm.

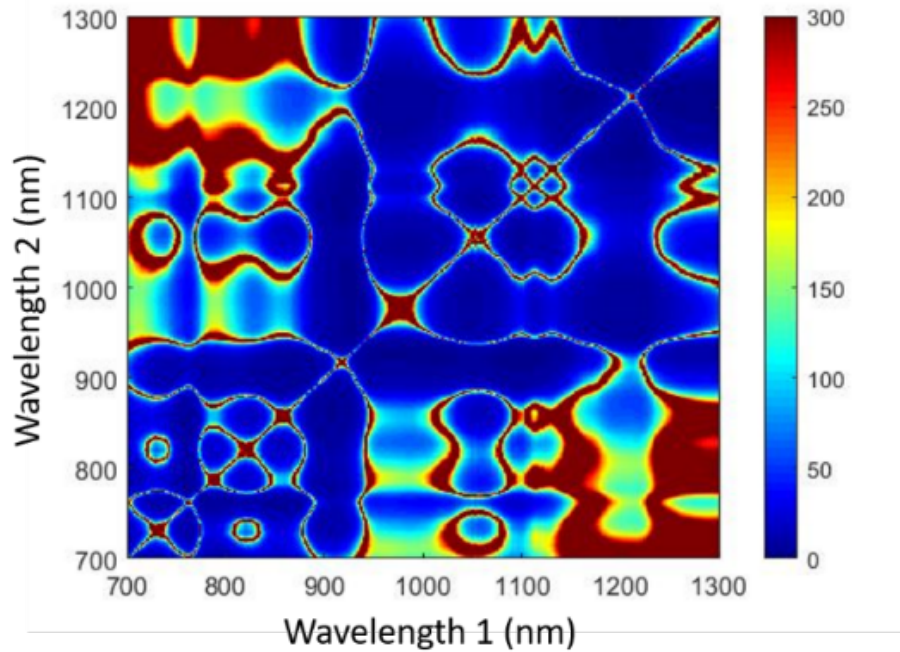


Figure 3.3: Condition number plot for extinction coefficient matrices containing values for water and lipid at wavelengths between 700 to 1300 nm.

Simulation for water and lipid extraction errors with different wavelengths:

While condition number analysis demonstrates the optimized wavelength pair in a noiseless scenario, the optimum choice of wavelength is also a function of measurement noise which is not accounted for in the analysis. To address this limitation, numerical simulations were used to estimate the percent error in chromophore extraction in the presence of noise, for each pair of integer wavelengths in the range of 700 nm to 1300 nm. 100 combinations of physiologically relevant water and lipid concentrations were randomly generated and their corresponding absorption spectra were calculated with noise added to the simulated absorption data. Finally, the chromophore concentrations were reconstructed from this simulated noisy absorption data at each wavelength pair and compared to the ground truth in terms of percent errors. **Figure 3.4.A** and **Figure 3.4.B** show the results of the numerical simulations for two different noise scenarios, one based on an experimental noise model

from a lab-based SWIR-MPI system [12], and one based on 5% zero-mean Gaussian noise. The absolute errors in water and lipid concentrations were calculated and the lower right of each figure panel shows the water extraction error and upper left shows the lipid extraction error. **Table 3.2** shows a comparison of water and lipid extraction errors for different noise models at their optimum wavelength pairs. The errors are also compared to the simulation results using 41 wavelengths in the SWIR region as well as the errors at the wavelength pair with the lowest condition number. The smallest errors in chromophore extraction generally occur at regions with low condition numbers; however, in this case the wavelength pairs that produced the lowest errors were 1150 and 1210 for the experimental noise model, and 920 and 1096 nm for the 5% Gaussian noise model.

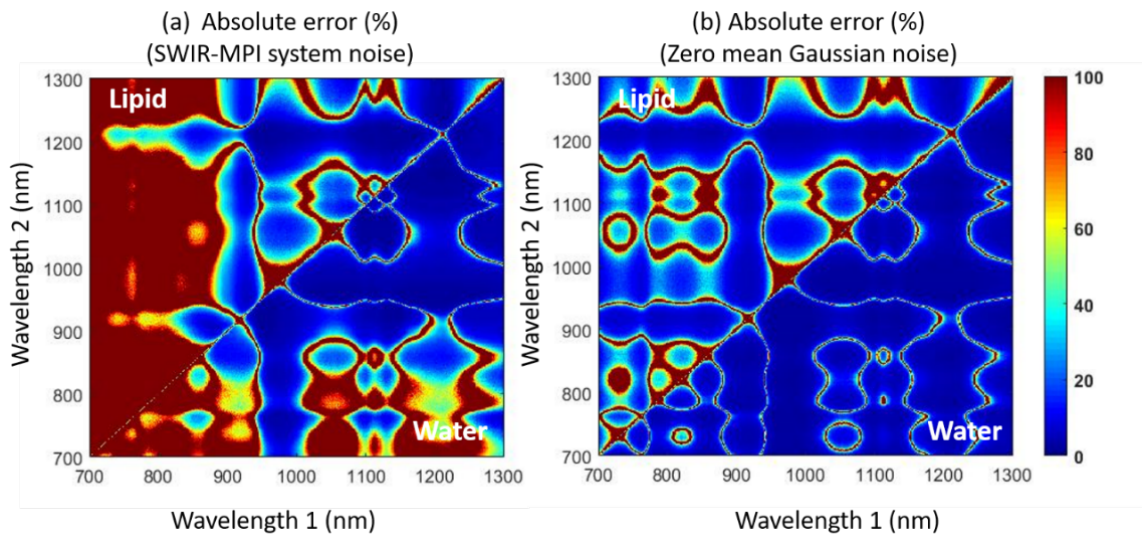


Figure 3.4: Average absolute errors in water and lipid extraction based on simulations with a) a model based on experimental SWIR-MPI system noise, b) a model assuming 5% zero-mean Gaussian noise.

Table 3.2: Comparison of water and lipid extraction errors for different wavelength pairs and noise models.

Wavelength (nm)	Condition number	Water error (5% Gaussian noise)	Lipid error (5% Gaussian noise)	Water error (SWIR-MPI noise)	Lipid error (SWIR-MPI noise)
900 – 10 – 1300	-	-0.00 ± 1.28%	0.00 ± 2.96%	3.17 ± 0.5%	-2.46 ± 1.12%
1212 & 1300	2.52	-0.02 ± 3.52%	-0.05 ± 5.22%	4.79 ± 0.54%	-2.86 ± 1.67%
920 & 1096	3.13	0.00 ± 3.88%	-0.01 ± 7.18%	4.87 ± 0.45%	-11.13 ± 2.71%
1150 & 1210	3.58	0.04 ± 4.44%	-0.09 ± 6.15%	0.69 ± 1.67%	0.19 ± 2.22%

3.3 SWIR SFDI DESIGN CRITERIA

3.3.1 Wavelength and spatial frequency selection

The choice of illumination wavelength and spatial frequency directly affects the uncertainties in calculated μ_a and μ_s' values. In our previous work, we developed a method based on the Cramer Rao Bound (CRB) to estimate optical property uncertainties in SFDI based on the experimental measurement of diffuse reflectance uncertainties as a function of wavelength, spatial frequency choice, and sample optical properties [46]. Here we used the CRB method to identify illumination wavelengths and spatial frequencies that minimizes the uncertainties in optical property measurements in the SWIR spectral band.

We first established a diffuse reflectance error model for our previous hyperspectral SWIR SFDI system. Since this system can take measurements over a wide wavelength range, it provides a means to directly compare uncertainties across wavelengths. A drift test was conducted over 5 hours from 4 intralipid samples with 2.5%, 5%, 7.5% and 10% lipid concentrations [12]. SFDI measurements were taken every 30 minutes from each sample (10 measurements at each concentration). The measurements were taken at 7 wavelengths from 700 nm to 1300 nm with 100 nm increments, and 8 spatial frequencies from DC to 0.5 mm^{-1} . The raw data at each wavelength and spatial frequency were converted to calibrated

diffuse reflectance using the calibration measurement taken from 10% intralipid prior to the experiment. The error model was constructed by averaging the ratio of standard deviation to the mean value (at each wavelength and spatial frequency) over the measurements (**Figure 3.5**). The calculated noise model was then used as input for the CRB algorithm, which converted the diffuse reflectance uncertainties to uncertainties in estimated optical properties. A Monte-Carlo based look-up table (LUT) inversion algorithm was used for all analyses.

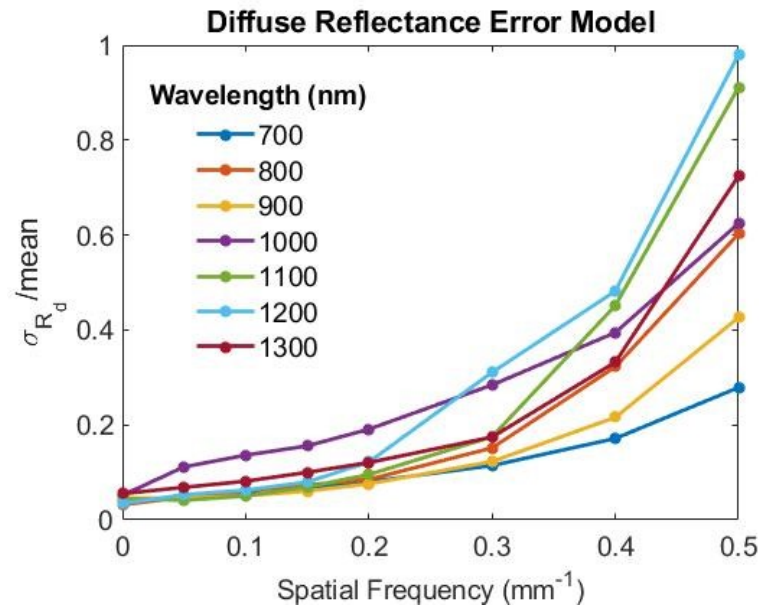


Figure 3.5: SWIR-MPI (meso-patterned imaging) noise model at seven wavelengths and eight spatial frequencies

We first identified the spatial frequency pairs that provided the lowest uncertainties across the range of tested wavelengths and physiologically relevant optical properties. The uncertainty estimates for μ_a and μ_s' were calculated for a wide set of spatial frequency pairs. Since uncertainties are also a function of sample optical properties, they were computed at five sets of previously measured optical properties that are representative of the dorsum of

the hand. The minimum uncertainties occurred when DC (0 mm^{-1}) illumination was paired with an AC illumination of either 0.1, 0.15, or 0.2 mm^{-1} , with only minor differences between these choices.

We then optimized the choice of illumination wavelengths to maximize the sensitivity of SFDI measurements to small changes in absorption and scattering properties of tissue and blood. **Figure 3.6** shows μ_a and μ_s' uncertainties across seven wavelengths from 700 to 1300 nm when using the spatial frequency pair DC and 0.15 mm^{-1} . The results show the smallest uncertainties in μ_a and μ_s' at 800 and 1100 nm, respectively. Smaller theoretical uncertainties suggest higher sensitivity to small changes in optical properties compared to the other tested wavelengths. While this analysis identified wavelengths with the lowest uncertainties, for many applications it is also important to evaluate the sensitivity of a measured parameter at a specific wavelength to the underlying changes in tissue (e.g. chromophore concentration changes or scattering changes).

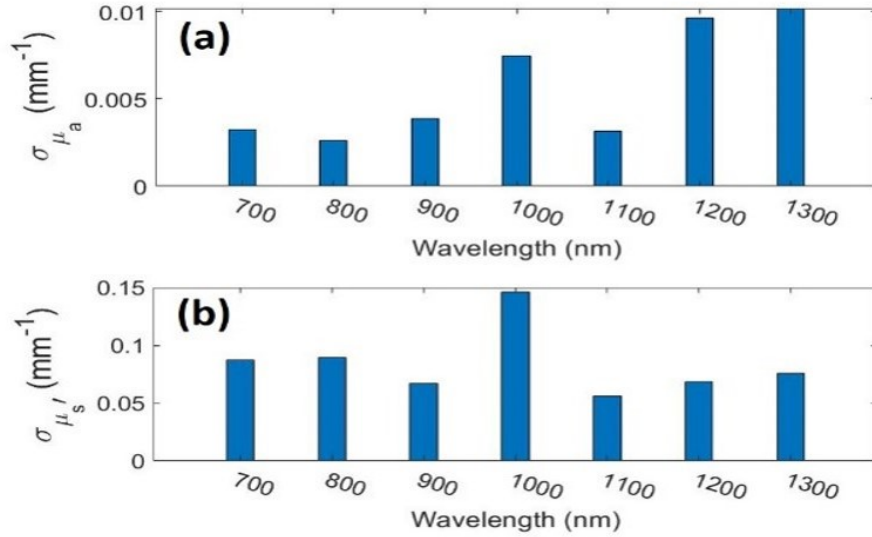


Figure 3.6: Cramer-Rao results for A) μ_a and B) μ_s' at spatial frequency of DC and 0.15 mm^{-1} .

Additionally, depth penetration was considered as an important metric for wavelength selection. Sensitivity to optical properties of the subcutaneous tissue and superficial blood vessels underneath the skin requires measurements that probe deeper than the dermal layer of skin. The thickness of human skin has previously been reported to be in the range of 0.5 to 2 mm [4, 5, 6]. We also sought to minimize the effect of highly absorbing chromophores present in skin epidermis layer, such as melanin, in order to have meaningful measurements in people with different skin tones [47].

To estimate the imaging penetration depth we used a Monte-Carlo based SFDI depth calculator reported in our prior work [48]. (Figure 3.7) demonstrates the 90th percentile of photon penetration depth for skin from 600 nm to 1800 nm at spatial frequencies of DC, 0.1 and 0.15 mm^{-1} [3]. The plot shows a maximum penetration depth at approximately

1100 nm, and also reveals that spatial frequencies up to 0.15 mm^{-1} pass through at least 1 mm of skin. The penetration depth results suggest that SFDI measurements taken at SWIR wavelengths and spatial frequencies of DC, 0.1 and 0.15 mm^{-1} are sensitive to the optical properties of the tissue and blood into the dermal layer, in some cases, below the dermal layer.

The CRB analysis suggests the use of 800 nm and 1100 nm for minimizing the uncertainties in μ_a and μ_s' extraction, respectively. These two wavelength are also in the spectral range where penetration depth is above 1 mm at spatial frequencies of DC to 0.15 mm^{-1} (**Figure 3.7**). The final choice of wavelength was made after searching through the available LEDs that provide high output power. While reviewing available parts from multiple suppliers, we ultimately chose Thorlabs LEDs, which are available over a wide wavelength range. 880 nm and 1100 nm center wavelength LEDs from Thorlabs provide high output power while also satisfy the other two wavelength selection criteria.

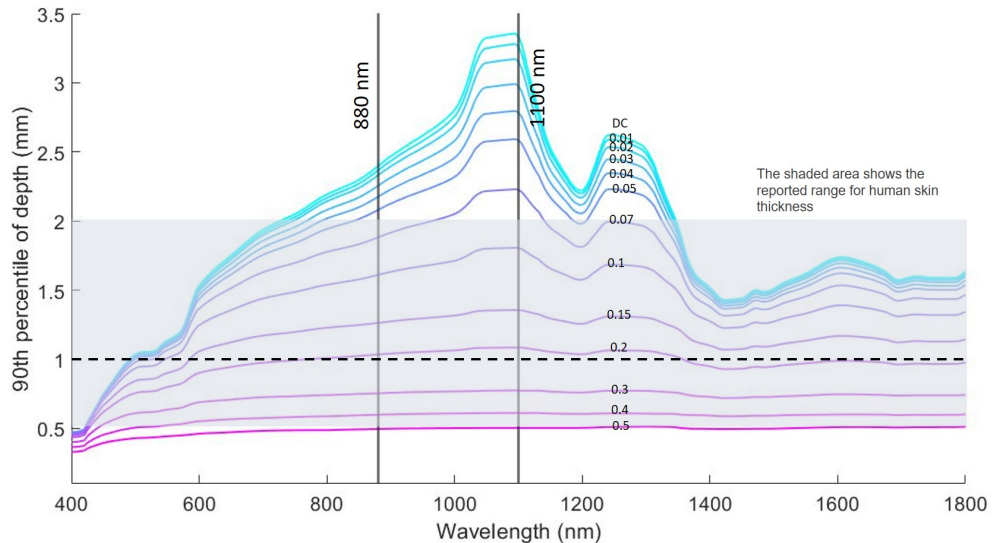


Figure 3.7: Photon 90th percentile depth penetration for skin optical properties at three spatial frequencies (DC, 0.1 mm^{-1} and 0.15 mm^{-1}) [3]. The shaded area shows the reported range for human skin thickness [4, 5, 6].

3.4 THE SWIR SFDI SYSTEM

A new LED-based SWIR SFDI system was designed and fabricated with the optimized wavelengths found in section 2.2. The system utilizes two LEDs, one at 880 nm in the NIR (M880L3, Thorlabs), and one at 1100 nm in the SWIR (M1100L1, Thorlabs) with 50 nm FWHM for both LEDs. The LEDs provided approximately 200 mW and 112 mW optical power at 880 nm and 1100 nm respectively. The optical power at sample plane is approximately $2.65 \mu\text{W}/\text{cm}^2$ at 880 nm and $3.1 \mu\text{W}/\text{cm}^2$ at 1100 nm. We followed the SFDI design steps that have been previously published by our lab and online in openSFDI.com and modified the design to build a compact and portable SFDI system [49].

Figure 3.8.a shows the SWIR SFDI system diagram. A long-pass dichroic mirror (DMLP1000, Thorlabs, cutoff wavelength = 1000 nm) directs the collimated light (collimating lens: ACL25416U-B, Thorlabs) from both LEDs to the DMD (LC4500, Keynote Photonics). The pattern from the DMD is being focused to the sample plane using an imaging lens (Ac254-050-B, Thorlabs). The projected light, which illuminates a large field of view (7x11 cm), is reflected from the sample and captured by a germanium CMOS camera (TriWave, Infrared Laboratories, Inc., Peabody, MA, USA) with a wide spectral sensitivity (300-1600 nm). A SWIR imaging lens was used with the camera (SR0510-A01, StingRay, Keene, NH, USA). A pair of crossed linear polarizers (LPNIRE100-B, Thorlabs) are placed in the illumination and detection paths to minimize the effect of specular reflection. The system is relatively fast (<1 min/whole sequence of DC + AC measurement, camera exposure time is 100 ms for each image at both wavelengths), compact and portable, making the system suitable for in-vivo and clinical measurements. **Figure 3.8.b** shows the fabricated system and **Figure 3.8.c** shows the representative images from the system captured at 800 nm as well as the processed images.

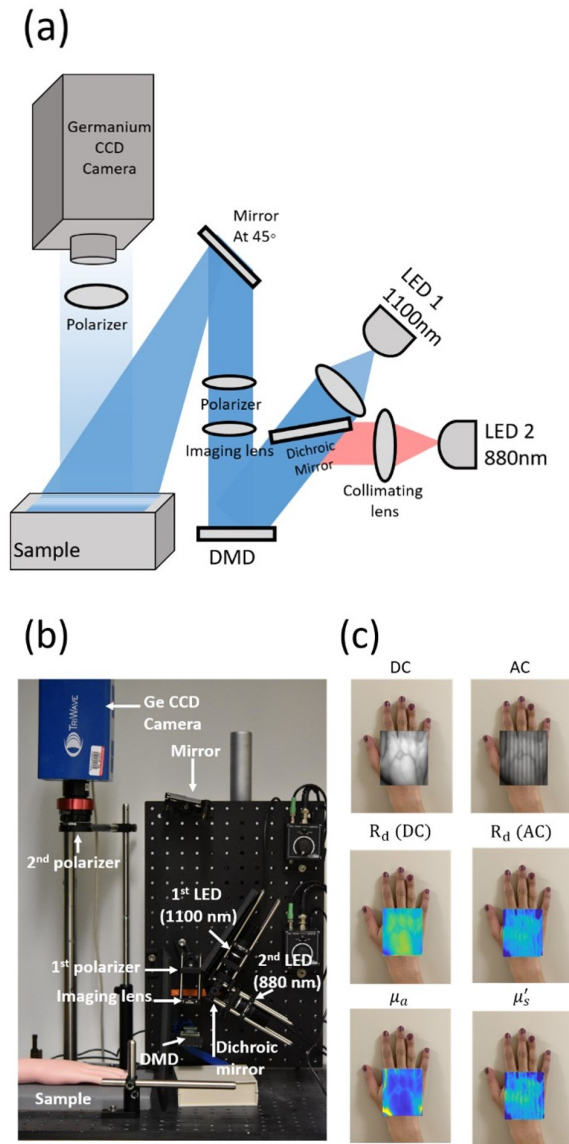


Figure 3.8: A) Schematic diagram of the SWIR SFDI system. Light from the two LEDs is collimated and combined at a dichroic mirror. The DMD generates the spatially modulated light that projects onto the sample with an achromatic lens. Two linear polarizers are placed in the illumination and detection path to reject specular reflection. B) The fabricated SWIR SFDI system. C) Representative images from the system captured at 880 nm. Top row represents the raw images with DC and AC illumination patterns superimposed on the white light image of the hand taken with a camera phone. The middle row represents the calibrated diffuse reflectance at two spatial frequencies. Bottom row shows the optical property maps (μ_a and μ'_s).

3.5 CALIBRATION AND IN-FRAME PHANTOM CORRECTION

Demodulated DC and AC images were converted to diffuse reflectance images by measuring a phantom with known optical properties. A Monte Carlo (MC) based forward model of diffusive light propagation was used to extract the diffuse reflectance (R_d) of the calibration phantom based on its known optical properties. Here we used a 10% intralipid suspension as the calibration phantom. The reduced scattering coefficient ($\mu_s' = \mu_s (1-g)$) of 10% intralipid suspension was adapted from Flock et al. Specifically, we assumed μ_s' decreased exponentially with wavelength and the anisotropy factor (g) decreased linearly with wavelength per the equations provided in Flock et al [50]. The absorption coefficient was calculated using pure water and lipid extinction spectra [44, 51] with Beers law. We ended up using $[\mu_a \ \mu_s']$ pair of $[0.0054 \ 3.64] \text{ mm}^{-1}$ at 880 nm and $[0.0181 \ 2.64] \text{ mm}^{-1}$ at 1100 nm for the calibration phantom. For the forward model used in the calibration process, intralipid was defined as a homogeneous semi-infinite medium with g and index of refraction (n) set to 0.7 and 1.33, respectively. These values were also adapted from Flock et al. [50].

A small 10% intralipid phantom (1 x 2 x 2 cm) was placed in the field of view as a gold standard phantom with known and stable optical properties. Assuming that the optical properties of the in-frame phantom do not change over time, we expect the R_d values of the in-frame phantom to stay constant during measurements. For each measurement, the extracted R_d values of the in-frame phantom were compared to the gold standard R_d values (predicted by the Monte Carlo model) at each wavelength and spatial frequency. Any discrepancy between the measured R_d values and the gold standard values of the in-frame phantom translates into correction factor and were used to correct the R_d values of the entire field of view. This method was described in our prior work [52].

3.6 SYSTEM CHARACTERIZATION

To characterize the precision of the system, a repeat test measurement was performed by taking 10 back-to-back measurements of a 10% intralipid suspension at $f_x = \text{DC} \ \& \ 0.15 \text{ mm}^{-1}$. The measured optical properties over the region of interest spanning the intralipid surface (approximately 2 x 2 cm, 14400 pixels) were averaged and the standard deviation of the mean values over these 10 measurements were calculated. The coefficients of variation of the repeat measurements for μ_a were 1.55% and 0.80% for 880 nm and 1100 nm (standard deviation $5.4 \times 10^{-4} \text{ mm}^{-1}$ and $1.31 \times 10^{-4} \text{ mm}^{-1}$). These values for μ_s' were 0.20% and 0.21% for 880 nm and 1100 nm (standard deviation 0.0074 mm^{-1} and 0.0057 mm^{-1}).

We also calculated the theoretical precision of the system by conducting the CRB analysis with the noise model of the dual-LED system. The dual-LED system outperforms the laser-based system (smaller noise and higher precision), and the spatial frequency of 0.1 and 0.15 mm^{-1} paired with DC appear to be the optimized choice with the new system as well.

To characterize the measurement resolution of μ_s' extractions, intralipid samples with 19 different concentrations ranging from 1.55% to 2.45% with 0.05% increments were measured. **Figure 3.9** shows the mean and standard deviation of the extracted optical properties from these measurements. The absorption remained almost unchanged over the different intralipid concentrations (**Figure 3.9.a**), while the reduced scattering increased gradually with increasing lipid concentrations (**Figure 3.9.b**). **Figure 3.9.c** shows the histogram of μ_s' values for three different intralipid concentrations at 0.05% increments. Changes as small as 0.05% in lipid concentration resulted in statistically significant alterations in measured μ_s' values ($p < 0.0001$ using pairwise Students t-test). The 0.05% lipid increment translates to an μ_s' increase of approximately 0.03 mm^{-1} at 880 nm and approximately

0.02 mm^{-1} at 1100 nm, indicating the $\mu_{s'}$ resolution of the system is at least this small for the imaging parameters utilized. **Figure 3.9.d** shows the imaging contrast in $\mu_{s'}$ of four intralipid suspensions from 2.0% to 2.3% at 880 nm and 1100 nm.

We used the results from the intralipid titration experiment to evaluate the accuracy of the optical property extraction. We compared the measure μ_a values to the ground truth values calculated using the Beers law. The SWIR SFDI results show on average 9.65% error (0.00055 mm^{-1} absolute error) in extracted μ_a at 880 nm and 1.30% error (-0.00008 mm^{-1} absolute error) in extracted μ_a at 1100 nm. For $\mu_{s'}$ we expect to see a linear increase in $\mu_{s'}$ with increasing lipid concentration. Going from 1.55% to 2.45% lipid concentration we expect to see a 1.58 fold increase in $\mu_{s'}$. The measured $\mu_{s'}$ values show 1.56 fold and 1.50 fold increase at 880 nm and 1100 nm, respectively, closely matching expectations.

Intralipid Titration

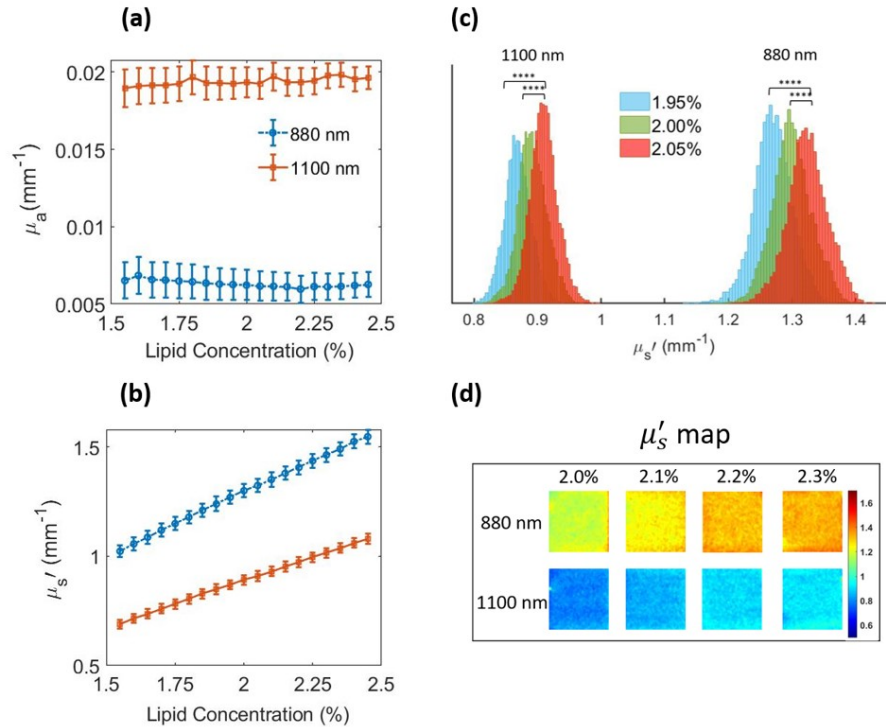


Figure 3.9: Results of an intralipid titration experiment to characterize the measurement sensitivity of SWIR SFDI to lipid concentration increments of 0.05% at 880 nm and 1100 nm. A) The measured absorption coefficient stayed largely unchanged when lipid concentrations were increased from 1.55% to 2.45%. B) The measured reduced scattering coefficient increased with increasing intralipid concentrations. C) Histograms of μ_s' pixel values from three consecutive measurements in the lipid titration experiment. The differences between the distribution of measurements of 1.95%, 2.0% and 2.05% lipid concentration were statistically significant (**** indicates $p < 0.0001$, determined with Student's t-test). D) μ_s' maps of four intralipid suspensions from 2.0% to 2.3% concentrations. All four concentrations were placed in the same field of view and measured simultaneously.

3.7 TWO-LAYER MODEL

Here we developed a two-layer inverse model to better extract the optical properties of subcutaneous tissue and blood. Our group has previously developed a Monte Carlo based

two-layer lookup table (LUT) inversion model that accounts for the effect of mouse skin during preclinical tumor SFDI imaging in the NIR [53]. In this prior work, the two-layer LUT reduced the errors in optical property extraction from the second, deeper, layer in both a two-layer phantom study and in an in-vivo mouse study. Here we used similar methods to account for the effect of human skin properties on the optical properties extracted from subcutaneous tissue and blood. The Gardner MC method, which obtains R_d estimates naively in the spatial frequency domain, was used to generate the two-layer LUT [54]. The top layer represents the human skin layer with fixed optical properties and thickness. The bottom layer is a semi-infinite geometry with optical properties as free parameters of the inversion algorithm. MC simulations were conducted using the Boston University shared computer cluster. We launched 10^7 photons for each simulation and a total of 160 simulations were conducted (one for each μ_s' value). μ_a was set to 0.0005 mm^{-1} for the bottom layer for MC simulations. The result from each simulation were then post processed using Beers law to achieve the bottom layer μ_a range for the two-layer LUTs.

A phantom validation study was conducted to evaluate the effect of using the two-layer model to perform optical property extractions. We first used 5% intralipid to fabricate a skin mimicking phantom with optical properties similar to human skin in the 1000-2200 nm wavelength range [55]. The phantom was made by mixing intralipid with agar powder and heating the mixture to form a solution, which formed a solid phantom after cooling. The optical properties of the phantom were measured using the SWIR SFDI system. We used the average optical properties of the phantom measured at 880 nm and 1100 nm to set the top layer μ_a and μ_s' values to 0.004 and 0.88 mm^{-1} , respectively. The anisotropy factor and refractive index were set to 0.7 and 1.33 for both top and bottom layers to match the properties of intralipid [50]. The average thickness of human skin was reported as 1 mm and was set as a fixed parameter in MC simulations [4, 5].

A set of two-layer phantoms were fabricated to validate the two-layer LUT inverse model with the top-layer mimicking the skin tissue thickness (1 mm) and optical properties using 5% intralipid solid phantom. The skin-mimicking phantom was placed on top of the bottom liquid phantoms which consist of four intralipid suspensions from 2% to 5% lipid concentrations. SFDI measurements were taken from the two-layer phantoms and processed using both one-layer and the new two-layer LUT. **Figure 3.10.a** shows the geometry of the two-layer MC simulations as well as a picture of 1 mm thick skin phantom used in the phantom study. **Figure 3.10.b** shows the average error in extracted μ_s' from the bottom layer from the four intralipid suspensions. The two-layer model improves the accuracy of bottom layer μ_s' extraction by 33.9% and 24.5% for 880 nm and 1100 nm, respectively. The two-layer LUT however does not improve the error in the extracted μ_a , and errors for both the one-layer and two-layer LUTs were approximately 50% at both wavelengths, although this corresponds to a small absolute error of approximately 0.005 mm^{-1}).

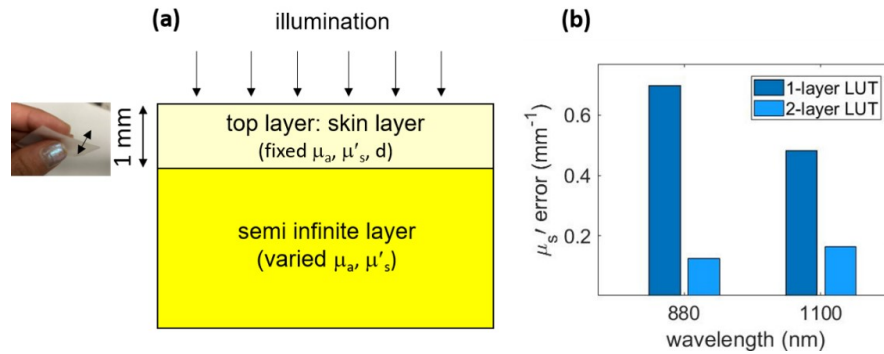


Figure 3.10: A) A schematic of the two-layer MC simulation geometry. The inset shows a 1 mm thick skin-simulating phantom made with intralipid and agar. B) Comparison of bottom layer μ_s' measured using one-layer and two-layer LUTs. The absolute extraction errors for μ_s' are shown.

The parameters of the two-layer LUT were then modified for human measurements. A second two-layer LUT was generated with a g value of 0.9 for both the skin layer and

the semi-infinite bottom layer. The refractive index was set to 1.37 for the skin layer [3, 55] and 1.4 for the bottom layer. The μ_a value for the skin layer was set to 0.024 mm^{-1} [3]. The μ_s' of the skin layer was set to 0.88 mm^{-1} , which matches the μ_s' of the LUT used in the phantom study and lies in the range reported for skin at 1100 nm [3, 56]. A third two-layer LUT was generated using μ_s' of 1.25 mm^{-1} , which matches the optical properties of skin at 880 nm [56, 57]. The same μ_a value of 0.024 mm^{-1} was used for both of these two-layer LUTs.

For the newly generated two-layer LUT, an additional round of CRB analysis was conducted for spatial frequency selection. While the prior analysis for a single layer media indicated that DC illumination paired with an AC spatial frequency of 0.1, 0.15, or 0.2 mm^{-1} had approximately equivalent performance, the two-layer analysis indicated that DC and 0.1 mm^{-1} had superior performance compared to the other choices when attempting to extract the deeper layer optical properties. This is likely due to the deeper imaging depth of 0.1 mm^{-1} versus 0.15 or 0.2 mm^{-1} (**Figure 3.7**). Subsequent human measurements were collected using $f_x = \text{DC}$ and 0.1 mm^{-1} .

We note that we also tried the model with $g = 0.3$ which is closer to the reported g value in [58] for intralipid. The different models have a relative bias of 0.0009 and 0.0037 mm^{-1} in μ_a , and 0.34 and 0.26 mm^{-1} in μ_s' at 880 and 1100 nm respectively, but the choice of model with different g value did not affect the performance characteristic of the system and the performance of the two-layer model.

3.8 IN-VIVO BLOOD AND TISSUE MEASUREMENTS

SWIR SFDI measurements were performed on the dorsal surface of the hand of three subjects: one 28 year old female and two 28 year old male subjects. The measurements were conducted under an institutionally-approved protocol (protocol number 4698). Sub-

jects were informed about the study and provided informed consent prior to the experiment. The optical properties extracted when using the one-layer and two-layer LUTs were compared over large superficial vessel regions (dorsal metacarpal veins in the hand) and the surrounding tissue. The results from using each LUT were compared in terms of the contrast between the optical properties of superficial vessels and the surrounding tissue using line profiles. In **Figure 3.11.a-b**, optical property maps for the dorsum of the hand at 880 and 1100 nm are shown for subject #1 using the one-layer LUT and the two-layer LUTs. The line profiles are plotted over the red dashed line in **Figure 3.11.b** for both μ_a and μ_s' (**Figure 3.11.c-d**). The contrast between the metacarpal veins and the surrounding tissue on the hand increases for both μ_a and μ_s' when using the two-layer LUT compared to the one-layer LUT for all volunteers. We calculated the contrast over the line profile using the following equation (Weber contrast) at each wavelength and optical properties (mu refers to scattering or absorption coefficient):

$$C = \frac{\mu_{Max} - \mu_{Min}}{\mu_{Min}} \quad (3.2)$$

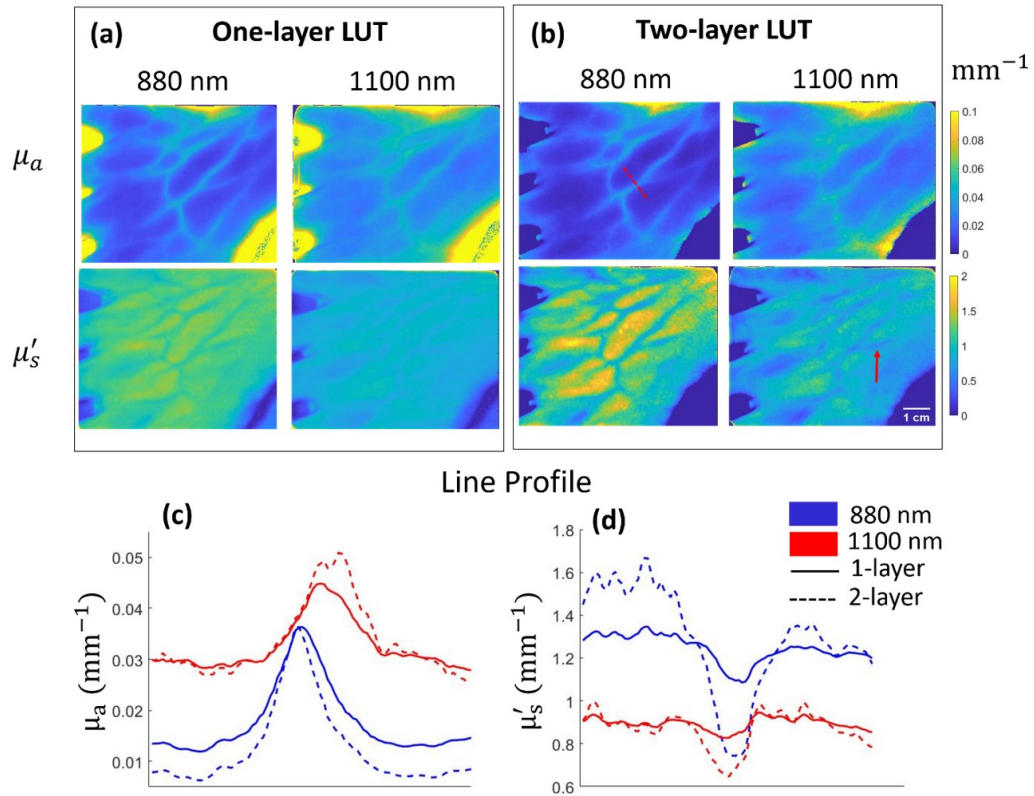


Figure 3.11: Healthy volunteer results (subject #1) from the dorsum of the hand. A) Optical property maps at 880 nm and 1100 nm using one-layer LUT and B) two-layer LUTs. C) Line profiles over the dotted red line for μ_a and d) μ_s' . Blue shows the line profiles at 880 nm and red shows the line profiles at 1100 nm. The solid lines correspond to the one-layer LUT results and dashed lines correspond to the two-layer LUT results. The use of the two-layer LUT enhances the contrast of the superficial blood vessel especially in μ_s' . The red arrow in D) shows an example of a vessel-like structure that is identified in μ_s' map but not in μ_a map at the same wavelength.

On average, we saw a 352% and 223% increase in μ_s' contrast and 104% and 61% increase in μ_a contrast at 880 and 1100 nm, respectively, averaged across all subjects over a designated superficial vessel on the hand. Table 1 summarize the contrast ratio (shown as percentages) between a superficial vessel and its surrounding tissue at both wavelengths and optical properties using one-layer and two-layer LUTs for all subjects. These results

suggest that two-layer LUTs provide increased sensitivity to the large superficial blood vessels. We noted that some image features, e.g. vessels could be identified in the μ_s' map while they cannot be identified in the corresponding μ_a map. One example is designated by the red arrow in **Figure 3.11.b**. We note that the optical property maps and the contrast values represent the bottom layer when using the two-layer LUTs.

3.9 DISCUSSION

In this work, we have designed and validated a new dual-LED SWIR SFDI system for non-invasive measurement of tissue and blood optical properties. We identified optimal wavelengths and spatial frequencies for accurate estimation of optical properties, and we developed a two-layer model to improve the sensitivity of SFDI measurements to subcutaneous tissue and blood. The portable SWIR SFDI system was fabricated using two LEDs at 880 nm and 1100 nm. The spatial frequency pairs of DC-0.15 mm^{-1} and DC-0.1 mm^{-1} were used for homogenous phantom and two-layer phantom/in-vivo measurements, respectively. The new SWIR SFDI system is fast (<1 min measurement time for 2-wavelength measurements), compact and portable, which are distinct advantages compared to our previous hyperspectral SWIR SFDI system, which took approximately 2 minutes and 15 seconds for 2-wavelength measurements. The new system is sensitive to small optical property alterations with the μ_s' resolution at least 0.03 mm^{-1} at 880 nm and at least 0.02 mm^{-1} at 1100 nm.

The two-layer model developed here decreased errors by at least 24% in the extracted bottom layer μ_s' compared to the homogenous model in the two-layer phantom study. However, it did not result in an improvement in bottom layer μ_a estimation. Similarly, the estimated μ_a in the in-vivo measurements were less affected by the use of the two-layer inverse model compared to the estimated μ_s' . One possible explanation is the similarity between

top and bottom layer μ_a in the phantom study. We used 5% intralipid suspension to fabricate the skin phantoms and the bottom layer consisted of four intralipid suspensions with 2-5% lipid concentrations. The μ_a of intralipid at 880 and 1100 nm is minimally affected by the alteration in lipid concentrations over the 2-5% range ($\mu_a(\text{at } 880 \text{ nm}) = 0.0056\text{-}0.0057 \text{ mm}^{-1}$ and $\mu_a(\text{at } 1100 \text{ nm}) = 0.0189\text{-}0.0195 \text{ mm}^{-1}$ for 2% lipid concentrations). Since both layers had similar μ_a values, the error in the extracted μ_a was minimally affected when using either the one-layer or two-layer LUT.

The use of the two-layer model revealed higher contrast between superficial vessels and their surrounding tissue compared to the homogeneous, one-layer model for in-vivo measurements of the hand. The optical absorption of blood is known to be substantially higher relative to skin and optical scattering of blood is often reported to be lower relative to skin [59, 60]. The higher contrast between superficial vessels and the surrounding tissue at both μ_a and μ_s' can be interpreted as an improved sensitivity to optical properties of blood (i.e., μ_a increased more dramatically over vessels and μ_s' decreased more dramatically over vessels compared to the single-layer LUT results). The optical properties of the tissue surrounding the superficial vessels stayed relatively unchanged when using either the single or two-layer LUTs for 1100 nm, but changed more substantially for 880 nm. This is possibly because the two-layer model helped to account for the effect of melanin absorption in the epidermis on the extracted μ_a at this wavelength, and it is known that melanin absorption is stronger at 880 nm compared to 1100 nm [61].

SWIR SFDI suffers from a few important limitations. First, SFDI measurements are limited by a partial volume effect when measurements are taken on a heterogeneous media. In this work, we attempted to mitigate the effect of skin on subcutaneous optical property extraction by using a two-layer inverse model. Here, fixed optical properties and thickness for the skin were assumed in our model, which may reduce applicability to different body

locations with different skin thickness and different skin tones; such adjustments however can be made for different measurement locations. Although SWIR wavelengths benefit from lower melanin absorption compared to the VIS-NIR optical window, people with different skin tones may have distinct skin optical properties [2, 61]. Further study is required to investigate the effect of the two-layer model on optical property extraction from subjects with different skin tones. Additionally, while the dual-LED SWIR SFDI system developed here has distinct advantages for clinical use, including being label-free, non-contact, with a relatively high acquisition speed, the fabrication cost is high compared to other VIS/NIR SFDI systems due to the high cost of the SWIR camera (currently scientific grade InGaAs SWIR cameras can cost well over \$10k USD).

3.10 CONCLUSION

In conclusion, we have developed a clinic ready dual-LED SWIR SFDI system. We have generated a new two-layer inverse model that accounts for the layered effect of skin, validated this system and the model through measurements in phantom models as well as the hands of three healthy volunteers. Although additional development and study are needed, this SWIR SFDI system can measure the optical properties of tissue and blood. As such, this technology has the potential to provide a powerful novel tool for multiple clinical applications in a safe, cost effective, and efficacious manner for conditions such as cardiovascular diseases and diabetes.

CHAPTER 4

Feasibility of postprandial optical scattering of lipoproteins in blood as an optical marker of cardiovascular disease risk: modeling and experimental validation

Blood lipid levels (i.e., triglycerides (TG) and cholesterol) are highly predictive of cardiovascular disease (CVD) risk. Current methods for measuring blood lipids require invasive blood draws and traditional lab testing, limiting their practicality for frequent monitoring. Optical measurements of lipoproteins, which carry TG and cholesterol in blood, may provide simpler invasive or non-invasive methods for more frequent and rapid blood lipid measurements. In this work, we investigated the effect of lipoproteins on optical properties of blood before and after a high-fat meal (i.e., the pre- and post-prandial state). To do this, we conducted simulations using Mie theory which were supported by literature review to identify key parameters including specific lipoprotein size distributions and number density. We also conducted experimental validation of ex-vivo blood samples. Our results show that lipoproteins in blood, particularly very low density lipoproteins (VLDL) and chylomicrons, are highly scattering in the visible and near-infrared wavelength region. Estimates of the increase in the reduced scattering coefficient (μ_s') of blood after a high-fat meal ranged from 4% for a healthy individual, to 15% for those with type 2 diabetes, to up to 64% for those suffering from hypertriglyceridemia at 730 nm. A reduction in blood scattering anisotropy (g) also occurred as a function of lipoprotein concentration increase. These findings lay the foundation for future research in the development of optical methods for invasive and non-invasive optical measure of blood lipoproteins, which could improve early detection and management of CVD risk.

The work in Chapter four was published in the Journal of Biomedical Optics in 2023 [62] with the following contributing authors:

Anahita Pilvar¹, Declan W.Smith², Jorge Plutzky³, Darren Roblyer^{1,4}

¹*Department of Electrical and Computer Engineering, Boston University, Boston, MA 02215*

²*Department of Physics, Boston University, Boston, MA 02215*

³*Department of Medicine, Brigham and Womens Hospital and Harvard Medical School, Boston, MA 02115*

⁴*Department of Biomedical Engineering, Boston University, Boston, MA 02215*

4.1 INTRODUCTION

Plasma lipoproteins, which are complex biochemical particles that transport hydrophobic lipids through the blood, are largely unrecognized as a potential optical biomarker for the evaluation of cardiovascular health. Lipoprotein particles are known to be partially responsible for blood plasma turbidity, and they very likely affect total blood optical properties. Plasma levels of triglyceride and cholesterol, which are packaged and transported in blood within lipoproteins, are strongly predictive of future cardiovascular events, including heart attack and stroke [8, 18]. Currently, measurement of these plasma blood lipids requires invasive blood draw and traditional laboratory-based testing. Label-free optical measurements of blood lipoproteins, and their changes after dietary fat ingestion, may have important implication for cardiovascular health assessment, especially for those suffering from dyslipidemias such as type 2 diabetes [63].

The optical properties of blood have been a topic of interest for many years with implication in variety of diagnostic and therapeutic applications and blood quality assessment. Both the absorption and scattering properties of blood are dominated by red blood cells (RBCs), which account for approximately 36% to 54% of human blood [64]. Hemoglobin, which accounts for approximately 95% of the volume of red blood cells, is responsible for

the optical absorption of blood, especially at visible and near infrared wavelengths [65]. At longer wavelengths (>1000 nm), blood absorption is dominated by the optical absorption of water which accounts for around 90% of blood plasma. The scattering properties of blood are largely a consequence of the refractive index mismatch between RBCs and blood plasma, but also affected by the size, shape, orientation, and concentration of the RBCs as well as other cells, proteins, vesicles, and other scattering particles. There have also been investigations of how glucose can alter blood and tissue optical scattering, with prior work demonstrating a decrease in tissue optical scattering due to elevated levels of glucose caused by a closer matching of refractive index between the extracellular fluid and cellular membrane [66].

While less explored, lipoproteins are also likely to alter blood optical properties, especially optical scattering. Triglyceride rich lipoproteins (TRL) including chylomicrons and very low density lipoproteins (VLDL), are large (20 - 1200 nm in diameter) [67, 68] and have a substantial index of refraction mismatch from plasma. Due to their size and refractive index, TRLs provide a strong source of Mie scattering to visible and NIR light. There has been very little prior work investigating how naturally occurring lipoproteins affect blood optical properties, which represents a potential missed opportunity for both invasive and non-invasive optical health monitoring.

In this work we utilized both computational modelling and experimental measurements to quantify the effect of lipoproteins on the optical properties of blood. In the sections, below we build towards a realistic estimate of the changes in human blood optical properties after a high-fat meal. We first described the basic properties of plasma lipoproteins. We then conducted a series of simplified experiments to test the effect of added lipoprotein-like particles on the optical properties of blood, which are measured using a technique called spatial frequency domain imaging (SFDI) [28]. We used Mie theory to

both validate the experimental results and quantify the effect of so-called dependent scattering, which occurs because of the close spacing of red blood cells in plasma. Next, we utilized extensive literature review to estimate expected fasting and postprandial (i.e., after a meal) lipoprotein size distributions, concentrations, and temporal dynamics. Finally, we used these parameters as part of a more comprehensive model to provide predictions of expected scattering changes in blood following a high fat meal for both healthy individuals and patients with dyslipidemias. Together, this work provides an important framework for the development of optical methods to detect lipoproteins in blood.

4.2 THE BASIC PROPERTIES OF PLASMA LIPOPROTEINS AND THEIR SYNTHESIS

Plasma lipoproteins are classified according to their density into several particle types, including chylomicrons, very low density (VLDL), low density (LDL), intermediate density (IDL) and high density (HDL) lipoproteins. Of these, chylomicrons have both the lowest density and the largest size, typically ranging between 75 nm and 1200 nm [67, 68]. After fat intake, dietary lipids including triglycerides and cholesterol are packaged into large triglyceride rich lipoproteins (TRL) (i.e., chylomicrons) in enterocyte cells in the small intestine and enter the bloodstream via the lymphatic ducts [67]. Chylomicrons deliver dietary fat to tissues throughout the body, after which they transform into smaller particles called chylomicron remnants, which are taken up by the liver. VLDLs are also TRLs, and have lower triglyceride and higher cholesterol levels compared to chylomicrons. VLDLs are the endogenous source of triglyceride and are synthesized in the liver before entering the blood circulation. They are smaller than chylomicrons with diameters ranging from 30 - 80 nm [67]. Both VLDL and Chylomicron are spherical micelles that

are composed of a monolayer phospholipid shell that protects the hydrophobic core of triglyceride and cholesterol.

Figure 4.1 summarizes the blood triglyceride pathways including the exogenous pathway, in which ingested fats are packaged in chylomicrons, as well as the endogenous pathway, in which the liver produces VLDLs. Chylomicron and VLDL particles account for most of the blood triglyceride levels and their concentrations are highly influenced by food intake. As we will show, these TRL particles are a strong source of Mie scattering due to their size and other important properties. Smaller cholesterol-rich particles such as LDL, IDL, and HDL are unlikely to provide substantial optical scattering in the visible and near-infrared wavelength bands.

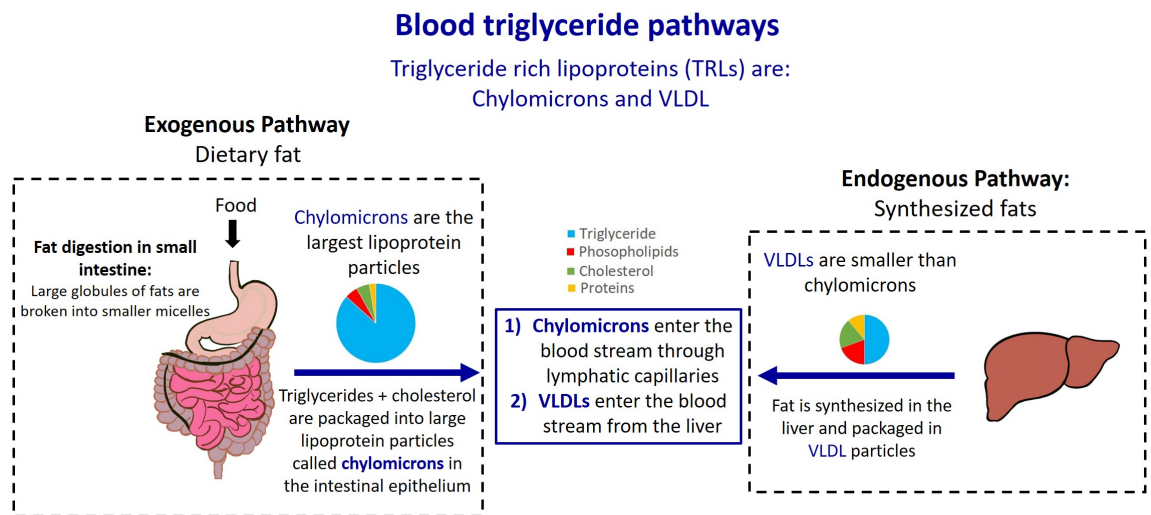


Figure 4.1: Blood triglyceride pathways: Chylomicron and VLDL are the main source of blood triglycerides (TG). Chylomicrons enter the blood through the small intestine after dietary fat intake and hence they are the exogenous source of blood TG. VLDLs enter the blood through the liver and they are the endogenous source of blood TG.

4.3 EXPERIMENTAL MEASUREMENTS OF LIPOPROTEINS-LIKE PARTICLES IN BLOOD

To assess the effect of lipoprotein-like particles on the blood optical properties, an ex-vivo experiment was conducted using fresh bovine blood (Carolina Biological Supply) and intralipid (INTRALIPID[®] 20%) as surrogate for TRLs. Intralipid is an intravenous fat emulsion composed of soybean oil, egg yolk phospholipids, glycerin, and water and is used as a source of calories and essential fatty acids for several therapeutic and nutrition indications, such as nutrition supply for patients with essential fatty acid deficiency. Intralipid is available at different lipid concentrations, described by the mass percentage of soybean oil in the volume of emulsion. For instance, intralipid 20% contains 20% of soybean oil (1000 ml of intralipid 20% contains 200 g of soybean oil) which is more than 70% triglyceride [69]. The size distribution of intralipid particles has been previously quantified through electron microscopy, with reported intralipid particle sizes ranging from 25 to 675 nm with an exponentially decreasing size distribution and an average particle size of 97 nm [70]. The refractive index of intralipid micelles is 1.46 which is similar to what the refractive index reported for chylomicron [70, 71]. Due to its particle size range and composition, intralipid closely resembles blood chylomicrons.

SFDI was used to measure the optical properties of blood and the effect of lipids on blood absorption and scattering experimentally. In SFDI sinusoidal patterns of light at different wavelengths and spatial frequencies are projected on the sample and the reemitted light is captured by a camera. The captured images are processed and the result is the maps of optical properties (absorption (μ_a) and reduced scattering coefficient (μ_s')) at every wavelength [71]. We fabricated a dual-LED based NIR-SWIR SFDI system previously [25]. For this study we added a third wavelength in NIR to the system. Our current version of the SFDI system utilizes three LEDs at 730 nm, 880 nm, and 1100 nm

as the illumination source. A digital micromirror device was used to generate the spatial patterns of light. An InGaAs camera (Triwave, Infrared Laboratories, Inc., Peabody, Massachusetts) with a wide range of optical sensitivity was used as the detector. **Figure 4.2** shows the system diagram of the three-LED SFDI system.

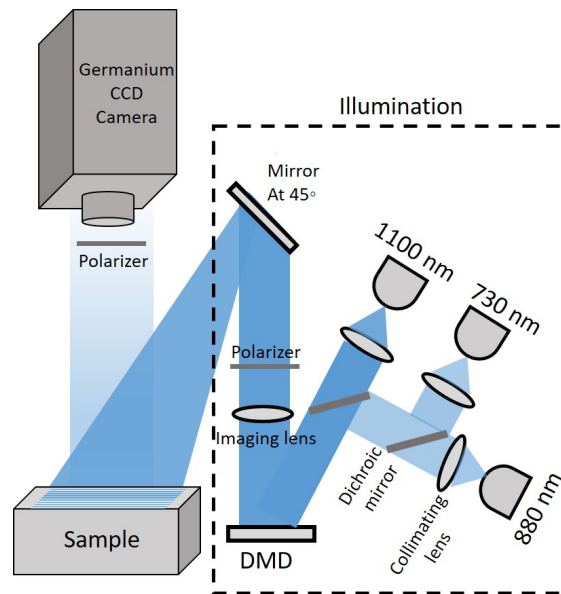


Figure 4.2: System diagram of the three-LED SFDI system.

The concentration of intralipid was titrated in bovine blood from 0.1% to 1% in increments of 0.1%. These intralipid concentrations corresponds to triglyceride levels in blood ranging from a healthy fasting state to a very high state representative of a patient suffering from hypertriglyceridemia, a condition in which lipoproteins are not rapidly absorbed into tissue from the blood [72]. The optical properties of pure blood and blood-intralipid mixture were measured at each intralipid concentration using SFDI. In each case a 12 ml sample was measured in well contained as part of an optically diffuse optical phantom as in our prior work [12].

The results, as shown in **Figure 4.3.A**, indicate that the absorption properties of blood

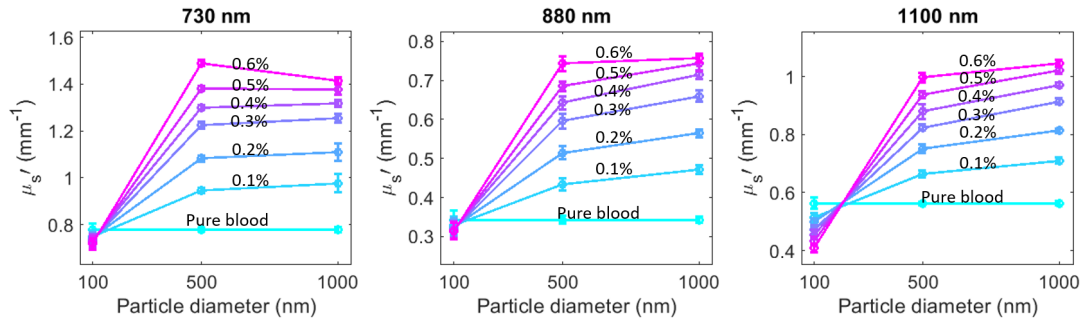


Figure 4.3: Intralipid in bovine blood titration experiment results A) Measured absorption coefficient at three wavelengths showing no appreciable change as intralipid concentration increases from 0.1% to 1%. B) Reduced scattering coefficient increases with intralipid concentration for all measured wavelengths. C) $\Delta\mu_s'$ shows larger increase for shorter NIR wavelengths

are largely unchanged by the addition of intralipid at these concentrations. This observation is supported by estimated changes predicted using Beers law and known extinction coefficients, which predict a less than $1 \times 10^{-4} \text{ mm}^{-1}$ increase in μ_a for a 0.1% increase in lipid concentration at these wavelengths. In contrast, the reduced scattering coefficient of blood increased with increasing intralipid concentration, with larger $\Delta\mu_s'$ observed at shorter NIR wavelengths compared to the longer SWIR wavelengths (**Figure 4.3.B-C**). It should be noted that the μ_s' spectra do not follow the expected power law behavior for the ex-vivo blood measurements due to the predominant effect of large red blood cells on optical scattering, resulting in scattering oscillation at these wavelengths when the measurement wavelength is small compared to the size of the scattering particles.

Since the size of chylomicron particles is also affected by a meal [73, 74], we next investigated the effect of particle size on blood optical scattering through a monodisperse polystyrene microsphere titration experiment. In this study, microsphere beads with three sizes were used: 100 nm, 500 nm, and 1000 nm, mimicking small, medium, and large lipoproteins. We note that the refractive index of microspheres is approximately

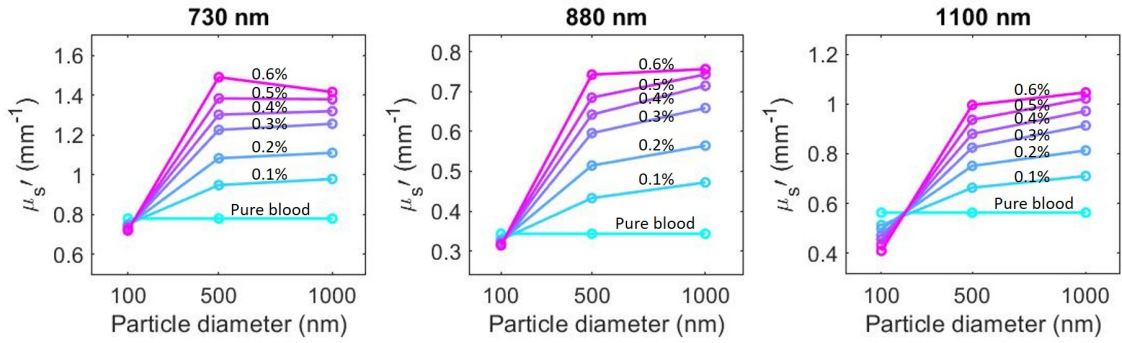


Figure 4.4: Microsphere bead in blood titration experiment at 730, 880 and 1100 nm. The results show the effect of added particle size on blood μ_s' as the bead concentration and size increases. The largest μ_s' increases occur from 100 nm to 500 nm. Bead concentration is indicated as volume percentage of bead in blood.

1.57 at the measured wavelengths which is higher than the refractive index of lipoproteins and intralipid micelles, which range between approximately 1.46 and 1.5 [71, 75]. SFDI measurements were taken from the mixture of microsphere particles in bovine blood with bead concentration (V/V) ranging from 0.1% to 0.6% with 0.1% increments. (Figure 4.4) illustrates the effect of particle concentration and size on the μ_s' of blood, showing that increasing the added particle size leads to an increase in blood μ_s' , with a more pronounced effect when the bead size increases from 100 nm to 500 nm.

4.4 ESTIMATION OF BLOOD μ_s' ALTERATIONS WITH MIE THEORY

Mie theory was used to model the experimental results above. Mie theory describes the scattering of electromagnetic plane wave by homogenous spherical particles. The following equation can be used to approximate the reduced scattering coefficient of particles using the Mie theory framework [76]:

$$\mu_s'(\lambda) = N_0 \sum_i f(a_i) (\pi a_i^2) Q_{scat}(m, a_i, \lambda) [1 - g(m, a_i, \lambda)] \quad (4.1)$$

$$m = \frac{n_1}{n_0} \quad (4.2)$$

Here N_0 refers to the number density of the scattering particles, $f(a_i)$ refers to the particle size distribution, a is the particle radius, Q is the scattering efficiency derived from Mie theory, λ is the wavelength, m is the relative refractive index where n_1 and n_0 are the refractive indices of the particles and the surrounding medium, respectively. The g parameter is the anisotropy factor which can also be predicted with Mie theory.

The use of Mie theory to predict blood optical properties comes with a caveat of dependent scattering caused by RBCs. Dependent scattering events occur in environments where the distance between scattering particles is relatively small compared to the size of the particles [77]. Mie theory is only applicable when the particle spacing is at least 3 to 5 times larger than the particle diameters, a criterion that is not satisfied in blood where RBCs are the dominant source of scattering [78]. However previous studies have applied correction factors to account for the dependent scattering effect of RBCs. One such correction factor is the Twersky factor, which involves multiplying a constant factor dependent on the shape and concentration of the particles to the Mie simulation results [77]:

$$W_m = \frac{(1-h)^{m+1}}{(1+h(m-1))^{m-1}} \quad (4.3)$$

In the Twersky equation for blood, h refers to the blood hematocrit and m is the packing factor that relates to the shape of the red blood cells. In its simplest form, m is defined as an integer value of 1, 2, or 3 for particles that are plate like, cylindrical, or spherical, respectively. Some studies, such as the study on intralipid dependent scattering at high concentrations by Aernouts et al., used non-integer values for m which were empirically determined by fitting the results of the simulations to the experimental results

[79].

Here, Mie theory was used to predict the μ_s' at each lipid concentration in the bovine blood-intralipid titration experiment. The size distribution of intralipid particles reported by Van Staveren et al was used for all Mie simulations [70]. A refractive index of 1.46 was assigned to the intralipid particles and 1.345 to the media [70, 80].

Mie simulations were only conducted for intralipid particles and not the whole blood environment. To correct for dependent scattering, the Mie predicted μ_s' at each intralipid concentration was multiplied by the Twersky factor. The results were then added to the μ_s' of the pure bovine blood measured with SFDI to mimic the intralipid in bovine blood titration experiment at each concentration. The hematocrit level of the bovine blood was measured using an auto blood analyzer (HEMAVET 950FS, Drew Scientific, FL, USA) and found to be 0.33. The packing dimension of the Twersky factor was found empirically by fitting the results of the Mie theory multiplied by the Twersky factor for various concentrations to the measured μ_s' at each measurement wavelength. The packing dimension of 0.97, 1.78, 1.61 was found most effective to match the Mie simulations to the experiment results at 730, 880, and 1100 nm, respectively.

(**Figure 4.5.A**) shows the results of the experiment and the simulations for each of the three wavelengths. The results indicate that the experiment results do not match the Mie simulation before applying the Twersky factor, with the discrepancy between the experiment and the simulation increasing as the lipid concentration increases. (**Figure 4.5.B**) shows the experiment and simulation results after applying the Twersky factor to the output of the Mie equation. These results suggest that Mie theory combined with a dependent scattering correction factor can predict the μ_s' for a given concentration of scattering particles in blood. The mean absolute error (MAE) between the experiment and the simulation results reduced from 0.30 mm^{-1} , 0.32 mm^{-1} , and 0.22 mm^{-1} to 0.027

mm^{-1} , $0.012 mm^{-1}$, and $0.098 mm^{-1}$ after we applied the Twersky factor to the simulated data at 730, 880 and 1100 nm, respectively.

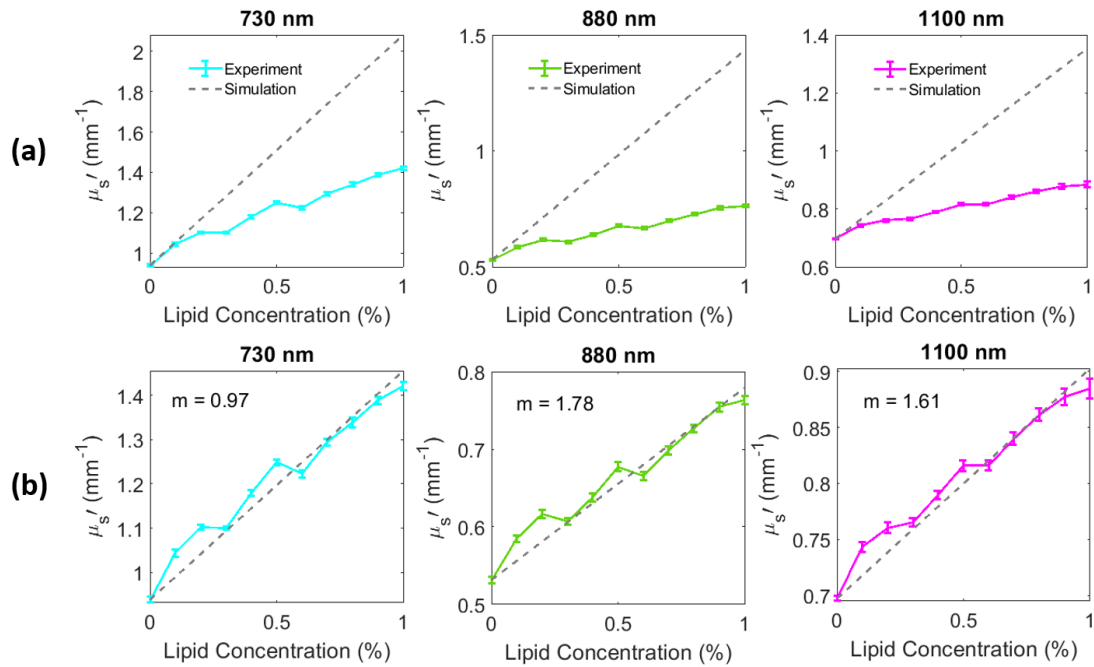


Figure 4.5: A) μ_s' results from titration experiments are shown in solid lines and Mie simulation results from the same lipid concentrations added to the baseline pure blood μ_s' are shown in dashed lines at 730, 880 and 1100 nm. The experiment results do not match the simulations due to the dependent scattering events caused by RBCs. B) Mie predicted μ_s' match the experiment results after correction by Twersky factor to account for dependent scattering events.

The effect of particle size on μ_s' was tested by conducting Mie simulation for monodisperse particles with diameter of 50 to 1000 nm at one selected concentration (0.3% V/V). **Figure 4.6.A** demonstrates the simulated effect of particle size on μ_s' at the three wavelengths. The simulation results supports our observation from the beads-in-bovine-blood titration experiment (**Figure 4.4**), where larger particle size results in an increase in

the measured μ_s' . The effect of size on μ_s' is more significant for smaller particle sizes relative to the wavelength. The simulated μ_s' for particles with similar refractive index as chylomicrons (≈ 1.46 in NIR) shows a similar trend with size but with lower absolute values. We then compared the simulated μ_s' to the measured μ_s' from section 3 at different size, concentration, and wavelengths used in the experiment. **Figure 4.6.B** shows that the simulated μ_s' closely follows the experimental μ_s' measured with SFDI. The intraclass correlation coefficient (ICC(1-1)) shows a strong agreement between the experimental and simulated data (ICC = 0.92, p-value < 0.0001).

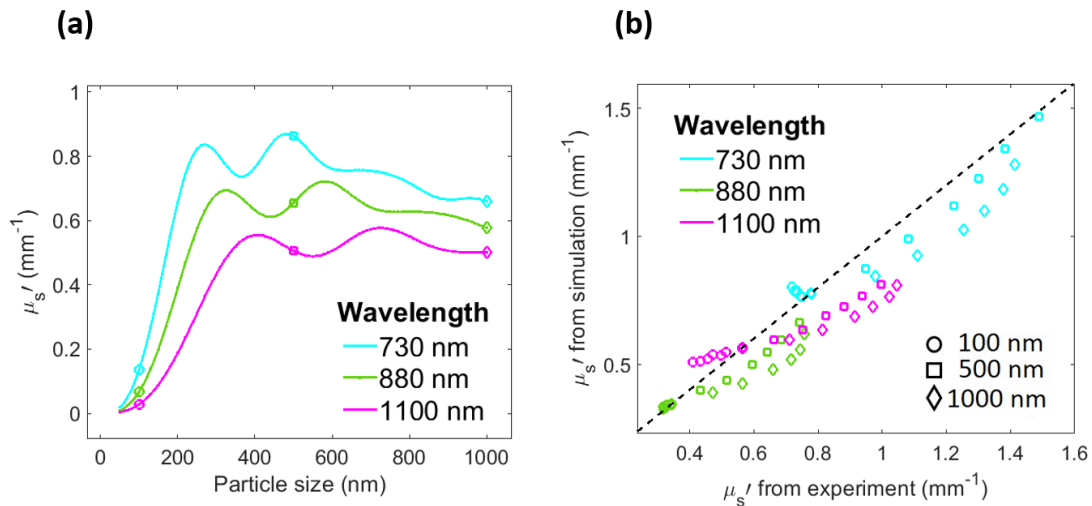


Figure 4.6: A) Mie simulation results shows the effect of particle size on μ_s' at three simulated wavelengths. The markers shows the particle sizes that were used in the bead experiment B) Comparison between the measured μ_s' and the simulated μ_s' at different bead size, concentration and wavelengths. Different colors correspond to different wavelengths and different marker shape correspond to different bead sizes. Each data point corresponds to a different concentration from 0.1% to 0.6% (V/V) of bead in bovine blood. The black dashed line is the identity line.

4.5 CHYLOMICRON AND VLDL SCATTERING PARAMETERS FROM LITERATURE

The sections above provide an initial evaluation of how lipoprotein-like particles affect blood optical properties. In order to gain a better understanding of how human lipoproteins affect optical scattering of blood in the postprandial state, it is necessary to have knowledge of the size, number density, and refractive index of the TRLs in the blood pre- and post-meal. Although prior research has focused on blood triglyceride content when studying blood lipids, less is known about chylomicron concentration and the distribution of chylomicrons and VLDLs. Here, we reviewed the existing literature on the TRLs and used these information to generate a size distribution with accurate particle concentration for these lipoproteins. The information on size and concentration as well as the refractive index of TRLs were then used to predict the impact of TRL alterations on blood optical scattering pre- and post-meal using Mie theory.

Table 4.1 summarizes the reported literature properties for TRLs and blood triglyceride content in the fasting state. The concentration of chylomicron and VLDL particles is directly related to the blood triglyceride level, as most of the blood triglyceride is carried by these particles. If a size distribution is assumed for chylomicron and VLDL particles, the blood triglyceride level can be converted into the concentration of TRL particles of each size. It was assumed that chylomicrons and VLDLs have an exponentially decreasing size distribution [70, 71], with chylomicrons spanning between 75 to 1200 nm and VLDL particles spanning 30-80 nm [67, 68]. An exponential size distribution was generated for each particle with an average size of 100 nm for chylomicrons and 50 nm for VLDLs:

$$f(a_i) = \frac{\exp\left(\frac{a_i}{a}\right)}{a} \quad (4.4)$$

Here $f(a_i)$ is the distribution function with respect to particle size and a is the size parameter related to the average size of the distribution.

To calculate the concentration of the particles, it was first assumed that the blood triglyceride content is distributed between chylomicron and VLDL particles, with 30% of fasting triglyceride coming from chylomicron and 70% from VLDL [81]. Next, chylomicron and VLDL mass concentration was calculated for the corresponding blood triglyceride concentration, assuming that 90% of chylomicrons and 50% of VLDLs mass are triglyceride [68]. The volume concentration of TRLs was then calculated by dividing the mass concentration of the particles by their volume density. The volume density of chylomicrons and VLDLs are approximately 930 mg/ml and 1000 mg/ml, respectively [68]. Using the generated size distribution for these two particles, we then calculated the total number of each particle at each size by dividing the volume concentration of chylomicrons and VLDLs by the total volume of these particles from the normalized size distribution:

$$N = \frac{P}{\sum f(a_i)V(a_i)} \quad (4.5)$$

where N refers to the total number of particles (CM or VLDL), P is the total volume of the particles, f is the normalized size distribution, V is the volume of the particles with size a_i , and i is the number of particles in the size distribution.

We then generated a distribution of chylomicron and VLDL particles for any concentration of fasting triglyceride in blood by multiplying the total number of each particle by the normalized size distribution $f(a_i)$. (**Figure 4.7**) shows this distribution of VLDLs and chylomicrons for blood triglyceride level of 100 mg/dL.

Table 4.1: Reported literature properties for TRLs and triglyceride in the fasting state as well as model parameters

Property	Reported values	Reference Notes	Model parameters
Particle diameter	Chylomicron: 75-1200 nm, VLDL: 30-80 nm	[67, 68]	Chylomicron average size = 100 nm, VLDL average size = 50 nm
Particle size distribution	Exponential	[70, 71]	Assume chylomicrons have the same size distribution shape to intralipid Exponential
Density (g/ml)	Chylomicron < 0.95, VLDL: 0.96-1.006	[67, 68]	Chylomicron: 0.93, VLDL: 1
Triglyceride content (%W/w)	Chylomicron: 80-95%, VLDL: 45-65%	[68]	Chylomicron: 90%, VLDL: 50%
Refractive index	Chylomicron: 1.46%	[71]	No information on VLDL is available 1.46 for both VLDL and chylomicron
Plasma fasting triglyceride (mg/dL)	Normal: <150 mg/dL, Borderline high: 150-199 mg/dL, High: 200-499 mg/dL, very high: >500 mg/dL	[82]	Healthy: 50 mg/dL, Diabetes: 200 mg/dL, Hypertriglyceridemia: 200 mg/dL

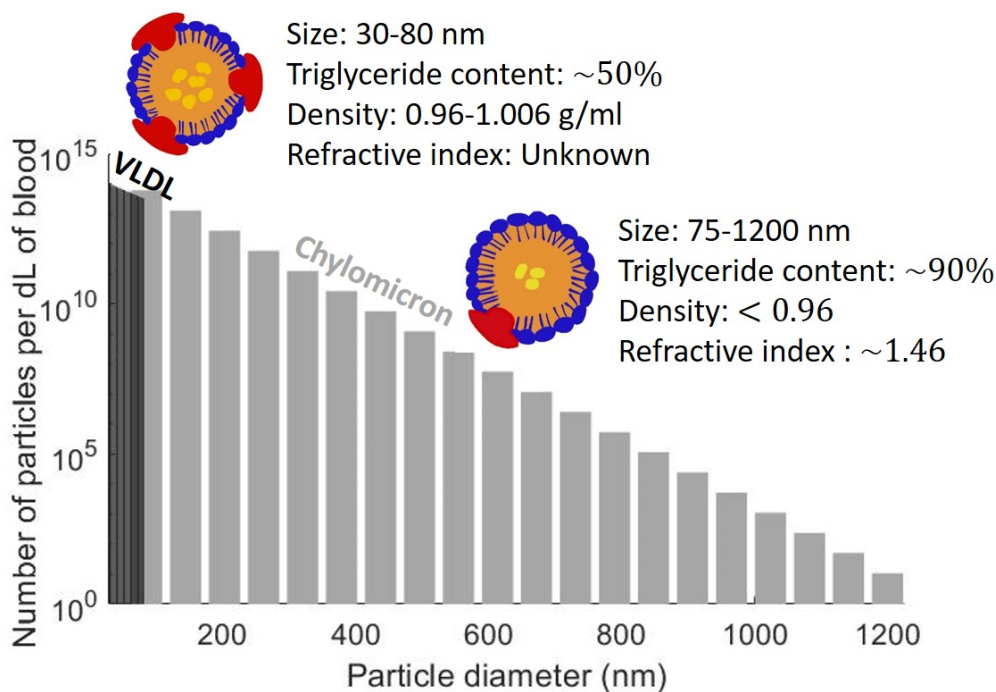


Figure 4.7: VLDL and chylomicron size distribution for 100 mg/dL of blood triglyceride

Table 4.2 summarizes the changes in triglyceride content and TRL properties that

may occur after a meal based on literature. An increase in blood triglyceride levels primarily results in changes in chylomicron distribution, resulting in larger average particle size, higher refractive index, and higher number density [71, 73, 74].

Table 4.2: Reported literature properties for TRLs and triglyceride in the postprandial state

Property	Reported values	Reference	Notes	Model parameters
Blood triglyceride	Healthy: < 175 mg/dL, High: 175-880 mg/dL, Hypertriglyceridemia: >880 mg/dL	[8]		Healthy: 100 mg/dL, Diabetics: 400 mg/dL, Hypertriglyceridemia: 1200 mg/dL
Peak refractive index	Chylomicron: 1.5, VLDL: -	[71]	No information on RI of VLDL is available	CM : 1.5, VLDL : 1.46 (no change)
Peak average size	Chylomicron: 200 nm, VLDL: 60 nm	[74, 73]	Effect of meal on VLDL particle size is minimal	Chylomicron: 200 nm, VLDL: 50 nm (no change)

A triglyceride level of <150 mg/dL is considered to be normal in the fasting state [82]. For a healthy individual, the triglyceride levels in the blood increases and reaches its peak 2-4 hours after a meal. Triglyceride content can rise up to 175 mg/dL, depending on the meal and the persons response to the fat intake [83]. However, for individuals with type 2 diabetes or hypertriglyceridemia, both the baseline and postprandial triglyceride levels can be much higher. A baseline triglyceride level of 200 mg/dL is considered high, and levels above 500 mg/dL are considered very high. In the postprandial state, triglyceride levels may reach as high as 1000 mg/dL or more for subjects with such conditions [83].

In addition to concentration, the size of the chylomicrons also increases after a meal. One study showed that the size increase ranges from 90-120 nm, with younger subjects showing larger increases compared to older subjects [74]. Additionally, the size of the smaller TRLs, VLDLs, increase by about 10 nm after a meal [73]. The increase in particle size is related to the amount of triglycerides carried by the particles, with larger particles carrying more triglycerides.

The refractive index of the TRLs has also been shown to change with alterations in their size and composition. Particles with higher triglycerides content have higher refractive index compared to the particles with lower triglyceride content. The mean refractive index of chylomicrons in the fasting state is reported to be 1.46, and increases to around 1.5 after a meal [71]. However, there is limited information on the refractive index of VLDLs and how it changes after a meal in the prior literature.

4.6 ESTIMATION OF BLOOD μ_s' CHANGES AFTER A MEAL

Having the above information on TRL size distribution, concentration, and refractive index allows for the estimation of expected blood μ_s' during fasting and after a high fat meal. We first simulated the whole blood environment by assuming a single particle size for RBCs. The non-spherical shapes of RBCs does not satisfy the spherical particle assumption in Mie theory, however, previous studies have attempted to overcome this limitation by assuming a spherical shape for RBCs with a diameter that corresponds to their equivalent volume [84]. For these simulations a diameter of 5.56 μm and a number density of 0.005 $\text{cell}/\mu\text{m}^3$ (correspond to 0.45 hematocrit) was assumed for RBCs [85]. The refractive index for RBCs was assumed to be 1.4 [85]. Using the distribution of chylomicrons, VLDLs, and RBCs, the effect of postprandial lipid alterations on blood scattering properties was estimated using Mie theory combined with the Twersky correction factor for dependent scattering. To calculate the Twersky factor, the packing factors determined in section 4 were used.

Figure **Figure 4.8.B**, **Figure 4.8.C** and **Figure 4.8.D** illustrate the effect of increasing blood triglyceride content on the scattering coefficient (μ_s), anisotropy factor (g), and μ_s' of blood. The first simulation represents 50 mg/dL of blood TG with an average chylomicron

size of 100 nm, and the following 10 simulations show a 50 mg/dL increase in blood TG and a 5 nm increase in average chylomicron size at each step. The refractive index of chylomicronparticles increases from 1.46 to 1.5 from the first to the last simulation. The simulation parameters are shown in **Figure 4.8.A**. These simulations suggest that while blood μ_s is not significantly affected by the altered triglyceride content, blood μ_s' increases with an increase in blood triglyceride concentration. This increase in blood μ_s' is mainly due to the larger scattering angle events as a result of altered TRLs, and hence smaller g parameter compared to the fasting state. **Figure 4.8.E** summarizes the percent change in μ_s' for different triglyceride alteration from the baseline simulation.

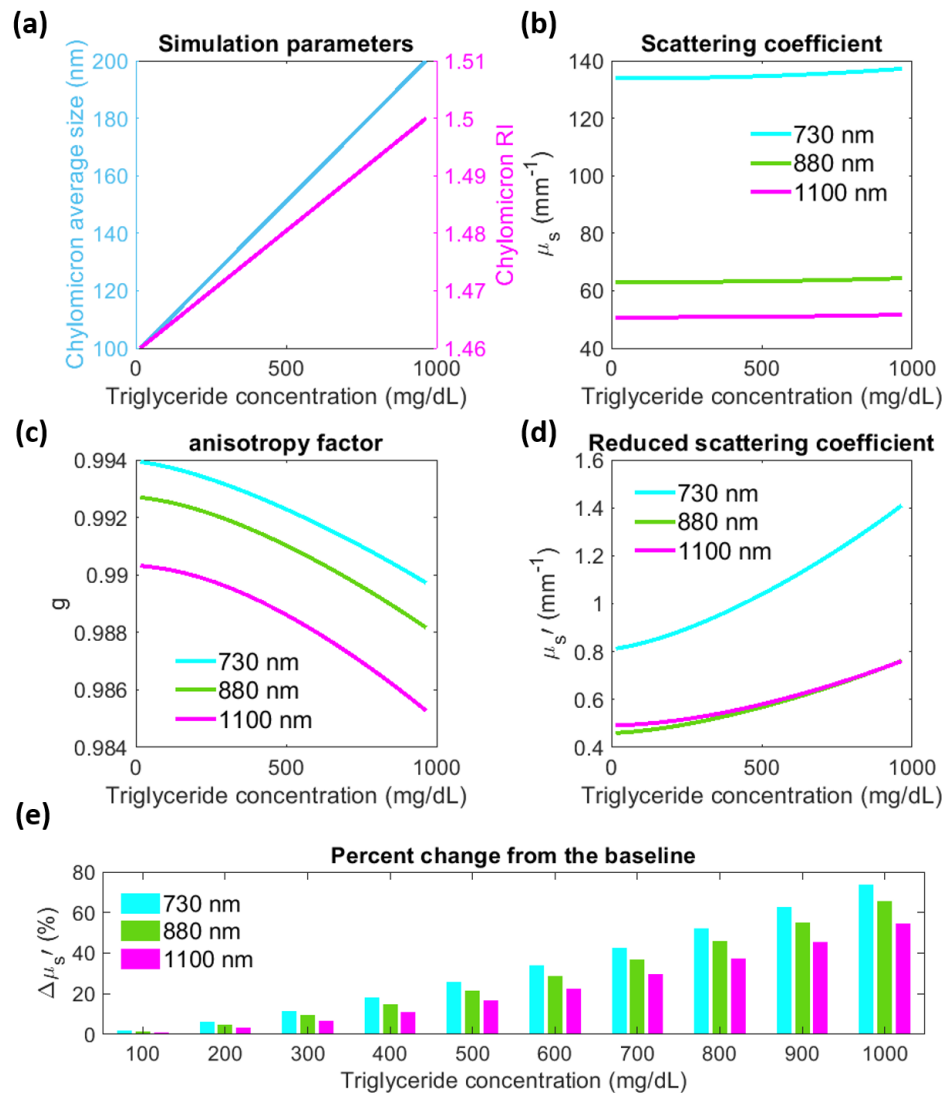


Figure 4.8: Mie simulation results for whole blood in fasting and postprandial state. A) Simulation parameters B) Blood scattering coefficient (μ_s) B) anisotropy factor and C) blood μ_s' as the triglyceride content in blood increases. The increase in triglyceride results in higher concentration of chylomicrons, larger chylomicron particles and higher refractive index. D) Percent change in blood μ_s' from the baseline (first simulation results)

The effect of lipid alteration on blood μ_s' was further simulated by adding the simulated chylomicron and VLDL changes to the experimental measurements of blood μ_s' .

For a healthy subject, we assumed 50 mg/dL of blood triglyceride in the fasting state, which increased by 50 mg/dL after a meal. For subjects with type 2 diabetes and hypertriglyceridemia, the baseline blood triglyceride level was assumed to be 200 mg/dL, which increased by 200 mg/dL and 1000 mg/dL after a meal, respectively. For all subjects, we assumed an average chylomicron size of 100 and refractive index of 1.46 at the fasting state, which increased to 200 nm and 1.5 after a meal.

Table 3 shows the estimated postprandial $\Delta\mu_s'$ for healthy subjects, and subjects with type 2 diabetes, and hypertriglyceridemia. Similar to the $\Delta\mu_s'$ from the whole blood simulation results shown in **Figure 4.8.D**, these simulations also suggest a few percent increase in μ_s' for healthy subjects after a meal, and up to a 64% increase in μ_s' for subject with hypertriglyceridemia.

Table 4.3: $\Delta\mu_s'$ from the baseline for different level of TG correspond to different subject population. The Mie simulated μ_s' was added to measured bovine blood μ_s' at each wavelength

Subject	Δ Triglyceride	$\Delta\mu_s'$ (730 nm)	$\Delta\mu_s'$ (880 nm)	$\Delta\mu_s'$ (1100 nm)
Healthy	50 mg/dL	3.85%	3.34%	2.32%
Type 2 diabetes	200 mg/dL	15.23%	13/25%	9.26%
Hypertriglyceridemia	1000 mg/dL	64.37%	55.79%	38.57%

4.7 DISCUSSION

In this work, we investigated the effect of lipoprotein particles on the optical properties of blood. Specifically, we studied chylomicrons and VLDLs, which are the two largest lipoproteins in blood and are highly optically scattering. We used SFDI

to experimentally measure the effects of lipoprotein-like particles on the μ_s' of blood. Our titration experiment of intralipid in bovine blood showed an increase in μ_s' with an increase in intralipid concentration, with larger changes at shorter, NIR wavelengths. The microsphere-in-bovine-blood titration experiment showed an increase in blood μ_s' with an increase in particle size, with larger changes for increases in smaller sized beads. The results were then simulated and validated using Mie theory and a correction factor for dependent scattering. Next, we generated a distribution for chylomicrons and VLDLs based on prior literature information on their size, refractive index, composition and concentration. Using this size distribution, we estimated the effects of blood lipid after a meal for different levels of triglyceride alteration, corresponding to healthy, diabetic, and hypertriglyceridemic blood triglyceride content. Our simulations indicate a small increase in blood μ_s' (a few percent) in healthy subjects and changes as high as 60% for subjects with hypertriglyceridemia after a meal.

Measurements of blood lipids have implication for cardiovascular disease assessment. Hyperlipidemia, which refers to the abnormal elevation of blood lipids including cholesterol and triglyceride, is one of the major risk factors for CVD and can indicate an increased risk of heart attack, myocardial infraction, and stroke [8]. Regular screening of blood lipids is essential for early CVD diagnosis, surveillance, and treatment feedback [19, 20]. Current blood lipid measurements require invasive blood draws, usually after an overnight fast. Recent evidence suggest that postprandial measurement of blood lipids may further improve CVD risk prediction and help to identify pre-diabetic conditions [9, 22]. Beside the invasive nature of the current technique, blood draws and the following lab-based analysis are resource intensive due to the need of trained technicians and lab equipment. These requirements limit access to blood lipid measurements and prevent those at risk of CVD from undergoing regular blood lipid monitoring [86, 87].

Measuring the optical properties of blood and their changes over time could offer a potential alternative for assessing blood lipid levels, making regular blood lipid testing more practical and accessible. SFDI has the capability to non-invasively measure blood optical properties through intact skin when combined with multilayer inverse models [28]. The effect of lipoproteins on optical scattering of blood can potentially provide information about the concentration of the lipoproteins and their response to meals. Additionally, the spectral shape of the scattering coefficient can potentially shed light on lipoprotein sizes and how they change after a meal through Mie analyses [88]. There may be other invasive and non-invasive techniques that can be used to take advantage of the optical scattering changes identified in this work. While longer NIR and SWIR wavelengths are ideal for in vivo measurements due to tissue penetration, shorter wavelengths than those used in this work may be ideal for ex-vivo measurements of blood due to the larger expected changes in scattering.

One potential confounder for the use of optical scattering measurements for blood lipoproteins is the impact of hematocrit on blood optical properties. Subjects with different hematocrit levels will have different absorption and scattering properties regardless of their blood lipid status. However, assuming that hematocrit remains constant for a subject after a meal, optical measurements of blood can still be used to monitor blood lipid dynamics for each individual. This may require a more advanced modeling to isolate the effect of lipoprotein from other confounding physiological factors, which will be investigated in future studies. Furthermore, the alteration in blood μ_s' expected for healthy subjects (a few percent) may be difficult to detect, especially in the in vivo state. We also note that our μ_s' estimation for different blood triglyceride level could be affected by the simulation parameters and assumptions made here, especially since the literature values for some of these parameters were limited.

4.8 CONCLUSION

In summary, our study investigated the effect of lipoproteins and their alterations on blood optical properties through ex-vivo experiments conducted with SFDI and computational modeling using Mie theory. Our findings suggest that lipoproteins are highly optically scattering. Using Mie theory, we were able to estimate the changes in the μ_s' of blood following a high fat meal for individuals with varying medical conditions. The results of this study provide a basis for future investigation of invasive and non-invasive measurements of blood lipoproteins, which may enhance the early detection and management of cardiovascular diseases.

CHAPTER 5

Non-invasive assessment of blood lipid using spatial frequency domain imaging (SFDI): healthy volunteer study

The consumption of a high fat meal has been shown to elicit various hemodynamic changes, including a decrease in endothelial function and alterations in core and peripheral blood flow. To date however, the vast majority of prior studies have utilized ultrasound to characterize the postprandial (i.e. after meal) state through flow-mediated dilation studies. There has been little to no characterization of tissue postprandial hemodynamics using near infrared techniques that can quantify tissue level changes in oxygenation. In this study we used the near-infrared technique called Spatial Frequency Domain Imaging (SFDI) to monitor tissue optical properties and hemodynamics during the postprandial state in a cohort of 20 healthy volunteers. Specifically, we examined the effects of low-fat (2g of fat) and high-fat (60 g of fat) meals on optical properties measured with SFDI, and their correlation with blood triglyceride levels. Additionally, we assessed the reactive hyperemic response following arterial occlusion. Our results demonstrated a strong positive correlation between the change in the tissue absorption coefficient (μ_a), oxyhemoglobin concentration (HbO_2), and tissue oxygen saturation (StO_2) and the change in blood triglyceride levels three hours after a meal (strongest Pearson correlation coefficient = 0.72, P-value = 0.0006). These changes exhibited a statistically significant difference three hours after the meal between the low-fat and high-fat meal groups, indicating the potential impact of dietary fat content on optical measurements. Furthermore, the arterial occlusion study revealed an impaired reactive hyperemic response in subjects who consumed high-fat meals compared to subjects who consumed low-fat meals. These results lay the groundwork for future investigations into the assessment of optical property and hemodynamic changes following meals. The potential applications of this research extend to cardiovascular disease risk assessment

and diet management, offering valuable insights for individuals seeking to optimize their dietary choices and manage cardiovascular health.

5.1 INTRODUCTION

Blood lipids, including cholesterol and triglycerides (TG), are one of the most well-established biomarkers for cardiovascular diseases (CVD) [8, 16, 17]. Elevated levels of lipoproteins, which are micelles that transport lipids through the blood, are strongly implicated in increased risk of developing CVD and can be used to predict CVD and monitor treatment [8, 16, 17]. Regular blood lipid screening is recommended for CVD risk assessment and may improve the diagnostic accuracy of blood lipids [9, 19, 20].

In clinical settings, blood lipids are typically assessed in the fasting state. However, research studies indicate that non-fasting or postprandial TG levels may be a more reliable predictor of cardiovascular risk compared to blood TG levels in the fasting state [17]. Previous studies have shown that hourly postprandial blood lipid monitoring can aid in detecting pre-diabetic conditions and assist in monitoring diet [22, 23]. The current method for assessing blood lipids is through a lipid panel test that requires a blood draw. Measuring blood lipids in the postprandial state in this manner is burdensome and not feasible for standard clinical use due to the invasive nature of the technique, the medical infrastructure required, the personnel and logistics required, and the costs involved in obtaining and analyzing results. Additionally, the latency between the blood draw and the availability of the results is a barrier to point-of-care treatments [87, 86]. The development of a non-invasive method that could reveal postprandial changes associated with blood lipids would make these measurement more practical and increase access to improved screening for at-risk patients.

We recently investigated the use of shortwave infrared spatial frequency domain

imaging (SWIR SFDI) for blood lipid assessment in the postprandial state [12]. The wide-field nature of SFDI enables the segmentation of large superficial vessels from microvascular regions in the measurement location, making the technique valuable for assessing optical changes in the postprandial state non-invasively over both vascular and microvascular regions. In **Chapter 4** we modeled and validated that lipids induce substantial increase in the optical scattering of blood due to changes in size, concentration and refractive index of lipoprotein particles specially chylomicrons after a meal. Additionally these lipoproteins may cause endothelial dysfunction and induce hemodynamic changes in peripheral tissue, changes such as vasoconstriction and reduction in reactive hyperemia [89, 90]. Here we conducted a healthy volunteer study to investigate optical property and hemodynamic changes of superficial vascular and microvascular regions on subjects' hand after a meal.

5.2 MATERIALS AND METHODS

5.2.1 Subjects eligibility and enrollment

The study was conducted in compliance with an institutionally approved review board protocol (protocol number 4698) at Boston University. Informed consent was obtained from all participants prior to the experiment. 20 healthy subjects were recruited among which 10 subjects (5 males and 5 females, age distribution 30.9 ± 6.7) participated in the postprandial study after a low-fat meal and 10 subjects (6 males and 4 females, age distribution 30.4 ± 5.8) participated in the study after a high-fat meal. Subjects that are <18 years old or have a prior history of hypotension (low blood pressure), low blood sugar, dizziness, fainting, and type 1 or 2 diabetes were excluded from the study. Participants were asked to fill a questionnaire containing age, weight, height, race and ethnicity, and

skin tone information prior the start of the study.

5.2.2 Spatial frequency domain imaging (SFDI) system

In this study, a custom built LED based SFDI system was used to perform all the SFDI measurements [28]. The system utilizes two LEDs in the NIR (730 nm and 880 nm) and one LED in the SWIR wavelength band (1100 nm) as the illumination source. Sinusoidal spatial patterns of light were projected on a sample using a digital micro-mirror device (DMD), and the remitted light was captured by a camera. **Figure 5.1.a** shows the system diagram of the three LED SFDI system. A flowchart of SFDI data acquisition and processing is provided in **Figure 5.1.b**. The field of view (FOV) of the SFDI images is 7×11 cm. The exposure time for all three wavelengths was set to 100.925 ms, which is a sufficient time for DMD projection and provide good signal to noise ratio for all measurement wavelengths.

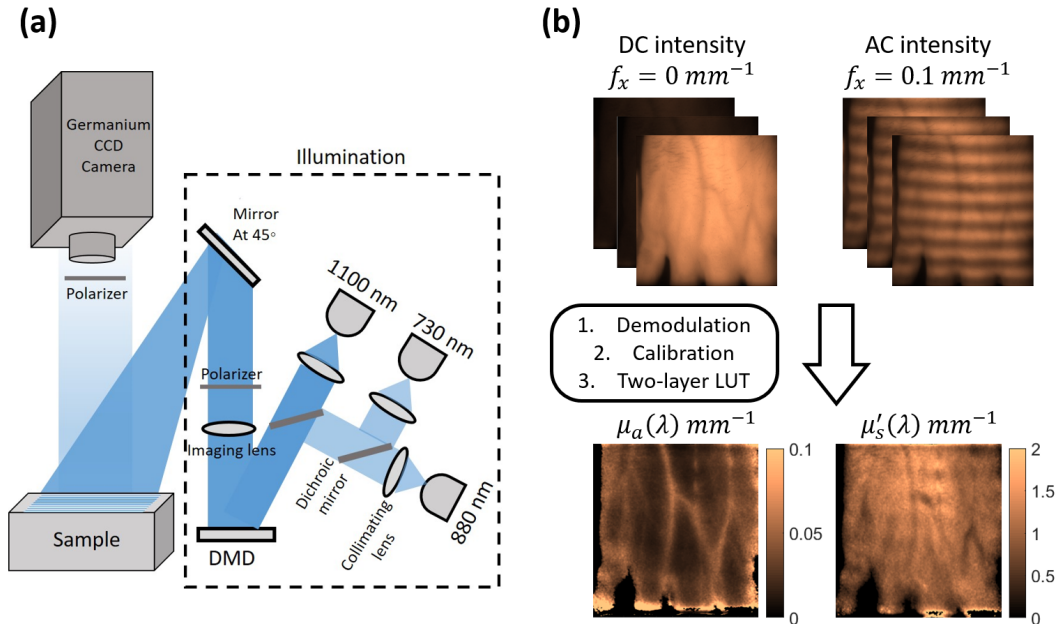


Figure 5.1: a. Schematic diagram of three-LED SFDI system b. SFDI data acquisition and processing flowchart. Top row shows the raw images captured at spatial frequency of DC and 0.1 mm^{-1} from dorsal surface of a subject's hand at 880 nm. The captured images are demodulated and calibrated and the diffuse reflectance data is converted into absorption and reduced scattering coefficient using the two-layer look up tables (LUTs) introduced in **Chapter 3**. The bottom row shows the μ_a and μ'_s maps. The images were cropped to only show the hand ROI.

5.2.3 Postprandial experiment procedure

To assessing the dynamic of postprandial lipoproteins in response to a test meal, voluntary subjects who agree to participate in the study were asked to do 10 hours of overnight fasting. Subjects who were participated in the high fat meal study were provided a meal in the next morning that contained $\sim 60 \text{ g}$ of fat ($\sim 1400 \text{ KCal}$). Subjects had an option to choose between breakfast sandwiches from Dunkin Donuts (Bacon egg and cheese or sausage egg and cheese on croissant) or big breakfast option from McDonald's combined with two protein shakes. Subjects in the low fat meal group were provided a zero-sugar oat-

meal (2 g of fat, 110 KCal) in the morning of the study. Subjects were monitored following the measurements procedure at the baseline (before consuming the meal in the morning) and for 5 hours every hour after the meal.

5.2.4 Measurement procedure

Figure 5.2 shows the study procedure and timeline. Prior to the start of the procedure, subjects were offered a cup of water and their blood pressure was measured to check for exclusion criteria (i.e. low blood pressure). The study procedure contained three components: hourly SFDI measurements, planar illumination measurements during hourly arterial cuff occlusions, and hourly blood tests.

Participants were instructed to sit on a chair and place their right hand into a silicone hand holder positioned under the SFDI system. An automated pneumatic cuff was placed around their right arm. SFDI measurements were conducted on the dorsal surface of the participants' hand while they were asked to keep their hand still in the holder through the entire study. SFDI patterns were projected at spatial frequency pair of DC and 0.1 mm^{-1} at three wavelengths of 730 nm, 880 nm and 1100 nm. After all SFDI patterns were projected, a single DC pattern at 880 nm was projected onto the participant's hand and images were captured at a rate of 0.3 frames per second. Following a 1-minute baseline measurement, the occlusion procedure began with a pressure of 215 mmHg applied to subjects' upper arm, which is appropriate for both venous and arterial occlusions. This pressure was maintained for 3 minutes before being released. Measurements continued for an additional 4 minutes after the release of pressure to capture the recovery state. Participants were then asked to sit on a different chair for blood work. The glucose and lipid profile were assessed using an in-lab lipid analyzer (Alere Cholestech LDX Analyzer). A fingerstick procedure was performed on the participant's finger to collect

several small drops of blood using a lancet within 10 seconds. The blood sample was then placed in a cassette and inserted into the Alere system to obtain the full blood profile and glucose concentration.

After finishing the procedure in the fasting state, the subject were asked to eat a low-fat (control group) or a high-fat meal (known to induce increased blood lipids). The procedure were then repeated for 5 hours every one hour after the meal. Additionally, blood pressure and heart rate was measured at every time point. Subjects were free to leave the lab between measurements. Participants were told not to eat for the duration of the study but they were allowed to drink water.

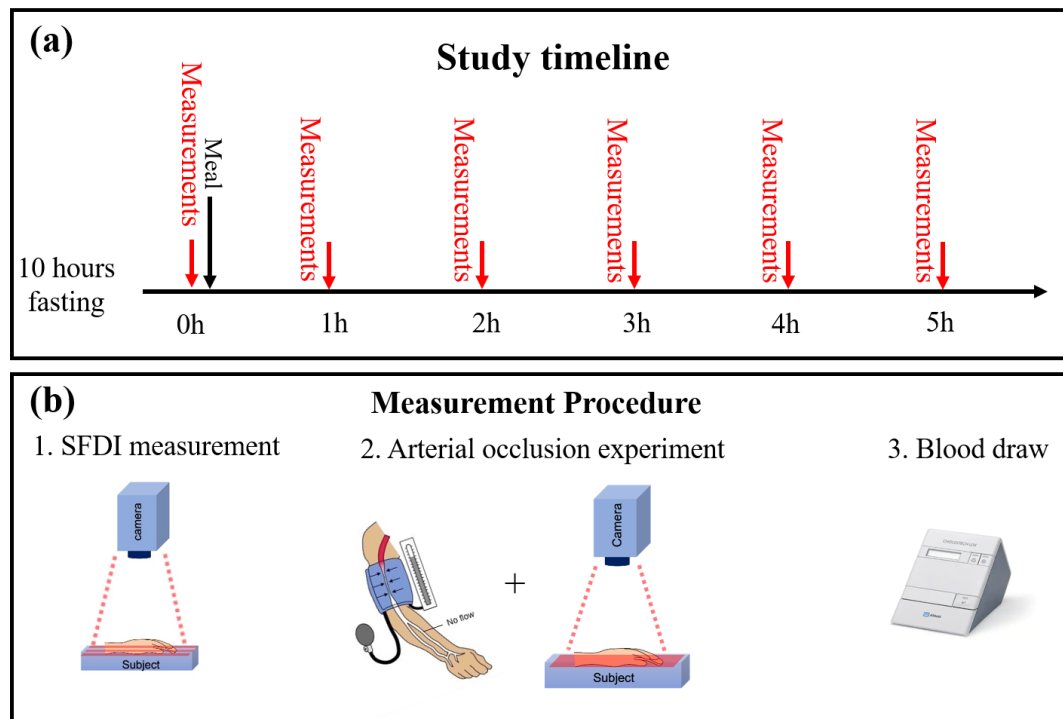


Figure 5.2: a. Study timeline b. Measurement procedure

5.2.5 Data analysis

5.2.5.1 SFDI data analysis

Details regarding SFDI data processing has been described elsewhere [10]. Briefly, the captured images at different spatial frequencies are demodulated using the demodulated algorithm. The demodulated images are calibrated using a calibration phantom with known optical properties. Optical absorption and reduced scattering coefficients were then estimated at each illumination wavelength from a two-layer lookup table generated by Monte Carlo simulations with calibrated diffuse reflectance map at two spatial frequencies as inputs. The two layer LUTs were generated in our prior work to account for the effect of human skin [28]. Spatial frequency pair of DC and 0.1 mm^{-1} were used for all SFDI measurements in this study. Additionally, the extracted μ_a values at 730 nm and 880 nm were used to extract hemoglobin information, including the concentration of oxyhemoglobin (HbO_2), deoxyhemoglobin (Hb), total hemoglobin (THb), and hemoglobin oxygen saturation (StO_2). The absorption map at 880 nm for each subject was used for vessel segmentation at each time point. Automated identification of vessels across the entire hand region was achieved by utilizing Hessian-based multiscale filtering, implemented through the "fibermetric" command in MATLAB. To identify superficial veins, pixels that corresponded to the top 60% of μ_a within segmented vessel areas were used. The generated vessel mask was applied to optical property and hemoglobin maps for segmenting vascular and microvascular regions. The average μ_a and μ_s' as well as oxyhemoglobin, deoxyhemoglobin, total hemoglobin and hemoglobin oxygen saturation (StO_2) were calculated for areas inside vascular regions and the rest of the image (microvascular regions) at each time point.

In addition to the absolute optical property and hemoglobin values, composite metrics of optical properties were calculated and contrast analysis was also conducted for more

thorough comparison of SFDI metrics at different time points. The contrast between vascular and microvascular regions was calculated using equation 1 (Weber contrast):

$$Contrast = \frac{(\mu_{MAX} - \mu_{MIN})}{\mu_{MIN}} \quad (5.1)$$

In this equation, μ refers to either μ_a or μ_s' at each measurement wavelengths. In line profile assessment for each subject, three large superficial vessels were selected and the contrast between vascular and microvascular region over the three line profile were averaged and used as the vascular-microvascular contrast metric. Alternatively, this metric was also calculated using the average optical properties over vascular and microvascular regions after vessel segmentation.

All SFDI features were normalized to the value at the baseline to compare the relative changes over time as well as comparing the two subject categories (low fat versus high fat). All data were processed using MATLAB (R2021b, The Mathworks Inc., Natick, MA).

5.2.5.2 *Planar illumination analysis for the arterial occlusion experiment*

In order to extract absorption information from a single DC illumination, we utilized the μ_s' value that was measured with SFDI prior to the cuff occlusion experiment at each time point, and assumed that it remained constant throughout the occlusion experiment. μ_a at 880 nm was then extracted from the approximately 1600 images that were taken during the 8 minute occlusion experiment at each time point.

The longitudinal absorption trend at each time point was plotted as a function of time for a selected vascular and microvascular region. Parameters such as the release point, maximum μ_a after the release and recovery point (time point where μ_a returns to a stable value) were identified manually. The metrics such as time to peak after the release,

$\Delta\mu_a$ from the release to maximum μ_a , recovery slope, reperfusion slope and area under the curve were then calculated using these parameters. For AUC, μ_a was normalized and adjusted to zero in the released point and the AUC was calculated from the release up to 30 seconds after the release.

5.2.5.3 Statistical analysis

Descriptive data are presented as *mean* \pm *SE*. Statistical analysis was conducted using the "anovan" function in MATLAB to compare the SFDI-derived parameters between two groups (high fat meal and low fat meal) over six time points. The analysis examined the interaction effect between the group and time factors. Post hoc analysis was performed using the "multcompare" function to determine pairwise differences between the groups at each time point. A p-value < 0.05 was considered statistically significant.

5.3 RESULTS

5.3.1 Lipid panel

The effect of high fat and low fat meal on blood triglyceride, glucose and cholesterol is shown in **Figure 5.3**. All results are shown as percent change from the baseline. There was a significant increase in blood triglyceride 2, 3, 4 and 5 hours after the meal ($p < 0.0001$ for 2-4 hours and $p < 0.01$ for the 5th hour). No significant change in triglyceride occurred after the low fat meal. For the high meal subject category, on average triglyceride concentration reaches its peak value 3 hours after the meal consumption. For the low fat meal subject category, most subjects show either a decrease or minimal increase in triglyceride concentration after the meal. For both subject groups, glucose increase 1 hour after the meal with significant change only in high fat meal group ($p < 0.05$) and declined

in the following hours. No significant change occurred in blood cholesterol following a meal.

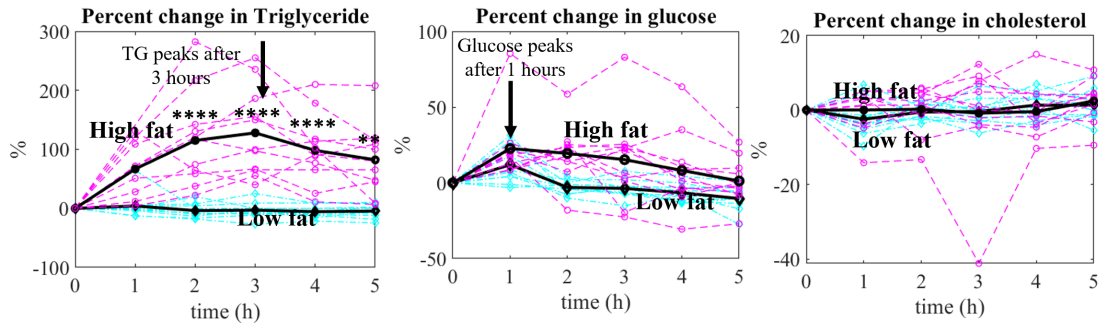


Figure 5.3: Percent change in a) triglyceride concentration b) glucose concentration and c) cholesterol concentration compared to the fasting state (time point = 0) during the 5 hours postprandial measurements after high fat and low fat meal. Asterisks show the level of significant different between the two subject groups. $p < 0.00001$ is shown with **** and $p < 0.05$ is shown with *.

5.3.2 SFDI results

The temporal changes and trends in SFDI-derived parameters over the six-hour experiment were investigated. This analysis aims to provide insights into the dynamic patterns of SFDI-derived parameters and their association with different meal types over time. The difference between the two subject groups were analyzed over both vascular and microvascular regions. **Figure 5.4** shows the oxyhemoglobin map of a representative subject from each category at baseline and three hours post-meal. The maps indicate an increase in oxyhemoglobin levels in the vascular and microvascular regions of the subject who consumed a high-fat meal. For this subject, the average oxyhemoglobin concentration of vascular and microvascular regions increased from $54 \mu\text{M}$ and $31.8 \mu\text{M}$ at baseline to $87.4 \mu\text{M}$ and $53.3 \mu\text{M}$ 3 hours after the high fat meal. Conversely, the subject who consumed a low-fat meal exhibited a decline in oxyhemoglobin levels, indicating an

opposite trend. The average oxyhemoglobin concentration of vascular and microvascular regions changed from 70.2 μM and 45.2 μM at baseline to 69.2 μM and 48.22 μM 3 hours after the low fat meal.

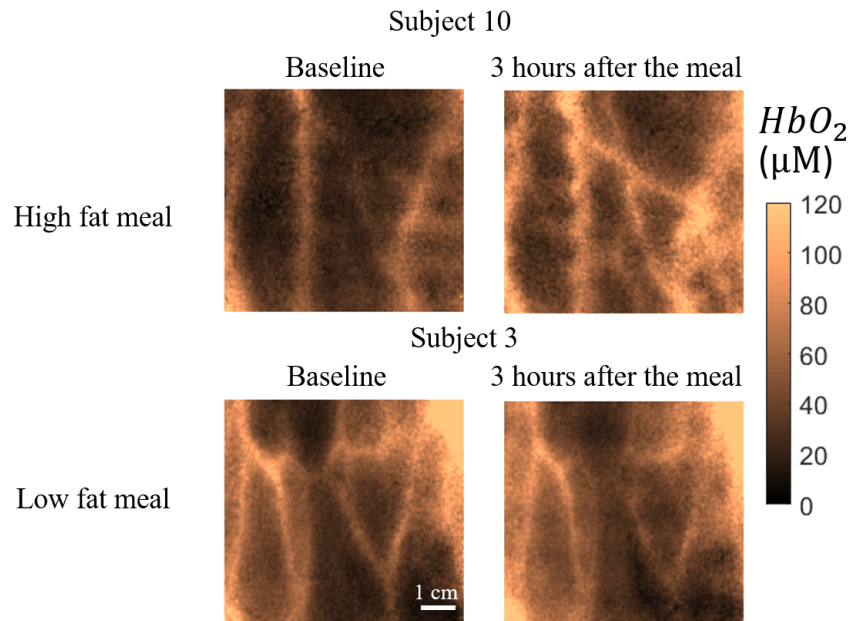


Figure 5.4: Oxyhemoglobin maps at baseline and three hours after the meal for representative subjects in high fat and low fat category.

For more quantitative analysis of changes in SFDI parameter after the meal, hand ROIs was segmented into vascular and microvascular regions. **Figure 5.5.a** shows the process of generating a vessel mask using the μ_a map at 880 nm, and apply the mask to optical property and hemoglobin maps for a representative subject. A separate mask was generated at each time point. The mean and standard deviation of the SFDI parameter inside each region were calculated to use in the comparison and correlation analysis.

The composite metric of $\mu_a \left(\frac{\mu_a(1100\text{nm}) \cdot \mu_a(880\text{nm})}{\mu_a(730\text{nm})} \right)$ in the microvascular regions shows the strongest correlation with triglyceride levels (pearson correlation coefficient = 0.73, P-

value = 0.0006). Following that, Oxyhemoglobin in the microvasculature and Weber contrast in μ_a at 880 nm exhibit strong correlations with triglyceride levels when normalized to the baseline. **Figure 5.5.b** shows the longitudinal relative changes of these three metrics with the highest correlation with triglyceride for high fat and low fat study groups. For subjects who consumed a high fat meal, these metrics increase and peak three hours after the meal. The peak occur at the same time point as the triglyceride peak. Conversely, subjects who had a low fat meal show an opposite trend, particularly within the first two hours after the meal. There is a statistically significance difference between high fat and low fat meal subjects three hours after the meal at these three metrics. **Figure 5.5.c** illustrate the correlation between the same SFDI parameters and triglyceride for all subjects (including both low fat and high fat groups) three hours after the meal, when both parameters are normalized to their respective baseline values.

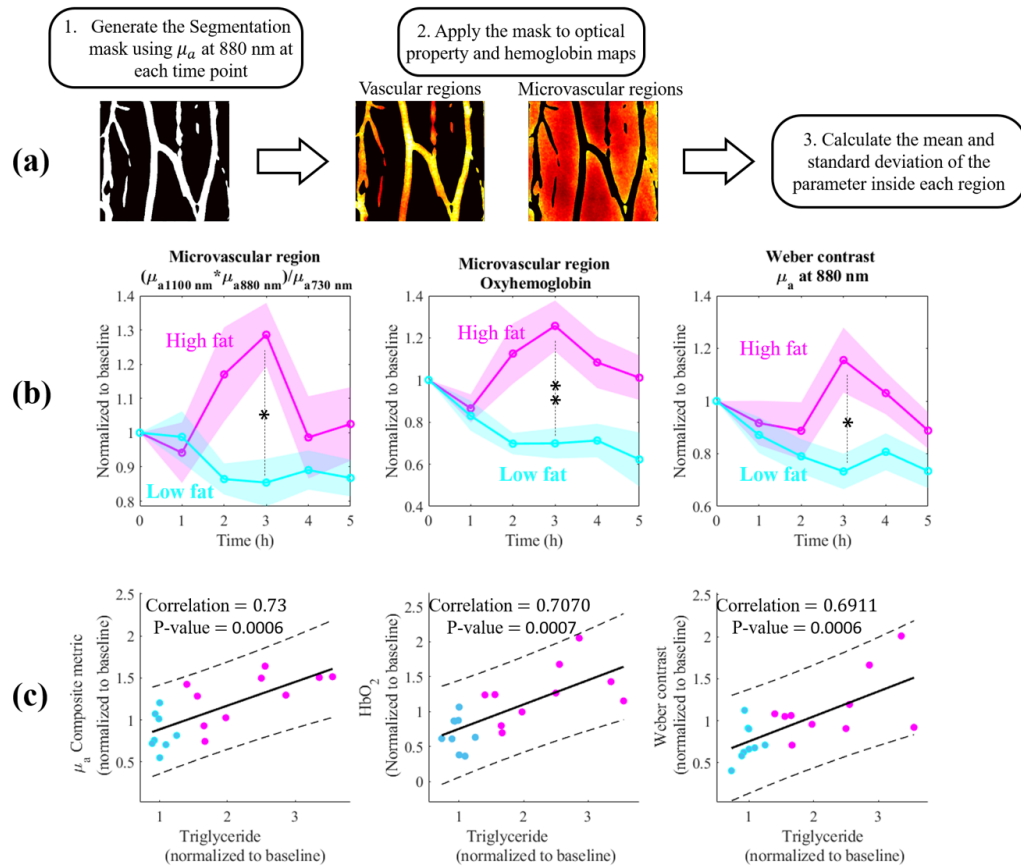


Figure 5.5: a. The process of generating the vessel mask using μ_a map at 880 nm and apply the mask to segment vascular and microvascular regions. b. Temporal changes and trends in three SFDI-derived parameters with the strongest correlation with serum triglyceride over the six measurements for high fat and low fat groups. $p < 0.05$ is shown with * and p -value < 0.01 is shown with **. c) The correlation plots for the same three metrics with triglyceride concentration combining all subjects from both group. All metrics were normalized to their respective baseline values.

Table 5.1 shows all the SFDI-derived parameters that have a strong correlation with triglyceride information from the lipid panel three hours after the meal, when comparing the relative changes of both parameters from the baseline. The strong correlations were identified based on the p -value where p -values < 0.05 was considered as significant.

Table 5.1: Pearson Correlation between measured triglyceride and SFDI parameters after normalizing to the baseline. Correlations with p-value < 0.05 are shown.

SFDI metric		Pearson correlation coefficient	P-value
μ_a Vasculature	880 nm	0.683	0.0012
	1100 nm	0.606	0.0077
μ_a Microvasculature	880 nm	0.643	0.003
	1100 nm	0.56	0.0156
Weber contrast in μ_a	730 nm	0.6095	0.0056
	880 nm	0.6911	0.0011
	1100 nm	0.6571	0.003
Composite metrics in μ_a	(1100 nm x 880 nm)/730 nm	0.7296	0.0006
	1100 nm/880 nm	-0.567	0.0142
	880 nm/730 nm	0.5450	0.0193
Hemoglobin in vasculature	HbO_2 (μ M)	0.666	0.0018
	StO_2 (%)	0.601	0.0065
Hemoglobin in microvasculature	HbO_2 (μ M)	0.707	0.0007
	StO_2 (%)	0.6442	0.0029

5.3.3 Arterial occlusion results

Arterial occlusion experiment aimed to investigate the impact of meal on hemodynamics and endothelial function by analyzing the μ_a response during reactive hyperemic phase. The temporal changes in μ_a at 800 nm over vascular and microvascular regions were analyzed separately by manually selecting ROIs on each region. Interestingly, the μ_a behaved very differently over these two regions with only the μ_a of microvascular regions exhibiting a sudden increase in μ_a characteristic of the previously observed reactive hyperemic phase following the release of the cuff [91, 92, 93]. We calculated the parameter that identified the magnitude and speed of changes in μ_a during the reactive hyperemia over the microvascular regions.

Figure 5.6.a shows an example μ_a response during the 8 minutes cuff occlusion ex-

periment, and the parameters that were identified during and after the release. **Figure 5.6.b** shows two examples of μ_a time trace at baseline and three hours after the meal, representing subjects from the high fat meal and low fat meal groups. **Figure 5.6.c** displays the mean and standard error of the calculated μ_a parameters. From these plots, it is evident that subjects who had a high fat meal exhibit a smaller $\Delta\mu_a$ from release to peak three hours after the meal, with the peak occurring at a longer time after the release (extended time to peak). Consequently, the reperfusion slope decreases three hours after the meal compared to the baseline. The area under the curve (AUC) during the initial 30 seconds after the release shows minimal changes after the high fat meal for this subject group. Conversely, subjects who consumed a low fat meal demonstrate significantly amplified reactive hyperemia three hours after the meal, characterized by a higher $\Delta\mu_a$ and a quicker response (shorter time to peak and a sharper reperfusion slope). Additionally, the AUC increases after the low fat meal in comparison to the baseline. The difference between the metrics calculated for low fat and high fat subject group is not significant at any of the time points.

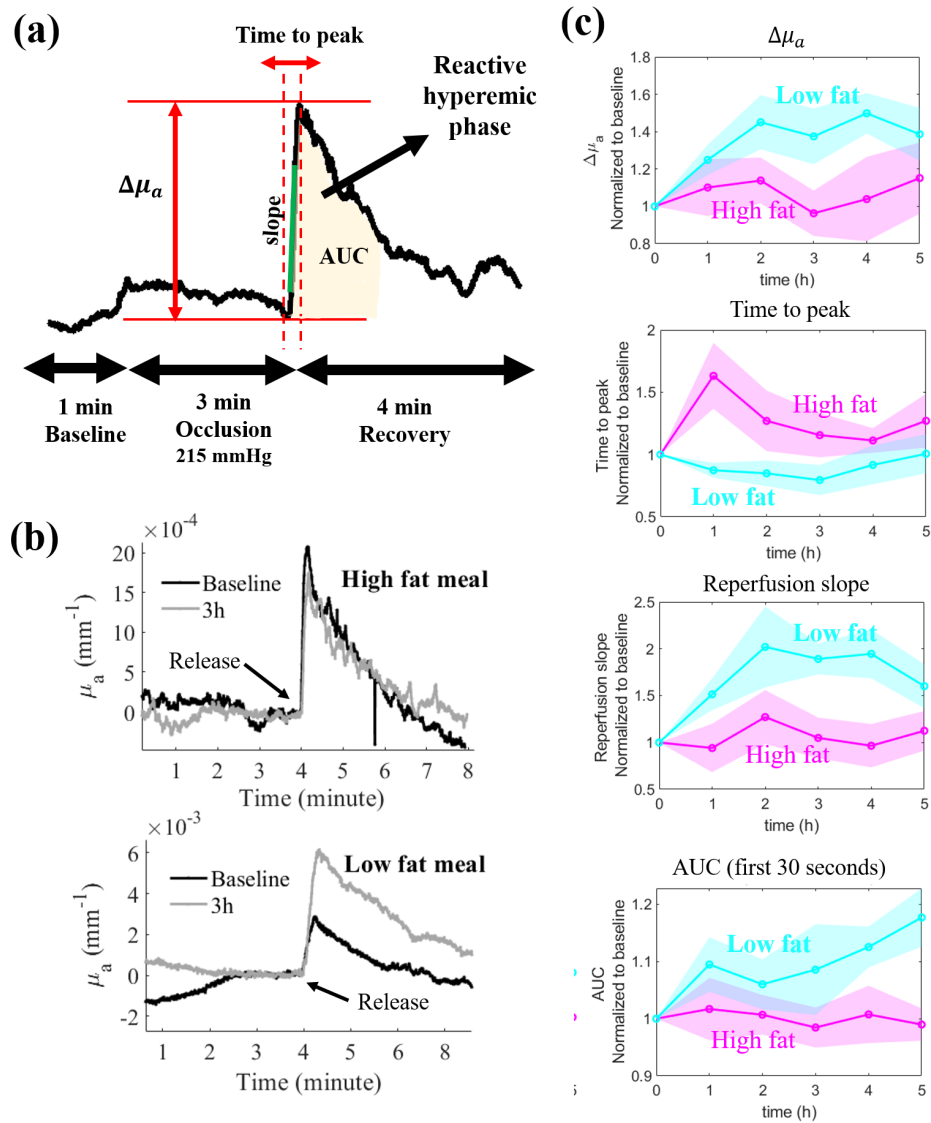


Figure 5.6: a. an example of μ_a changes during the cuff occlusion experiment and the identified parameters after the release. b. Microvascular μ_a is shown during the 8-minute cuff occlusion experiment at baseline and three hours after the meal for two representative subjects. The top panel displays the results from a subject who consumed a high fat meal, and the bottom panel shows the results from a subject who consumed a low fat meal. c. Calculated parameters during the reactive hyperemic phase for low fat and high fat meal subjects. The solid lines represent the mean values, while the shaded regions depict the standard error between all subjects.

5.4 DISCUSSION

In this work we explored the application of SFDI for monitoring meal induced changes in optical properties and hemodynamics of skeletal muscle. SFDI measurements were conducted in fasting and postprandial state from vascular and microvascular regions of the hand in a cohort of 20 subjects, with 10 subjects participating in the postprandial low fat meal study and the remaining 10 subjects participating in the postprandial high fat meal study. Lipid panel and glucose concentration were also measured at each time point from a fingerstick blood draw as the gold standard.

The results show a statistically significant distinction, especially in the μ_a related metrics, between subjects who consumed a low fat meal and those who consumed a high fat meal three hours after the meal. The composite μ_a metric ($\frac{\mu_a(1100\text{nm})\cdot\mu_a(880\text{nm})}{\mu_a(730\text{nm})}$) in microvascular regions is significantly different between the two groups three hours after the meal (p-value < 0.05) and has the strongest correlation with triglyceride when both are normalized to their respective baseline value (Pearson correlation coefficient = 0.73, p-value = 0.0006). Oxyhemoglobin of microvascular regions and Vascular-microvascular contrast of μ_a at 880 nm are the second and third metric with highest correlation with triglyceride, and both are significantly different between low fat and high fat meal subjects three hours after the meal.

The observed absorption pattern during the postprandial state can be attributed to alterations in blood flow as a result of the meal. Postprandial hyperemia refers to the increased blood flow to the digestive system following a meal [94, 95]. This may also affect the blood flow in other parts of the body. In a healthy individual, peripheral blood vessels dynamically regulate their diameter through vasoconstriction and vasodilation in order to maintain the normal blood pressure. One possible explanation for the observed alteration in the μ_a related parameters is the initial constriction of peripheral blood vessels shortly

after the meal, leading to a drop in μ_a metrics 1 hour after the meal in the high fat meal subject group. The constriction is then followed by a subsequent dilation of the vessels which resulting in an increase in μ_a metrics 2 to 5 hours after the meal [96]. Regarding the low fat meal, there may be a lower blood flow to peripheral tissue due to the reduced metabolic activity. However there is limited information available in the literature regarding such changes.

Endothelial dysfunction and the impact of meals on vasodilation are typically assessed using flow-mediated dilation (FMD), a method that examines the dilation of the brachial artery after a period of ischemia through ultrasound imaging [97, 98, 89, 99]. It is well-established that high-fat meals contribute to endothelial dysfunction by inhibiting the secretion of Nitric Oxide (NO), which is a vasodilator [89, 100, 101]. In this study, instead of utilizing FMD, our aim was to investigate the effect of meals on endothelial function by examining reactive hyperemia. Reactive hyperemia is a widely recognized method used to assess peripheral microcirculatory function and it measured the extent of limb reperfusion following a short period of ischemia [91, 92, 93]. We focused on assessing the impact of meals on reactive hyperemia within the microvascular region of the participants' hands. We observed that a high fat meal led to an impaired hyperemic response characterized by smaller and slower changes. Conversely, a low fat meal resulted in a more pronounced hyperemic response with larger and faster changes following the release of occlusion. However, we note that the differences between the high fat and low fat meals were not statistically significant at any of the recorded time points.

Despite our initial hypothesis, which was supported by ex-vivo experiments of blood and Mie simulations, we did not find any significant difference in optical scattering metrics between the high fat meal and low fat meal cohorts at any time point in our in-vivo study with healthy volunteers. In our prior work, we estimated a 2-4% change in blood

μ_s' at the three measurement wavelengths for healthy subjects after a high fat meal due to alterations in size, number density and refractive index of lipoprotein particles. However, these changes primarily occur in the blood, which constitutes only a small percentage of the overall tissue. As a result, the magnitude of scattering changes might be too small to be detected when measuring the optical properties of tissue using SFDI.

Nevertheless, although we were unable to directly detect the effect of blood lipoprotein alterations through measurement of scattering, we observed significant differences in absorption metrics when comparing postprandial measurements after low-fat and high-fat meals. The exact mechanism underlying the observed changes in μ_a after both meals cannot be definitively determined without measuring blood flow using techniques such as diffuse correlation spectroscopy (DCS) and speckle contrast optical spectroscopy (SCOS). In future studies involving postprandial measurements in healthy volunteers and individuals with cardiovascular disease, our aim is to combine these techniques with SFDI. This integration will enable a comprehensive assessment of both optical properties and hemodynamics, providing a more comprehensive understanding of the physiological processes at play.

The work presented here for the first time explores the novel application of NIR-SWIR measurements for noninvasive tracking of postprandial changes. Our findings suggest that NIR-SWIR measurements hold promise as a means to monitor physiological responses following a meal. These results have implications for diet monitoring and offer potential insight into vascular health, particularly for individuals with dyslipidemias and CVD.

5.5 CONCLUSION

In summary, our study investigated the performance of SFDI in monitoring optical properties and hemodynamics during a postprandial healthy volunteer study after low fat and high fat meal. Our findings indicate a robust correlation between several μ_a metrics and blood triglyceride levels when they both are normalized to their baseline values. Furthermore, these μ_a metrics also demonstrated a statistically significant difference three hours after the meal between the two groups. The arterial occlusion study revealed a slightly impaired reactive hyperemia phase for the high fat meal subjects, and a more pronounced response for the low fat meal subjects. These observations provide valuable insights into the noninvasive measurement of meal-induced changes in optical properties. Such measurements may serve as a potential noninvasive tool for managing dietary interventions in both healthy individuals and those with cardiovascular diseases.

CHAPTER 6

Conclusions and future directions

The concluding chapter of this thesis provides a summary of the key findings and conclusions derived from the research conducted in the preceding chapters. Additionally, it outlines potential avenues for future research in related areas.

6.1 SUMMARIES

The three chapters of this thesis have focused on advancing the instrumentation and application of Spatial Frequency Domain Imaging (SFDI) for non-invasive blood lipid monitoring.

Chapter 3 presents a compact and portable LED based NIR-SWIR SFDI system. To optimize the performance, we carefully selected wavelengths and spatial frequencies based on techniques like Cramer Rao Bound and penetration depth analysis. The new system has a μ_s' resolution of at least 0.03 mm^{-1} at 880 nm and 0.02 mm^{-1} at 1100 nm. In order to account for the layered structure of the skin, we introduced a two-layer model. This new model significantly improves our ability to detect tissue and blood beneath the 1 mm dermal skin layer. The performance of the two-layer model was validated through two-layer phantom measurements, with the two-layer model reducing the error in deeper layer μ_s' extraction by at least 24%. Finally the system and the model was used to extract optical property information of the subcutaneous tissue and blood from dorsum surface of the hand of three healthy volunteers. By employing the two-layer model, we observed an increased contrast between the vascular and microvascular regions, as well as the enhanced vessel structures that were not apparent when using the homogeneous model. This novel instrumentation and modeling approach have the potential to become a powerful tool for various clinical

applications, such as diagnosing cardiovascular diseases and diabetes.

Chapter 4 presents the impact of lipoproteins, the carriers of TG and cholesterol in the blood, on the optical properties of blood in the postprandial states. Theoretical simulations were conducted using Mie theory to estimate lipoprotein scattering properties after reviewing relevant literature to determine key simulation parameters. Experimental validation was performed using spatial frequency domain imaging (SFDI) on ex-vivo blood samples for altered concentration and size of the scattering particles, similar to chylomicron alterations after a meal. The results demonstrated that lipoproteins, especially VLDL and chylomicrons, induce significant postprandial scattering change to blood μ_s' . Our results indicates small increase in blood μ_s' (a few percent) in healthy subjects and larger increase (as high as 60%) for subjects with hypertriglyceridemia after a high fat meal.

Chapter 5 presents a healthy volunteer study for monitoring optical properties after a meal using the proposed SFDI system and model in **Chapter 3**. The effect of low fat an high fat meal were monitored for five hours after the meal by measuring the hand of 20 healthy subjects with SFDI. Additinally, the endothelial function was examined for the two groups by monitoring reactive hyperemia after an arterial occlusion using continuous DC snapshot measurements. The SFDI results were correlated with blood draw lipid panel and a strong correlation were found between triglyceride and μ_a related metrics. These findings highlights the potential for utilizing this technique in non-invasive longitudinal monitoring of blood lipids.

6.2 FUTURE DIRECTIONS

The work in this thesis provides many potential future directions, some of which are described below.

1. Expand the healthy volunteer study to cover several choice of meal (fasting, low fat-low calorie, low fat-high calorie, high fat meal). This will enable us to identify the source of the observed optical property changes with greater certainty.
2. Combine the SFDI measurements with other instrumentation that enables measurement of blood flow. One such technology that we can add to our healthy volunteer measurement protocol is speckle contrast optical spectroscopy (SCOS). SCOS utilizes a long coherence laser and a CMOS or CCD sensor to measure the interference patterns (speckle) generated from scattering of the laser light on tissue. The speckle patterns fluctuate at varying speeds depending on the rate of blood flow through the tissue, hence it allows us to monitor blood flow following a meal. Having an estimation of blood flow will help us identify the reasoning behind the μ_a related trends we observed after low fat and high fat meal, and use that information to updated and modify our SFDI instrumentation and experiments.
3. Conduct the postprandial studies on subjects with lipidemia and triglyceridemia. In **Chapter 4** we estimated the changes in postprandial blood μ_s' for healthy subjects, as well as those with type 2 diabetes and hypertriglyceridemia. While blood μ_s' only increased by <4% in healthy subjects after a meal, these changes can be much larger in subjects with lipidemia. Although we were unable to extract scattering changes

after a high-fat meal in our study with healthy volunteers, this may be attributed to the minimal nature of the changes. Therefore, conducting these experiments on subjects with hyperlipidemia may yield different results in terms of scattering trends in the postprandial state.

4. More advance inverse model for optical property extraction. The two-layer LUT inverse model has a limitation in that it considered skin as a single layer, disregarding the presence of separate epidermis, dermis, and hypodermis layers. By incorporating a more complex layered model, it is possible to enhance the accuracy of extracting optical properties from the subcutaneous tissue and blood. Confining the optical property measurements to blood may improve our ability for detecting the direct effect of lipids on blood optical properties.
5. Non-invasive blood lipid monitoring from retinal blood vessels in the absence of skin. One of the challenges in monitoring blood lipids from superficial vessels throughout the body is the influence of skin and other confounding factors, including the impact of blood volume and blood flow, on optical property measurements. Conversely, the retina provides a unique opportunity to directly observe blood vessels. Previous studies have demonstrated the impact of lipemia on retinal vessels using a fundus camera, where retinal vessels appear milky when individuals have high levels of blood lipids [102]. A potential future direction for this study is to adapt a fundus camera, modify the light source to the desired wavelength, and investigate how the scattering of retinal blood vessels changes after a meal, enabling non-invasive blood lipid monitoring.

6.3 CONCLUSION

The body of this work has aimed to improve optical imaging toward noninvasive monitoring of blood lipids. Biomedical optics holds great potentials for noninvasive assessment of tissue and blood, which makes it invaluable for several clinical and life style applications. The findings presented here offer insights and open new avenues toward future investigations of noninvasive tissue and blood monitoring.

BIBLIOGRAPHY

- [1] Anahita Pilvar, Aarohi M Mehendale, Kavon Karrobi, Fatima El-Adili, Andreea Bujor, and Darren Roblyer. Spatial frequency domain imaging for the assessment of scleroderma skin involvement. *Biomed. Opt. Express*, 14(6):2955–2968, 6 2023.
- [2] Sheng-Hao Tseng, Paulo Bargo, Anthony Durkin, and Nikiforos Kollias. Chromophore concentrations, absorption and scattering properties of human skin in-vivo. *Optics Express*, 17(17):14599–14617, 2009.
- [3] A N Bashkatov, E A Genina, V I Kochubey, and V V Tuchin. Optical properties of human skin, subcutaneous and mucous tissues in the wavelength range from 400 to 2000nm. *Journal of Physics D: Applied Physics*, 38(15):2543–2555, 2005.
- [4] P J Dykes and R Marks. Measurement of skin thickness: a comparison of two in vivo techniques with a conventional histometric method. *Journal of Investigative Dermatology*, 69(3):275–278, 1977.
- [5] Y Lee and K Hwang. Skin thickness of Korean adults. *Surgical and radiologic anatomy : SRA*, 24(3-4):183–189, 2002.
- [6] Behrooz Zabihian, Zhe Chen, Elisabet Rank, Christoph Sinz, Marco Bonesi, Harald Sattmann, Jason R Ensher, Michael P Minneman, Erich E Hoover, Jessika Weingast, Laurin Ginner, Rainer A Leitgeb, Harald Kittler, Edward Z Zhang, Paul C Beard, Wolfgang Drexler, and Mengyang Liu. Comprehensive vascular imaging using optical coherence tomography-based angiography and photoacoustic tomography. *Journal of Biomedical Optics*, 21(9):1–7, 9 2016.
- [7] World Health Organization. Cardiovascular diseases (CVDs). Technical report, 2021.
- [8] Børge G. Nordestgaard. Triglyceride-Rich Lipoproteins and Atherosclerotic Cardiovascular Disease: New Insights from Epidemiology, Genetics, and Biology. *Circulation Research*, 118(4):547–563, 2016.
- [9] Rafael Perera, Emily McFadden, Julie McLellan, Tom Lung, Philip Clarke, Teresa Pérez, Thomas Fanshawe, Andrew Dalton, Andrew Farmer, Paul Glasziou, Osamu Takahashi, John Stevens, Les Irwig, Jennifer Hirst, Sarah Stevens, Asuka Leslie, Sachiko Ohde, Gautam Deshpande, Kevin Urayama, Brian Shine, and Richard Stevens. Optimal strategies for monitoring lipid levels in patients at risk or with cardiovascular disease: a systematic review with statistical and cost-effectiveness modelling. *Health technology assessment (Winchester, England)*, 19(100):1–401, 2015.

- [10] David J Cuccia, Frédéric P Bevilacqua, Anthony Joseph Durkin, Frederick R Ayers, and Bruce Jason Tromberg. Quantitation and mapping of tissue optical properties using modulated imaging. *Journal of Biomedical Optics*, 14(2):1–13, 3 2009.
- [11] Thomas D O’Sullivan, Albert E Cerussi, Bruce J Tromberg, and David J Cuccia. Diffuse optical imaging using spatially and temporally modulated light. *Journal of Biomedical Optics*, 17(7):1–15, 7 2012.
- [12] Yanyu Zhao, Anahita Pilvar, Anup Tank, Hannah Peterson, John Jiang, Jon C Aster, John Paul Dumas, Mark C Pierce, and Darren Roblyer. Shortwave-infrared meso-patterned imaging enables label-free mapping of tissue water and lipid content. *Nature Communications*, 11(1):5355, 2020.
- [13] Rami Nachabé, Benno H W Hendriks, Marjolein van der Voort, Adrien E Desjardins, and Henricus J C M Sterenborg. Estimation of biological chromophores using diffuse optical spectroscopy: benefit of extending the UV-VIS wavelength range to include 1000 to 1600 nm. *Biomedical Optics Express*, 1(5):1432–1442, 2010.
- [14] Paul A Heidenreich, Justin G Trogon, Olga A Khavjou, Javed Butler, Kathleen Dracup, Michael D Ezekowitz, Eric Andrew Finkelstein, Yuling Hong, S Claiborne Johnston, Amit Khera, Donald M Lloyd-Jones, Sue A Nelson, Graham Nichol, Diane Orenstein, Peter W F Wilson, and Y Joseph Woo. Forecasting the future of cardiovascular disease in the United States: a policy statement from the American Heart Association. *Circulation*, 123(8):933–944, 3 2011.
- [15] Jiaquan Xu, Sherry L. Murphy, Kenneth D. Kochanek, Brigham Bastian, and Elizabeth Arias. Deaths: Final Data for 2016. *National vital statistics reports*, 67(5):1–76, 2018.
- [16] Nadeem Sarwar, John Danesh, Gudny Eiriksdottir, Gunnar Sigurdsson, Nick Wareham, Sheila Bingham, S Matthijs Boekholdt, Kay-Tee Khaw, and Vilmundur Gudnason. Triglycerides and the Risk of Coronary Heart Disease. *Circulation*, 115(4):450–458, 1 2007.
- [17] Sandeep Bansal, Julie E Buring, Nader Rifai, Samia Mora, Frank M Sacks, and Paul M Ridker. Fasting Compared With Nonfasting Triglycerides and Risk of Cardiovascular Events in Women. *The Journal of the American Medical Association*, 298(3):309–316, 7 2007.
- [18] Børge G Nordestgaard, Marianne Benn, Peter Schnohr, and Anne Tybjaerg-Hansen. Nonfasting Triglycerides and Risk of Myocardial Infarction, Ischemic Heart Disease, and Death in Men and Women. *The Journal of the American Medical Association*, 298(3):299–308, 7 2007.

- [19] Michael Miller, Neil J. Stone, Christie Ballantyne, Vera Bittner, Michael H. Criqui, Henry N. Ginsberg, Anne Carol Goldberg, William James Howard, Marc S. Jacobson, Penny M. Kris-Etherton, Terry A. Lennie, Moshe Levi, Theodore Mazzone, and Subramanian Pennathur. Triglycerides and cardiovascular disease: A scientific statement from the American Heart Association. *Circulation*, 123(20):2292–2333, 2011.
- [20] C D Gillespie, N L Keenan, J B Miner, and Y Hong. Screening for lipid disorders among adults—National Health and Nutrition Examination Survey, United States, 2005–2008. *MMWR Morb Mortal Wkly Rep*, 61 Suppl:26–31, 6 2012.
- [21] John E Hokanson and Melissa A Austin. Plasma Triglyceride Level is a Risk Factor for Cardiovascular Disease Independent of High-Density Lipoprotein Cholesterol Level: A Metaanalysis of Population-Based Prospective Studies. *Journal of Cardiovascular Risk*, 3(2):213–219, 4 1996.
- [22] S. Boquist, A. Hamsten, F. Karpe, and G. Ruotolo. Insulin and non-esterified fatty acid relations to alimentary lipaemia and plasma concentrations of postprandial triglyceride-rich lipoproteins in healthy middle-aged men. *Diabetologia*, 43(2):185–193, 2000.
- [23] Kimber L. Stanhope, Andrew A. Bremer, Valentina Medici, Katsuyuki Nakajima, Yasuki Ito, Takamitsu Nakano, Guoxia Chen, Tak Hou Fong, Vivien Lee, Roseanne I. Menorca, Nancy L. Keim, and Peter J. Havel. Consumption of fructose and high fructose corn syrup increase postprandial triglycerides, LDL-cholesterol, and apolipoprotein-B in young men and women. *Journal of Clinical Endocrinology and Metabolism*, 96(10):1596–1605, 2011.
- [24] Jose M. Ordovas. Postprandial lipemia and cardiovascular disease: A Golden opportunity. *Current Atherosclerosis Reports*, 5(6):437–444, 2003.
- [25] David J. Cuccia, Frederic Bevilacqua, Anthony J. Durkin, and Bruce J. Tromberg. Modulated imaging: quantitative analysis and tomography of turbid media in the spatial-frequency domain. *Optics Letters*, 30(11):1354, 2005.
- [26] Sylvain Gioux, Amaan Mazhar, and David J Cuccia. Spatial frequency domain imaging in 2019: principles, applications, and perspectives. *Journal of Biomedical Optics*, 24(7):1–18, 6 2019.
- [27] Robert H Wilson, Kyle P Nadeau, Frank B Jaworski, Rebecca Rowland, John Quan M Nguyen, Christian Crouzet, Rolf B Saager, Bernard Choi, Bruce J Tromberg, and Anthony J Durkin. Quantitative short-wave infrared multispectral imaging of in vivo tissue optical properties. *Journal of Biomedical Optics*, 19(8):1–4, 8 2014.

- [28] Anahita Pilvar, Jorge Plutzky, Mark C. Pierce, and Darren Roblyer. Shortwave infrared spatial frequency domain imaging for non-invasive measurement of tissue and blood optical properties. *Journal of Biomedical Optics*, 27(06):1–13, 2022.
- [29] Robert H Wilson, Kyle P Nadeau, Frank B Jaworski, Bruce J Tromberg, and Anthony J Durkin. Review of short-wave infrared spectroscopy and imaging methods for biological tissue characterization. *Journal of biomedical optics*, 20(3):30901, 3 2015.
- [30] Marc P Hansen and Douglas S Malchow. Overview of SWIR detectors, cameras, and applications. In *Proceedings of SPIE*, volume 6939, 3 2008.
- [31] Jessica A Carr, Daniel Franke, Justin R Caram, Collin F Perkinson, Mari Saif, Vasileios Askoxylakis, Meenal Datta, Dai Fukumura, Rakesh K Jain, Mounji G Bawendi, and Oliver T Bruns. Shortwave infrared fluorescence imaging with the clinically approved near-infrared dye indocyanine green. *Proceedings of the National Academy of Sciences*, 115(17):4465 LP – 4470, 4 2018.
- [32] Shoujun Zhu, Rui Tian, Alexander L Antaris, Xiaoyuan Chen, and Hongjie Dai. Near-Infrared-II Molecular Dyes for Cancer Imaging and Surgery. *Advanced Materials*, 31(24):1900321, 6 2019.
- [33] Zhenhua Hu, Cheng Fang, Bo Li, Zeyu Zhang, Caiguang Cao, Meishan Cai, Song Su, Xingwang Sun, Xiaojing Shi, Cong Li, Tiejun Zhou, Yuanxue Zhang, Chongwei Chi, Pan He, Xianming Xia, Yue Chen, Sanjiv Sam Gambhir, Zhen Cheng, and Jie Tian. First-in-human liver-tumour surgery guided by multispectral fluorescence imaging in the visible and near-infrared-I/II windows. *Nature Biomedical Engineering*, 4(3):259–271, 2020.
- [34] Aaron G Smith, Reina Perez, Aaron Thomas, Shona D Stewart, Arash Samiei, Arjun S Bangalore, Heather E Gomer, Marlena B Darr, Robert C Schweitzer, Sandhya Vasudevan, Jeffrey K Cohen, James C Post, Srinivas Murali, and Patrick J Treado. Objective determination of peripheral edema in heart failure patients using short-wave infrared molecular chemical imaging. *Journal of Biomedical Optics*, 26(10):1–17, 10 2021.
- [35] Lise L. Randeberg and Julio Hernandez-Palacios. Hyperspectral imaging of bruises in the SWIR spectral region. *Photonic Therapeutics and Diagnostics VIII*, 8207(February 2012):82070N, 2012.
- [36] Diana C Sordillo, Laura A Sordillo, Peter P Sordillo, Lingyan Shi, and Robert R Alfano. Short wavelength infrared optical windows for evaluation of benign and malignant tissues. *Journal of Biomedical Optics*, 22(4):1–7, 4 2017.

- [37] Hairong Zhang, Daniel C Salo, David M Kim, Sergey Komarov, Yuan-Chuan Tai, and Mikhail Y Berezin. Penetration depth of photons in biological tissues from hyperspectral imaging in shortwave infrared in transmission and reflection geometries. *Journal of Biomedical Optics*, 21(12):1–10, 12 2016.
- [38] Andrew M Smith, Michael C Mancini, and Shuming Nie. Second window for in vivo imaging. *Nature Nanotechnology*, 4(11):710–711, 2009.
- [39] Albert E Cerussi, Vaya W Tanamai, David Hsiang, John Butler, Rita S Mehta, and Bruce J Tromberg. Diffuse optical spectroscopic imaging correlates with final pathological response in breast cancer neoadjuvant chemotherapy. *Philosophical Transactions of the Royal Society A: Mathematical, Physical and Engineering Sciences*, 369(1955):4512–4530, 11 2011.
- [40] Bruce J Tromberg, Zheng Zhang, Anaïs Leproux, Thomas D O’Sullivan, Albert E Cerussi, Philip M Carpenter, Rita S Mehta, Darren Roblyer, Wei Yang, Keith D Paulsen, Brian W Pogue, Shudong Jiang, Peter A Kaufman, Arjun G Yodh, So Hyun Chung, Mitchell Schnall, Bradley S Snyder, Nola Hylton, David A Boas, Stefan A Carp, Steven J Isakoff, David Mankoff, and on behalf of the ACRIN 6691 investigators. Predicting Responses to Neoadjuvant Chemotherapy in Breast Cancer: ACRIN 6691 Trial of Diffuse Optical Spectroscopic Imaging. *Cancer Research*, 76(20):5933–5944, 10 2016.
- [41] Hossein S Yazdi, Thomas D O’Sullivan, Anaïs Leproux, Brian Hill, Amanda Durkin, Seraphim Telep, Jesse Lam, Siavash S Yazdi, Alice M Police, Robert M Carroll, Freddie J Combs, Tomas Strömberg, Arjun G Yodh, and Bruce J Tromberg. Mapping breast cancer blood flow index, composition, and metabolism in a human subject using combined diffuse optical spectroscopic imaging and diffuse correlation spectroscopy. *Journal of Biomedical Optics*, 22(4):45003, 4 2017.
- [42] Thomas D O’Sullivan, Anaïs Leproux, Jeon-Hor Chen, Shadfar Bahri, Alex Matlock, Darren Roblyer, Christine E McLaren, Wen-Pin Chen, Albert E Cerussi, Min-Ying Su, and Bruce J Tromberg. Optical imaging correlates with magnetic resonance imaging breast density and reveals composition changes during neoadjuvant chemotherapy. *Breast Cancer Research*, 15(1):R14, 2013.
- [43] Amaan Mazhar, Steven Dell, David J Cuccia, Sylvain Gioux, Anthony J Durkin, John V Frangioni M.D., and Bruce J Tromberg. Wavelength optimization for rapid chromophore mapping using spatial frequency domain imaging. *Journal of Biomedical Optics*, 15(6):1–9, 11 2010.
- [44] Thomas J Allen, Paul C Beard, Andrew Hall, Amar P Dhillon, and James S Owen. Spectroscopic photoacoustic imaging of lipid-rich plaques in the human aorta in the 740 to 1400 nm wavelength range. *Journal of Biomedical Optics*, 17(6):1–11, 5 2012.

- [45] R L P van Veen, H.J.C.M. Sterenborg, A Pifferi, A Torricelli, and R Cubeddu. Determination of VIS- NIR absorption coefficients of mammalian fat, with time- and spatially resolved diffuse reflectance and transmission spectroscopy. In *Biomedical Topical Meeting*, OSA Technical Digest, page SF4, Miami Beach, Florida, 2004. Optica Publishing Group.
- [46] Vivian Pera, Kavon Karrobi, Syeda Tabassum, Fei Teng, and Darren Roblyer. Optical property uncertainty estimates for spatial frequency domain imaging. *Biomedical Optics Express*, 9(2):661–678, 2018.
- [47] Thinh Phan, Rebecca Rowland, Adrien Ponticorvo, Binh C. Le, Robert H. Wilson, Seyed A. Sharif, Gordon T. Kennedy, Nicole P. Bernal, and Anthony J. Durkin. Characterizing reduced scattering coefficient of normal human skin across different anatomic locations and Fitzpatrick skin types using spatial frequency domain imaging. *Journal of Biomedical Optics*, 26(02), 2021.
- [48] Carole K Hayakawa, Kavon Karrobi, Vivian E Pera, Darren M Roblyer, and Vasanth Venugopalan. Optical sampling depth in the spatial frequency domain. *Journal of Biomedical Optics*, 24(7):1–14, 9 2018.
- [49] Matthew B Applegate, Kavon Karrobi, Joseph P Angelo Jr., Wyatt M Austin, Syeda M Tabassum, Enagnon Aguénonon, Karissa Tilbury, Rolf B Saager, Sylvain Gioux, and Darren M Roblyer. OpenSFDI: an open-source guide for constructing a spatial frequency domain imaging system. *Journal of Biomedical Optics*, 25(1):1–13, 1 2020.
- [50] Stephen T Flock, Steven L Jacques, Brian C Wilson, Willem M Star, and Martin J C van Gemert. Optical properties of intralipid: A phantom medium for light propagation studies. *Lasers in Surgery and Medicine*, 12(5):510–519, 1 1992.
- [51] D. J. Segelstein. *The complex refractive index of water (M.S. Thesis)*. University of Missouri, 1981.
- [52] Syeda Tabassum, Yanyu Zhao, Raef Istfan, Junjie Wu, David J Waxman, and Darren Roblyer. Feasibility of spatial frequency domain imaging (SFDI) for optically characterizing a preclinical oncology model. *Biomedical Optics Express*, 7(10):4154–4170, 2016.
- [53] Syeda Tabassum, Vivian Pera, Gage Greening, Timothy J Muldoon, and Darren Roblyer. Two-layer inverse model for improved longitudinal preclinical tumor imaging in the spatial frequency domain. *Journal of Biomedical Optics*, 23(7):1–12, 7 2018.

- [54] Adam R Gardner and Vasan Venugopalan. Accurate and efficient Monte Carlo solutions to the radiative transport equation in the spatial frequency domain. *Optics Letters*, 36(12):2269–2271, 2011.
- [55] Tamara L Troy and Suresh N Thennadil. Optical properties of human skin in the near infrared wavelength range of 1000 to 2200 nm. *Journal of Biomedical Optics*, 6(2):167–176, 4 2001.
- [56] Alexy N Bashkatov, Elina A. Genina, and Valery V Tuchin. Optical properties of skin, subcutaneous, and muscle tissues: a review. *Journal of Innovative Optical Health Sciences*, 04(01):9–38, 1 2011.
- [57] Steven L Jacques. Optical properties of biological tissues: a review. *Physics in Medicine and Biology*, 58(11):R37–R61, 2013.
- [58] Ben Aernouts, Eduardo Zamora-Rojas, Robbe Van Beers, Rodrigo Watté, Ling Wang, Mizuki Tsuta, Jeroen Lammertyn, and Wouter Saeys. Supercontinuum laser based optical characterization of Intralipid® phantoms in the 500-2250 nm range. *Optics express*, 21(26):32450–32467, 2013.
- [59] Tom Lister, Philip A Wright, and Paul H Chappell. Optical properties of human skin. *Journal of Biomedical Optics*, 17(9):1–15, 9 2012.
- [60] Yu Shimojo, Takahiro Nishimura, Hisanao Hazama, Toshiyuki Ozawa, and Kunio Awazu. Measurement of absorption and reduced scattering coefficients in Asian human epidermis, dermis, and subcutaneous fat tissues in the 400- to 1100-nm wavelength range for optical penetration depth and energy deposition analysis. *Journal of Biomedical Optics*, 25(4):1–14, 4 2020.
- [61] George Zonios, Aikaterini Dimou, Ioannis Bassukas, Dimitrios Galaris, Argyrios Tsolakidis, and Efthimios Kaxiras. Melanin absorption spectroscopy: new method for noninvasive skin investigation and melanoma detection. *Journal of Biomedical Optics*, 13(1):1–8, 1 2008.
- [62] Anahita Pilvar, Declan W Smith, Jorge Plutzky, and Darren M Roblyer. Feasibility of postprandial optical scattering of lipoproteins in blood as an optical marker of cardiovascular disease risk: modeling and experimental validation. *Journal of Biomedical Optics*, 28(6):65002, 2023.
- [63] Dianne Hyson, John C Rutledge, and Lars Berglund. Postprandial lipemia and cardiovascular disease. *Current atherosclerosis reports*, 5(6):437–444, 11 2003.
- [64] Riska Ariana. Hemoglobin and Hematocrit. In Hurst JW editors. Walker HK, Hall WD, editor, *Clinical Methods: The History, Physical, and Laboratory Examinations.*, chapter 151, pages 1–23. Boston, 3rd edition, 2016.

- [65] Tatsuro Yoshida, Michel Prudent, and Angelo D'Alessandro. Red blood cell storage lesion: Causes and potential clinical consequences. *Blood Transfusion*, 17(1):27–52, 2019.
- [66] John S Maier, Scott A Walker, Sergio Fantini, Maria Angela Franceschini, and Enrico Gratton. Possible correlation between blood glucose concentration and the reduced scattering coefficient of tissues in the near infrared. *Optics Letters*, 19(24):2062–2064, 1994.
- [67] Antonio M Gotto, Henry J Pownall, and Richard J B T Methods in Enzymology Havel. [1] Introduction to the plasma lipoproteins. In *Plasma Lipoproteins Part A: Preparation, Structure, and Molecular Biology*, volume 128, pages 3–41. Academic Press, 1986.
- [68] Patrick C N Rensen, Remco L A de Vruueh, Johan Kuiper, Martin K Bijsterbosch, Erik A L Biessen, and Theo J C van Berkel. Recombinant lipoproteins: lipoprotein-like lipid particles for drug targeting. *Advanced Drug Delivery Reviews*, 47(2):251–276, 2001.
- [69] G R List, W E Neff, R L Holliday, J W King, and R Holser. Hydrogenation of soybean oil triglycerides: Effect of pressure on selectivity. *Journal of the American Oil Chemists' Society*, 77(3):311–314, 2000.
- [70] Hugo J van Staveren, Christian J M Moes, Jan van Marie, Scott A Prahl, and Martin J C van Gemert. Light scattering in Intralipid-10% in the wavelength range of 400 - 1100 nm. *Applied Optics*, 30(31):4507–4514, 1991.
- [71] Darya N. Chernova, Anastasiya I. Konokhova, Olga A. Novikova, Maxim A. Yurkin, Dmitry I. Strokotov, Andrei A. Karpenko, Andrei V. Chernyshev, and Valeri P. Maltsev. Chylomicrons against light scattering: The battle for characterization. *Journal of Biophotonics*, 11(10):1–11, 2018.
- [72] Chris J Packard, Jan Boren, and Marja-Riitta Taskinen. Causes and Consequences of Hypertriglyceridemia. *Frontiers in Endocrinology*, 11, 2020.
- [73] Mary K Wojczynski, Stephen P Glasser, Albert Oberman, Edmond K Kabagambe, Paul N Hopkins, Michael Y Tsai, Robert J Straka, Jose M Ordovas, and Donna K Arnett. High-fat meal effect on LDL, HDL, and VLDL particle size and number in the Genetics of Lipid-Lowering drugs and diet network (GOLDN): an interventional study. *Lipids in Health and Disease*, 10(1):181, 2011.
- [74] Amber M. Milan, Anu Nuora, Shikha Pundir, Chantal A. Pileggi, James F. Markworth, Kaisa M. Linderborg, and David Cameron-Smith. Older adults have an altered chylomicron response to a high-fat meal. *British Journal of Nutrition*, 115(5):791–799, 2016.

- [75] Xiaoyan Ma, Jun Q Lu, R Scott Brock, Kenneth M Jacobs, Ping Yang, and Xin-Hua Hu. Determination of complex refractive index of polystyrene microspheres from 370 to 1610 nm. *Physics in Medicine & Biology*, 48(24):4165, 2003.
- [76] C.F. Bohren and D.R. Huffman. Absorption and Scattering by a Sphere. In Wiley-VCH GmbH & Co., editor, *Absorption and scattering of light by small particles*, pages 82–129. 1998.
- [77] Victor Twersky. Transparency of pair-correlated, random distributions of small scatterers, with applications to the cornea*. *Journal of the Optical Society of America*, 65(5):524–530, 1975.
- [78] Annika M. K. Nilsson, Peter Alsholm, Anders Karlsson, and Stefan Andersson-Engels. T-matrix computations of light scattering by red blood cells. *Applied Optics*, 37(13):2735, 1998.
- [79] Ben Aernouts, Robbe Van Beers, Rodrigo Watté, Jeroen Lammertyn, and Wouter Saeys. Dependent scattering in Intralipid® phantoms in the 600-1850 nm range. *Optics Express*, 22(5):6086–6098, 2014.
- [80] H J Weeth and C F Speth. Estimation of Bovine Plasma Protein from Refractive Index. *Journal of Animal Science*, 27(1):146–149, 1 1968.
- [81] Farideh Shishehbor, Helen M Roche, and Michael J Gibney. The effect of low and moderate fat intakes on the postprandial lipaemic and hormonal responses in healthy volunteers. *British Journal of Nutrition*, 81(1):2530, 1999.
- [82] Becker D. Clark L. T. Cooper R. S. Denke M. A. Howard J. Hunninghake D. B. Illingworth D. R. Luepker R. V. McBride P. McKenney J. M. Pasternak R. C. Stone N. J. Van Horn L. Grundy, S. M. Detection, evaluation, and treatment of high blood cholesterol in adults (Adult Treatment Panel III). Technical report, 2002.
- [83] Børge G Nordestgaard, Anne Langsted, Samia Mora, Genovefa Kolovou, Hannsjörg Baum, Eric Bruckert, Gerald F Watts, Grazyna Sypniewska, Olov Wiklund, Jan Borén, M John Chapman, Christa Cobbaert, Olivier S Descamps, Arnold von Eckardstein, Pia R Kamstrup, Kari Pulkki, Florian Kronenberg, Alan T Remaley, Nader Rifai, Emilio Ros, and Michel Langlois. Fasting is not routinely required for determination of a lipid profile: clinical and laboratory implications including flagging at desirable concentration cut-points—a joint consensus statement from the European Atherosclerosis Society and European Feder. *European heart journal*, 37(25):1944–1958, 7 2016.
- [84] Nienke Bosschaart, Gerda J Edelman, Maurice C G Aalders, Ton G van Leeuwen, and Dirk J Faber. A literature review and novel theoretical approach on the optical properties of whole blood. *Lasers in Medical Science*, 29(2):453–479, 2014.

- [85] André Roggan, Moritz Friebel, K Do Rschel, Andreas Hahn, and Gu Nter Mu Ller. Optical Properties of Circulating Human Blood in the Wavelength Range 400-2500 nm. *Journal of biomedical optics*, 4 1:36–46, 1999.
- [86] Laxmi S. Mehta, Theresa M. Beckie, Holli A. DeVon, Cindy L. Grines, Harlan M. Krumholz, Michelle N. Johnson, Kathryn J. Lindley, Viola Vaccarino, Tracy Y. Wang, Karol E. Watson, and Nanette K. Wenger. Acute Myocardial Infarction in Women : A Scientific Statement from the American Heart Association. *Circulation*, 133(9):916–947, 2016.
- [87] Susan A Abookire, Andrew S Karson, Julie Fiskio, and David W Bates. Use and Monitoring of "Statin" Lipid-Lowering Drugs Compared With Guidelines. *Archives of Internal Medicine*, 161(1):53–58, 1 2001.
- [88] Xin Wang, Brian W Pogue, Shudong Jiang, Xiaomei Song, Keith D Paulsen, Christine Kogel, Steven P Poplack, and Wendy A Wells. Approximation of Mie scattering parameters in near-infrared tomography of normal breast tissue in vivo. *Journal of Biomedical Optics*, 10(5):51704, 9 2005.
- [89] Robert A Vogel, Mary C Corretti, and Gary D Plotnick. Effect of a Single High-Fat Meal on Endothelial Function in Healthy Subjects. *The American Journal of Cardiology*, 79(3):350–354, 1997.
- [90] Juanita J Fewkes, Nicole J Kellow, Stephanie F Cowan, Gary Williamson, and Aimee L Dordevic. A single, high-fat meal adversely affects postprandial endothelial function: a systematic review and meta-analysis. *The American Journal of Clinical Nutrition*, 116(3):699–729, 9 2022.
- [91] Ryan Rosenberry and Michael D Nelson. Reactive hyperemia: a review of methods, mechanisms, and considerations. *American Journal of Physiology-Regulatory, Integrative and Comparative Physiology*, 318(3):R605–R618, 2 2020.
- [92] Jay D Coffman and Donald E Gregg. Reactive hyperemia characteristics of the myocardium. *American Journal of Physiology-Legacy Content*, 199(6):1143–1149, 12 1960.
- [93] Alberto Coccarelli and Michael D. Nelson. Modeling Reactive Hyperemia to Better Understand and Assess Microvascular Function: A Review of Techniques. *Annals of Biomedical Engineering*, 51(3):479–492, 2023.
- [94] Adam David Jeays, Patricia Veronica Lawford, Richard Gillott, Paul A Spencer, Karna Dev Bardhan, and David Rodney Hose. A framework for the modeling of gut blood flow regulation and postprandial hyperaemia. *World journal of gastroenterology*, 13(9):1393–1398, 3 2007.

- [95] R H Gallavan and C C Chou. Possible mechanisms for the initiation and maintenance of postprandial intestinal hyperemia. *American Journal of Physiology-Gastrointestinal and Liver Physiology*, 249(3):G301–G308, 9 1985.
- [96] Gary D Plotnick, Mary C Corretti, and Robert A Vogel. Effect of Antioxidant Vitamins on the Transient Impairment of Endothelium-Dependent Brachial Artery Vasoactivity Following a Single High-Fat Meal. *The Journal of the American Medical Association*, 278(20):1682–1686, 11 1997.
- [97] Rouyanne T Ras, Martinette T Streppel, Richard Draijer, and Peter L Zock. Flow-mediated dilation and cardiovascular risk prediction: A systematic review with meta-analysis. *International Journal of Cardiology*, 168(1):344–351, 2013.
- [98] Hasan Korkmaz and Orhan Onalan. Evaluation of Endothelial Dysfunction: Flow-Mediated Dilation. *Endothelium*, 15(4):157–163, 1 2008.
- [99] C. Giannattasio, A. Zoppo, G. Gentile, M. Failla, A. Capra, F. M. Maggi, A. Catapano, and G. Mancina. Acute effect of high-fat meal on endothelial function in moderately dyslipidemic subjects. *Arteriosclerosis, Thrombosis, and Vascular Biology*, 25(2):406–410, 2005.
- [100] Anthony M. Dart and Jaye P.F. Chin-Dusting. Lipids and the endothelium. *Cardiovascular Research*, 43(2):308–322, 1999.
- [101] Hideki Shige, Toshitsugu Ishikawa, Michio Suzukawa, Toshimitsu Ito, Kei Nakajima, Kenji Higashi, Makoto Ayaori, Shinji Tabata, Fumitaka Ohsuzu, and Haruo Nakamura. Endothelium-dependent flow-mediated vasodilation in the postprandial state in type 2 diabetes mellitus. *American Journal of Cardiology*, 84(10):1272–1274, 1999.
- [102] Sheng Juan Zhang, Zhong Yang Yan, Li Fei Yuan, Yan Hui Wang, and Li Fei Wang. Multimodal imaging study of lipemia retinalis with diabetic retinopathy: A case report. *World Journal of Clinical Cases*, 10(19):6736–6743, 2022.

CURRICULUM VITAE

Anahita Pilvar

EMAIL: apilvar@bu.edu

EDUCATION:

- 2017-2023 **Boston University**, Boston, MA
Ph.D. in Electrical Engineering
Advisor: Dr. Darren Roblyer
Total Cumulative GPA: 3.84/4
- 2017-2021 **Boston University**, Boston, MA
M.S.in Electrical Engineering
Advisor: Dr. Darren Roblyer
Total Cumulative GPA: 3.84/4
- 2012- 2017 **Sharif University of Technology**, Tehran, Iran
B.S.in Electrical Engineering, majoring in Electronics
Total Cumulative GPA: 17/20

PEER REVIEWED PUBLICATIONS:

- 2023 "Spatial frequency domain imaging for assessment of scleroderma skin involvement"
A Pilvar, A Mehendale, K Karrobi, F El-Adili, A Bujor, D Roblyer, Biomedical Optics Express, 2023
- 2023 "Feasibility of postprandial optical scattering of lipoproteins in blood as an optical marker of cardiovascular disease risk: modeling and experimental validation"
A Pilvar, D W.Smoth, J Plutzky, D Roblyer, Journal of Biomedical Optics, 2023

- 2023 "A shortwave infrared diffuse optical wearable probe for quantification of water and lipid content in emulsion phantoms using deep learning"
S S. Spink, **A Pilvar**, L Lin Wei, J Frias, K Anders, S Franco, O C Rose, M Freeman, G Bag, H Huang, D Roblyer, *Journal of Biomedical Optics*, 2023
- 2022 "Shortwave infrared spatial frequency domain imaging for non-invasive measurement of tissue and blood optical properties"
A Pilvar, J Plutzky, M C. Pierce, D Roblyer, *Journal of Biomedical Optics*, 2022
- 2020 "Shortwave-infrared meso-patterned imaging enables label-free mapping of tissue water and lipid content"
Y Zhao, **A Pilvar**, A Tank, H Peterson, J Jiang, J C. Aster, J P Dumas, M C. Pierce, D Roblyer, *Nature Communication*, 2020
- 2019 "compressive Remodeling Alters fluid transport properties of collagen networksimplications for tumor Growth"
J Ferruzzi, M Sun, A Gkousioudi, **A Pilvar**, D Roblyer, Y Zhang, MH Zaman, *Scientific reports*, 2019

BOOK CHAPTER:

- 2022 Y. Zhao, **A. Pilvar**, M. C. Pierce, and D. Roblyer, Short-Wave Infrared Meso-Patterned Imaging for Quantitative and Label-Free Tissue Characterization, in *Short-Wavelength Infrared Windows for Biomedical Applications*, L. A. Sordillo and P. P. Sordillo, Eds., SPIE Press, Bellingham, Washington, pp. 141159 (2022).

POSTER AND PRESENTATION:

- 2023 SPIE Photonics West Conference, San Francisco, CA (Invited Talk)
"Scattering and hemodynamic changes after a high-fat meal measured with shortwave infrared spatial frequency domain imaging (SWIR SFDI)"
- 2022 Gordon research conference (GRC) on optics and photonics in medicine and biology, Lewiston, Maine (Poster)
"Non-invasive blood lipid monitoring with shortwave infrared spatial frequency domain imaging (SWIR SFDI)"

- 2022 Biophotonics Congress: Biomedical Optics Congress, Fort Lauderdale, FL (Talk)
"Non-invasive Blood Lipid Monitoring Using Shortwave Infrared Spatial Frequency Domain Imaging (SWIR SFDI)"
- 2022 SPIE Photonics West Conference, San Francisco, CA (Talk)
Clinic ready shortwave infrared spatial frequency domain imaging (SWIR SFDI) system for non-invasive monitoring of postprandial blood lipids
- 2022 SPIE Photonics West Conference, San Francisco, CA (Talk)
Spatial frequency domain imaging (SFDI) to quantify skin fibrosis in patients with scleroderma
- 2021 SPIE Photonics West Conference, Virtual, (Talk)
Shortwave Infrared (SWIR) Spatial Frequency Domain Imaging (SFDI) for monitoring blood lipids
- 2020 SPIE Photonics West Conference, San Francisco, CA (Talk)
Hyperspectral Shortwave Infrared Spatial Frequency Domain Imaging for the extraction of water and lipids concentrations in tissue and blood
- 2019 Northeast Symposium on Biomedical Optics (NESBO), Boston, MA (Poster)
Shortwave Infrared Spatial Frequency Domain Imaging for extracting water and lipid concentrations from biological samples

EXPERIENCES AND PROFESSIONAL SERVICES:

Teacher Assistance

- 2019 Teacher assistant of Electric circuit, Boston University
- 2018 Teacher assistant of Electric circuit, Boston University
- 2016 Teacher Assistant of Pulse Technique and Digital Circuits, Sharif University
- 2016 Teacher Assistant of Logic circuits, Sharif University
- 2015 Laboratory Teaching Assistant of EE Principle & Lab, Sharif University
- 2015 Teacher Assistant of Analog Circuits, Sharif University

Mentorship

2019-2022 Mentored three undergraduate groups in the Boston University Biomedical Engineering department for their senior design project for developing a SWIR wearable probe.

Memberships

2018 - 2022 Officer of OSA/SPIE Student Chapter at Boston University
 2018 - Current Member of Optical Society of America (OSA)
 2018 - Current Member of International Society of Optics and Photonics (SPIE)

Workshops Attendance

2022 Completed the NIH ec3i entrepreneurship program
 2022 Completed the i-CORPS entrepreneurship program
 2019 Attendance in OSA Student Leadership Conference, Washington, DC
 2019 New England FLIM Workshop, Boston University
 2018 Attendance in "Short Course in Computational Biophotonics" at Beckman Laser Institute, University of California, Irvine, CA

Peer-review articles for

- Journal of biomedical optics (JBO)
- Biomedical Optics Express (BOE)
- Applied science

HONORS AND AWARDS:

2019 Received recognition as the Best Teaching Assistant of the semester in the Electrical and Computer Engineering (ECE) department at Boston University
 2012 Ranked 24th in the National University Entrance Exam in mathematics and physics among more than 40000 participants in the country
 2012-2017 Awarded the National Elites Foundation scholarship in Iran

SKILLS:

Software Skills

Simulation/Design Software: MATLAB and Simulink, Labview, ImageJ

Computer Languages: Python, C/C++

Tools: Solidworks, L^AT_EX, Excel, Word, PowerPoint

Hardware Skills

Designing and Debugging Optical Systems

Microscopy (2-photon microscopy, Fluorescence Lifetime Imaging Microscopy

(FLIM), Confocal Microscopy)

Human and animal study experiences

Field of Study/Lab Skills

Diffuse Optical Imaging (DOI)

Spatial Frequency Domain Imaging (SFDI)

Wearable devices

Digital signal processing

Machine learning

ProQuest Number: 30567018

INFORMATION TO ALL USERS

The quality and completeness of this reproduction is dependent on the quality and completeness of the copy made available to ProQuest.



Distributed by ProQuest LLC (2023).

Copyright of the Dissertation is held by the Author unless otherwise noted.

This work may be used in accordance with the terms of the Creative Commons license or other rights statement, as indicated in the copyright statement or in the metadata associated with this work. Unless otherwise specified in the copyright statement or the metadata, all rights are reserved by the copyright holder.

This work is protected against unauthorized copying under Title 17, United States Code and other applicable copyright laws.

Microform Edition where available © ProQuest LLC. No reproduction or digitization of the Microform Edition is authorized without permission of ProQuest LLC.

ProQuest LLC
789 East Eisenhower Parkway
P.O. Box 1346
Ann Arbor, MI 48106 - 1346 USA